MODELING ULTRATHIN 2D TRANSITION METAL DI-CHALCOGENIDES (TMDCS) BASED ON TUNGSTEN FOR PHOTOVOLTAIC APPLICATIONS

by

Sayan Roy

A Dissertation

Submitted to the Faculty of Purdue University

In Partial Fulfillment of the Requirements for the degree of

Doctor of Philosophy

School of Electrical and Computer Engineering

West Lafayette, Indiana

May 2021

THE PURDUE UNIVERSITY GRADUATE SCHOOL
STATEMENT OF COMMITTEE APPROVAL

Dr. Peter Bermel, Chair

School of Electrical and Computer Engineering

Dr. Daniel Elliott

School of Electrical and Computer Engineering

Dr. Mark Lundstrom

School of Electrical and Computer Engineering

Dr. Jeffrey Greeley

School of Chemical Engineering

Approved by:

Dr. Dimitrios Peroulis

This dissertation is dedicated to my childhood favorite soccer team,

Mohun Bagan A.C.

ACKNOWLEDGMENTS

I have been very fortunate to work with my doctoral advisor, Prof. Peter Bermel, and I am very grateful for his mentorship and unconditional support during my time as a graduate student in Purdue University. I would like to thank Prof. Daniel Elliott, Prof. Mark Lundstrom and Prof. Jeffrey Greeley for serving on my doctoral advisory committee, and providing supportive and constructive feedback in my research projects over the past years. I would also like to thank my collaborators Prof. Sabre Kais and Dr. Zixuan Hu from the Department of Chemistry at Purdue University for working with me and guiding me in one of my most challenging research projects. Their invaluable technical guidance and support have helped me to take major strides in my research progress.

I am very grateful to my research group members for all the technical collaborations, together with thought-provoking and inspiring discussions. Also, I am very thankful to Prof. Muhammad Ashraful Alam, Prof. Rakesh Agrawal, Prof. Jeffery Gray and all students in the Network for Photovoltaic Technology research group for the supportive feedback and helpful advice during our weekly meetings.

Most importantly, I want to thank my family members for their strong and unwavering support during my academic journey. Their unconditional support for my goals and ambitions, the continuous encouragement at every point of in my life, and their firm belief in my endeavors have been instrumental in shaping my personality and helping me succeed both at the personal and professional levels. Finally, I want to extend my sincere gratitude to my childhood friends and my friends in Purdue for the unforgettable and priceless memories during my student life.

TABLE OF CONTENTS

LIST OF TABLES

LIST OF FIGURES

LIST OF ABBREVIATIONS

TMDC – Transition Metal Di-Chalcogenide

DFT – Density Functional Theory

HIT – Heterojunction with Intrinsic Thin Layer

WS_2 – Tungsten Disulfide

WSe_2 – Tungsten Diselenide

MoS_2 – Molybdenum Disulfide

V_{OC} – Open-circuit Voltage

J_{SC} – Short-circuit Current

ABSTRACT

Atomically thin 2D layered semiconductor materials such as Transition Metal Di-Chalcogenides (TMDCs) have great potential for use as flexible, ultra-thin photovoltaic materials in solar cells due to their favorable photon absorption and electronic transport properties. In this dissertation, the electronic properties, such as band structure and bandgap, and optical absorption properties of a TMDC known as Tungsten Disulfide (WS_2) were obtained from Density Functional Theory (DFT) calculations to design conventional and unconventional solar cells. Using these properties, a 1 μm thick heterojunction solar cell based on monolayer and bulk WS_2 together with amorphous silicon (a-Si) was modeled using numerical calculations and simulations. The maximum efficiency of this cell is 23.3% with $V_{OC} = 0.84$ V and $J_{SC} = 33.5$ mA/cm^2 under the AM1.5G terrestrial solar spectrum. Next, a similar but even thinner solar cell with a thickness of 200 nm, together with a light trapping structure and an anti-reflection coating layer, was modeled under the AM0 space solar spectrum; similar device performance efficiencies around 21-23% were obtained. The performance of these solar cell models is comparable to many commercial cells in both terrestrial and space photovoltaics. As conventional photovoltaics approach the Shockley-Queisser limit, the need for unconventional materials and approaches has become more apparent. Hybrid alloys of TMDCs exhibit tunable direct bandgaps and significant dipole moments. Dark state protection induced by dipole-dipole interactions forms new bright and dark states in the conduction band that reduce radiative recombination and enhance photon-to-electron conversion, leading to significantly higher photocurrents. In our work, current enhancement of up to 35% has been demonstrated by modeling dark state protection in a solar cell composed of Tungsten Diselenide (WSe_2) and Tungsten Sulfo-Selenide (WSeS), with the potential to exceed the Shockley-Queisser limit under ideal conditions.

1. INTRODUCTION

Photovoltaics is the process of converting the energy from sunlight directly into electricity using solar cells. It is a convenient method of harnessing the sun's energy. Solar cells convert the solar radiation into electricity with minimum consumption of resources and pollution, making them robust, reliable, and resilient. Photovoltaics is a growing and important alternative to conventional sources of energy such as fossil fuel electricity generation. It is also an indispensable source of power for space missions. Solar cells not only provide cheap and convenient power supply, but they also significantly diminish the impact of environmental damage caused by conventional electricity generation. They are one of the most environment-friendly electricity generating source. The environmental impact of electricity generation, particularly the greenhouse effect, adds further importance to the large-scale implementation of photovoltaics. Progress in photovoltaic research would not have been possible without major advances in semiconductor materials and manufacturing techniques.

1.1 Fundamentals of Photovoltaic Materials

When a semiconductor material is exposed to light, it absorbs the photons, exciting charge carriers (electrons and holes), which and separated to create electrical current. This current is extracted through conductive metal contacts and can then be used to power any external device or power grid. The efficiency of a solar cell is the amount of electrical power coming out compared to the incident energy, which is indicative of how effective the cell is at converting solar energy to electricity. Efficiency heavily depends on the properties and features of the constituent materials, as well as their geometries. An important property of semiconductors is the bandgap, which indicates what wavelengths of light the material can absorb and convert to electricity. If the semiconductor's bandgap matches the wavelengths of incident light, then that solar cell can efficiently convert most of the available energy. However, a semiconductor can only convert photons with the energy of the bandgap with high efficiency. Photons with lower energy are not absorbed and those with higher energy are reduced to the bandgap energy by thermalization losses.

A lot of research studies and investigations are ongoing into the search for new photovoltaic materials. Some requirements for an ideal solar cell material are:

- Bandgap between 1-2 eV.
- Thin film transparent and conducting structure.
- High Diffusion Length for electrons and holes.
- Tunability of electrical and optical properties.
- Consisting of readily available, non-toxic materials.
- Easily manufacturable and suitable for large area production.
- Good photovoltaic conversion efficiency.
- Long-term stability and reliability.

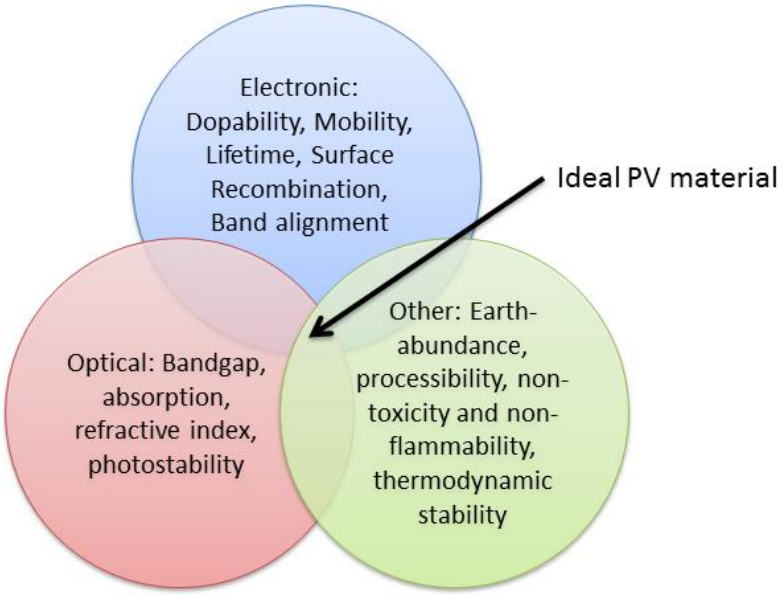

Figure 1. Many factors are needed for a favorable photovoltaic material (P. Bermel, personal communication, January 20, 2014).

1.2 2D Materials for Photovoltaics

Two-dimensional (2D) materials have gathered an increasing amount of interest from their unique potential benefits for a wide variety of optoelectronic devices [1]–[10]. Transition metal di-chalcogenides (TMDCs) are among the most attractive 2D layered materials that can be fabricated with atomic-scale thickness and a significant bandgap, as a replacement for bulk semiconductors for photovoltaic (PV) applications [2], [5], [8]. Ultra-thin multi-junction structures can be easily stacked due to van der Waals interactions [2], [3]. The 2D monolayers of TMDCs have direct

bandgaps while the bulk structures have indirect bandgap [2], [7]. They have promising electronic and optical properties suitable for applications in photovoltaics [1]. They have a thin film structure, which is both absorptive and conducting.

It has been reported that 2D TMDC materials can absorb up to 5-10% of incident sunlight in less than 1 nm thickness and can achieve significantly higher sunlight absorption per unit volume than commonly used solar absorbers such as GaAs and Si [11]. This could potentially make for much more lightweight and flexible photovoltaic modules. Tungsten disulfide (WS_2), a Transition Metal Di-Chalcogenide (TMDC), is an important 2D layered material which has attracted a great deal of interest because of its significant chemical and physical properties. It has a band gap of 1.3-2.2 eV, well within the range of photovoltaic materials, which makes it attractive for these applications.

Its 2D layered structure makes it possible to modify and tune its electronic properties by doping with other atoms or molecules between weakly bonded layers. It is also possible to apply external force or stimuli to modify its structure, and hence, its electronic properties. Like other TMDCs, WS_2 has significant absorption of incident photons with energies above its bandgap, make it a good absorber of solar radiation. It also exhibits excellent carrier transport properties, as demonstrated by high typical mobility values and high minority carrier diffusion lengths. Recent advances have demonstrated large scale fabrication and manufacture of TMDC-based devices. TMDCs are, in general, very stable, and resistant to atmospheric conditions and extremities. A major reason for using tungsten disulfide (WS_2) over molybdenum disulfide (MoS_2) is that the latter can get easily oxidized in the ambient air [12]; this can lead to significant degradation of devices operating in the natural environment.

Ultra-thin TMDCs have very favorable properties for a variety of nanoelectronic applications. The intrinsic bandgap of most TMDCs, together with high mobility values, and the ability to fabricate devices based on one to few layers of TMDCs has allowed for the design and development of ultra-thin transistors based on single-layer TMDCs (Figure 2). Ultra-thin TMDCs are also suitable for applications in various optoelectronic devices where the direct bandgap allows high absorption coefficients and efficient electron–hole pair generation under photoexcitation. Highly sensitive photodetectors can be fabricated using single-layer TMDCs due to favorable

optical absorption properties (Figure 3). Monolayer TMDCs have great potential for optoelectronic devices, light sensing and biomedical imaging.

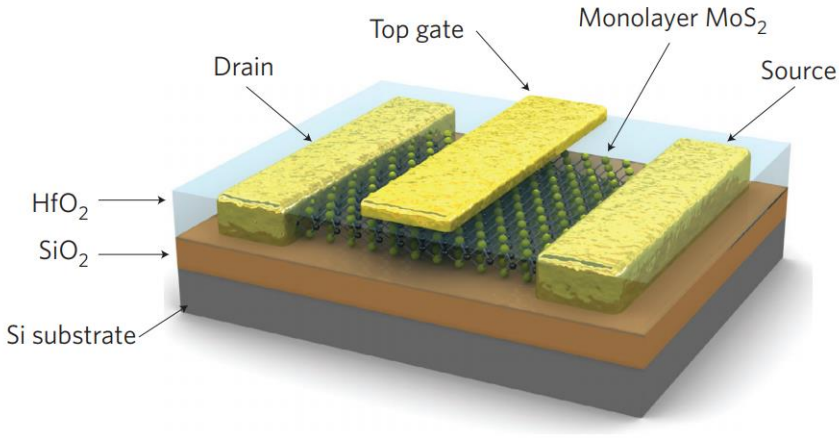

Figure 2. Single-layer MoS_2 transistor [8].

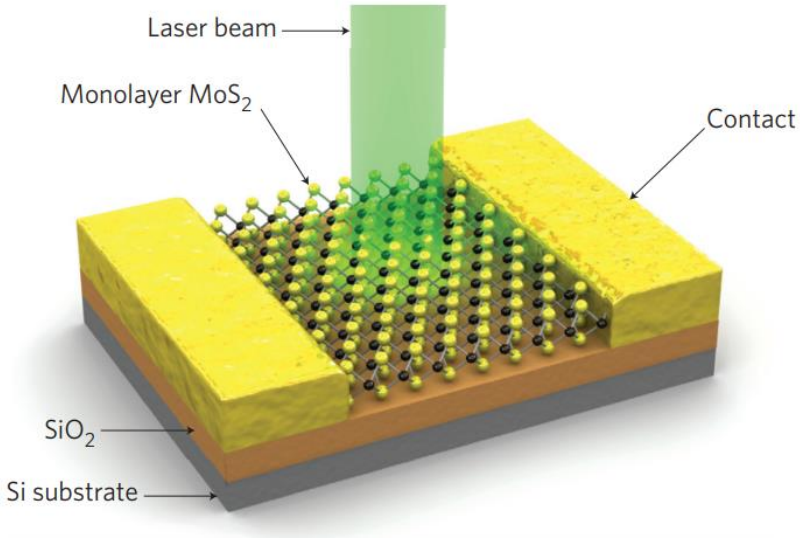

Figure 3. Single-layer MoS_2 photodetector [13].

As a result of the potentially favorable electronic and optical properties of ultra-thin TMDC semiconductors, they are strong candidates for implementation as the active materials in photovoltaic applications. TMDC-based photovoltaic systems with 1 nm thick active layers can attain power conversion efficiencies of up to ~1%, corresponding to more than an order of

magnitude higher power densities than the best existing ultrathin solar cells (Figure 4). Two-dimensional TMDCs have huge potential for implementation solar radiation absorption and energy conversion at the nanoscale level.

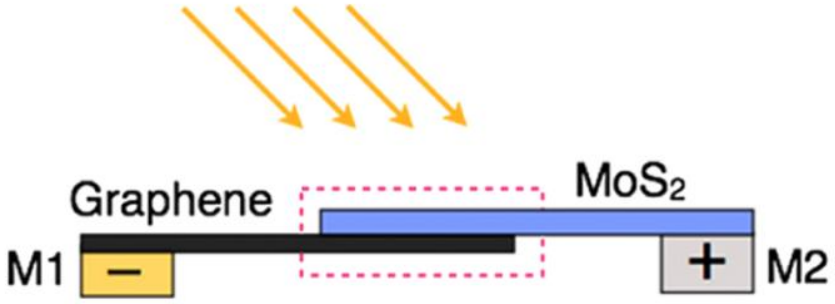

Figure 4. Nanoscale photovoltaics with single-layer TMDCs [11].

We have investigated the fundamental electronic properties of WS_2 in order to study and explore device level applications, and understand the benefits and limitations of integration in new and existing technology. We have calculated the electronic band structure, which gives us important properties such as bandgap, electronic transitions, density of states and photon absorption. The electronic band structure gives us the foundation to explore and obtain additional properties of the material, such as effective density of states for carriers and absorption coefficient for incident photons. These properties give us an insight and knowledge of potential applications of these materials, which enables us to progress towards investigating device-level implementations of WS_2 in various applications.

Using the electronic and optical properties of WS_2, we have developed p-n junction solar cell models using different structures of WS_2, bulk WS_2 and a-Si to obtain a photovoltaic device with high efficiencies, comparable to existing technology. The device simulations of our models were carried out under the terrestrial solar radiation on the surface of the Earth. In addition, we have also explored potential applications of WS_2-based solar cell model in space photovoltaics where this material can outperform existing technology.

1.3 Space Photovoltaics

Space photovoltaics has played a major role in providing electric power for most space missions. Solar radiation in space, one of the few local energy sources, can be converted directly to electricity. Advances in space photovoltaic technology has opened up a vast array of opportunities for space satellite and exploratory missions with longer and more reliable power supply requirements. The space solar radiation, called air-mass zero or AM0, is the solar radiation unaffected by the Earth's atmosphere. It is around 30-40% more intense than the terrestrial solar radiation. There are some key requirements for space photovoltaic systems. High conversion efficiency, together with light weight, is desired because of limited area and weight restrictions. An important and necessary feature is resistance to radiation-induced degradation in space environment; the presence of large concentrations of high energy particles and cosmic rays can significantly damage solar cells. Long-term operational reliability is vital for implementation in long-range space missions [14].

Until recently, silicon-based solar cells were most commonly used in space photovoltaics; there has been steady advances in the internal designs to be fine-tuned for best performance in space environment. The performance of space solar cells has been greatly enhanced by incorporation of complex light trapping structures, advanced anti-reflection coatings and improved radiation tolerance. Photovoltaic modules based on silicon initially gave efficiencies around 14-15%. In the recent past, high efficiency solar cells based on GaAs has been developed which can exhibit efficiencies around 18-19%. There is a big demand for the development of space photovoltaic systems with even higher efficiencies above 20% [15].

In addition to enhanced power output and high efficiencies, recent research has focused on developing space solar cells with ultra-thin active materials and high radiation resistance. Thin fil solar cells have the advantage of low cost and light weight, but their design and progress has been negatively affected by low efficiencies arising from reduced absorption of the broad-spectrum space solar radiation. There is constant search for new materials which can generate high power outputs in ultra-thin structures.

TMDCs are the perfect candidate for future implementation in space photovoltaic technology. They can absorb a significant amount of solar radiation in ultra-thin material structures. They have good absorptivity for high-energy photons. And they have the flexibility of integration

and incorporation with existing photovoltaic technology. Two-dimensional TMDCs are characterized by their ultra-thin structures, low weight and high power density, together with high resilience and reliability. TMDCs have a high degree of resistance to radiation-induced damage; nanoelectronic devices based on TMDCs have been demonstrated to exhibit negligible degradation in performance on exposure to high energy radiation in space environment. This makes them advantageous and beneficial for applications in high radiation environments. They have strong potential for implementation in space-based electronic and optical devices, and are very good candidates for space photovoltaic applications [16].

In ultra-thin solar cells, the major factor behind the low efficiencies is the reduced absorption of incident solar radiation in the thin materials. The incident light rays enter the cell through the front surface and, if not absorbed, leave through the rear surface of the cell, or are reflected back into the material if there is a planar reflector surface. The optical path length of the solar radiation is much lower than thicker solar cells. There has been extensive research on the development of sophisticated arrangements and complex structures that can extend the effective path length of light inside the cell; this phenomenon is called light trapping, as it allows for enhanced absorption of the incident solar radiation in an ultra-thin solar cell.

In photovoltaic systems, light trapping arrangement is used for enhancing the optical absorption in a solar cell and, at the same time, decreasing the active layer thicknesses, which results in light-weight, low-dimensionality and high efficiency devices [17]. Thinner devices allow for improved collection of generated carriers, with less constraints on the minority carrier diffusion lengths. With an appropriate light trapping structure, a thinner solar cell can retain the absorption of the thicker device and also have a higher open-circuit voltage [18], [19]. An optimum solar cell with light trapping is one in which the optical path length is several times the actual device thickness, where the optical path length of a device is the distance that an unabsorbed photon travels within the device before escaping out.

In almost all semiconductor materials, a significant portion of the incident radiation is lost by surface reflection. Silicon, for example, has a high surface reflection of over 30% [20]. This is a big loss of the incident radiation in solar cells; even solar cells with highly absorptive materials can have reduced power outputs because of this loss of photons from surface reflection. This loss

of incident radiation can be reduced by a great extent by incorporating a suitable dielectric material layer to function as an anti-reflection coating which minimizes surface reflection for a range of wavelengths in the incident solar spectrum.

An antireflective or anti-reflection coating is a type of optical coating applied to the top surface of solar cells to reduce reflection. In solar cells with highly absorptive materials, this improves the efficiency of the device since less light is lost due to surface reflection. An anti-reflection coating consists of a thin layer of an appropriate dielectric material, with a specifically chosen refractive index and thickness, such that interference effects in the material cause the wave reflected from the top surface of the anti-reflection coating to be out-of-phase with the wave reflected from the semiconductor surface [21]. These out-of-phase reflected waves interfere destructively with one another which results in net zero reflection.

We have developed an ultra-thin WS_2-based photovoltaic model for space applications. It is beneficial to have the total active layer thickness around 100-200 nm to minimize radiation damage without using additional radiation shielding structures. Solar cells with thick active layers are susceptible to radiation-induced damage from high energy radiation and particles in space; ultra-thin materials are much more resistant to radiation damage with considerably less degradation of performance. We have incorporated an additional light trapping structure and an appropriate anti-reflection coating layer in our photovoltaic model to propose an experimentally feasible device structure with performance comparable to existing space solar cells.

1.4 Tunability and Variability of Electronic Properties of 2D Materials

TMDCs have the unique advantage of flexibility and tunability of their structure and composition, which can allow for controlled variations of their physical and chemical properties. TMDCs have the potential to be more versatile due to the possibility of fine-tuning their properties and features. The band gap of TMDCs plays a key role in their electronic properties and device-level applications, such as field effect transistors, photodiodes, phototransistors and solar cells [22]. It is well known that TMDCs exhibit variation of their band gaps depending on the number of layers [5]. Tunability of the bandgap enables controlled modification of the optical absorption and electronic features, which can enhance optoelectronic device performance [23].

Some ways to achieve tunability of properties are ion intercalation [24], addition of biological species [25] and by chemical doping [26]. However, there are limitations of large-scale variations and modifications in terms of efficient distribution of dopants, the range of variations of the properties, and the applicability to a large number of materials in the family [27], [28]. Bandgap modulation of TMDCs by the formation of hybrid alloys has been studied both theoretically and experimentally [29]–[32], with good thermodynamic stability at room temperatures [33], [34].

Recent studies have shown that the band structure of monolayer MoS_2 can be modified and tuned by substituting sulfur atoms with other chalcogen elements to form hybrid alloys [35]; this allows for a mechanism of tunability for modifying the physical and chemical properties of MoS_2. Large-scale synthesis of high quality and uniform alloys of Mo-based TMDC alloys with several hundred micrometer area is possible by chemical vapour deposition (CVD) to achieve bandgap tunability over a large energy range [36].

It is possible to obtain alloys of TMDCs by altering their composition to contain more than one kind of chalcogen atoms [37]–[39], leading to the formation of hybrid TMDCs with tunable electronic and optical properties. We have investigated tungsten-based TMDC alloys containing both sulfur and selenium atoms, whose electronic properties are intermediate of tungsten disulfide (WS_2) and tungsten diselenide (WSe_2) with tunable direct bandgaps dependent on the sulfur and selenium concentrations.

Ultrathin 2D materials for photovoltaics have gained considerable interest; but it also essential to have robust materials which are resistant to atmospheric conditions. Transition metal oxides have significant potential for photovoltaic applications as a wide bandgap semiconductor [40], [41]. Transition metal oxides are very sturdy and resistant to atmospheric extremities. Tungsten trioxide (WO_3) is a very versatile material; it can be deposited on and is compatible for fabrication with many semiconductors. It also has strong absorption for high energy photons. The electronic properties of WO_3 were investigated to study the unique features of this material and explore possible electronic and optical applications. The electronic properties of WO_3 make it suitable for implementation as a wide-bandgap semiconductor in solar cells. It can be used in tandem with existing solar cells, or as the top junction of a multi-junction solar cell.

1.5 Photovoltaics beyond the Shockley-Queisser Limit

Since its discovery in the 1960s, the Shockley-Queisser (S-Q) efficiency limit has generally been viewed as a fundamental limit on the performance of conventional photovoltaic devices, because the detailed balance principle defines a non-trivial loss associated with the radiative recombination process [42], [43]. After decades of progress, recent work has brought certain high-performance photovoltaics made from multiple materials within several percent of this limit [44]. Solar cells have been shown to exhibit strong internal and external luminescence as they approach the S-Q limit, which limits their maximum efficiencies [45].

Concentrators are the most straightforward approach to increase the S-Q efficiency, but generally require operating at high temperatures, or with large cooling structures, and have not been widely adopted commercially [46]. Solar cells composed of nanophotonic structures have also been widely studied to help extend the S-Q limit (e.g., by restricting the range of incident angles for increased open circuit voltage), but current experimental devices have significant limitations in achieving higher efficiencies and stability [47]–[49]. As a result of these constraints, there has been a growing interest in many unconventional materials and approaches with the potential to break the S-Q limit [50], [51].

Arguably, the most successful approach is multijunction photovoltaics, where the solar spectrum is split by stacking materials with different bandgaps [52]. However, the cost of publicly known fabrication approaches can be orders of magnitude higher than single junctions [53]. In a related approach, multiple spectrum solar cells transform the broad solar spectrum to a narrow range of photon energies, such as in thermophotovoltaics [54]; however, a major challenge is in obtaining higher efficiency devices. Multiple absorption is a mechanism where a single, high-energy photon generates multiple electron-hole pairs for higher efficiencies [55], but there is significant difficulty in the subsequent transport and collection of carriers. Another approach to obtain increased incident energy absorption is hot carrier extraction [56], but a major challenge is fabricating a device to efficiently extract this excess energy.

It is also possible to obtain AC solar cells by treating the incident photons as electromagnetic waves, as demonstrated in optical rectennas [57], but scaling such devices to optical frequencies is a major technical challenge. Upconversion of sub-bandgap energy photons

is a novel method of absorbing incident photons which otherwise cannot be absorbed [58], but it comes with major challenges such as long-term stability and absorption of excited photons. Another approach uses multiple energy levels for demonstrable increases in photon absorption, such as intermediate band solar cells [59] and quantum well solar cells [60].

In our work, we have presented another approach based on multiple energy levels in our absorber. While most prior techniques use these levels to increase photon absorption, our approach does not expect increased absorption. Instead, our approach uses the newly-formed energy levels to greatly reduce carrier recombination for more efficient carrier extraction. This allows for higher photon-to-current conversion with previously demonstrated levels of photon absorption. As inspired by the Shockley-Queisser efficiency limit, a natural direction of designing high efficiency photovoltaic systems is to reduce the carrier recombination rate. To this end, recent research has investigated the possibility of using quantum effects in chromophore complexes to improve solar cell performance [61]–[67].

Optically dark states created by dipole-dipole interaction between molecular excited states can reduce radiative recombination in exciton transfer, effectively increasing the photocell efficiency [61]–[65], [68]. Dark states have been observed across a wide range of experiments, resulting in dramatic, readily observable effects. Electromagnetically-induced transparency in atoms with 2 pairs of nearly degenerate transitions give rise to dark and light states with orders of magnitude difference in transmission through condensates of these atoms [69]. Similarly, dark states in polaritons have been observed experimentally to cause dynamic light trapping of incident light pulses [70]. Dark states can also be observed in molecular systems to give rise to unusually efficient luminescence of solid-phase emitter molecules [71].

A dark state is an electronic state of an atom, molecule or material that cannot directly absorb (or emit) photons. It is well known that, in general, electronic systems can transition from one energy level to another by emitting or absorbing one or more photons. However, not all transitions between arbitrary states may be allowed in certain materials. An experimental signature can be observed when a laser is used to excite atoms, which then spontaneously decay into a state that is not coupled to any other level by the laser light, preventing the atom from absorbing or emitting light from that state. This state, where a photon can be neither absorbed nor emitted, is

described as a dark state. A dark state can also arise from quantum interference due to additional interactions between the excited states of identical molecules, such as dipole-dipole interactions.

Recent studies have investigated dark states created by dipole-dipole interaction between molecular exciton states in chromophore complexes, which can increase the photocell efficiency by protecting the excitation from radiative recombination [61]–[68]. Such interactions and the formation of stable bright and dark states are widely observed phenomena in experimental studies of pigment-protein complexes in photosynthesis and have been associated with the very high exciton capture efficiency in such processes. Although these studies point to a promising design principle for artificial photocells, they are quite limited to elementary models consisting of few interacting chromophore centers, and the dark state protection mechanism has not been applied to a specific material-based photovoltaic model.

In our proposed photovoltaic system, we have investigated the possibility of creating dark states in a realistic material to enable dark state protection and increase photocell efficiency with a realistic material model to facilitate experimental realization. We have used a photovoltaic model based on pure and hybrid TMDCs to demonstrate the dark state protection mechanism's ability to enhance the photocurrent by suppressing radiative recombination, thus getting closer to an actual material design to overcome the Shockley-Queisser limit.

1.6 Overview of Dissertation

In Chapter 2, we have investigated the fundamental electronic and optical properties, such as band structure and absorption coefficients, of WS_2 to develop the foundations of device level applications, and understand the benefits and limitations of device level integration in new and existing technology. Using these calculated properties, we have investigated and developed photovoltaic models based on WS_2 in Chapter 3. We have demonstrated applications of our models for both terrestrial and space environments, and explored niche applications of solar cells based on ultra-thin WS_2. Our proposed photovoltaic models have the potential to exhibit performance comparable to existing commercial solar cells. In Chapter 4, we have investigated an ultra-thin solar cell model developed in Chapter 3 and introduced additional features in the structure to obtain a high efficiency device. We have incorporated a light trapping structure and an anti-reflection coating layer in our device model to obtain a high efficiency ultra-thin solar cell.

In chapter 5, we have explored hybrid TMDC alloys and oxides based on tungsten to study the unique features of these material and explore possible electronic and optical applications. We have investigated monolayers of tungsten-based TMDC alloys containing sulfur and selenium, which exhibit composition-dependent tunable electronic and optical properties. In Chapter 6, we have developed a photovoltaic model based on pure and hybrid TMDC materials to demonstrate dark state protection and corresponding enhancement of the output photocurrent, with the potential to overcome the Shockley-Queisser limit.

2. ELECTRONIC AND OPTICAL PROPERTIES OF MONOLAYER, BILAYER AND BULK TUNGSTEN DISULFIDE (WS_2)

2.1 Background

Tungsten disulfide (WS_2), a transition metal di-chalcogenide (TMDC), is an important 2D layered material which has attracted a great deal of interest in recent years. It has significant chemical and physical properties which makes it attractive for a variety of electronic and optical applications. It has a band gap of 1.3–2.2 eV depending on the structure geometry and thickness, well within the range of photovoltaic materials. Its 2D layered structure makes it possible to modify and tune its electronic properties by doping with other atoms or molecules between weakly bonded layers. It is also possible to apply external force to modify its structure, and hence, its electronic properties. WS_2 has significant absorption of incident photons with energies above its bandgap, making it a good absorber of incident photons. It also exhibits excellent carrier transport properties, as demonstrated by typically high mobility values. Its favorable electronic and optical properties make it a strong candidate for photovoltaic applications.

Another material of the same family, molybdenum disulfide (MoS_2), has similar promising electronic, physical, and chemical properties. But tungsten-based compounds are more stable, robust, and resilient on exposure to extreme environmental and working conditions. My aim is to propose a material which not only has promising and favorable properties but is also suitable for implementation in a variety of applications under diverse operating conditions. For photovoltaic applications particularly, it is necessary that the constituent materials are stable in harsh environmental conditions and are resistant to exposure from temperature fluctuations, humidity variations and particulate matter. It is in these aspects that WS_2 stands out among other candidates and warrants detailed investigation of its properties and potential applications.

The first step in studying the properties of WS_2 is to correctly understand the overall structure of WS_2, both from a unit cell and supercell aspects. Investigating the fundamental unit

This work has been presented in *Optics for Solar Energy*, pp. OM2D-4. Optical Society of America, 2018.

It has also been published in *Solar Energy Materials and Solar Cells*, 174 (2018): 370-379.

cell allows us to study the fundamental electronic and optical properties of the material. It is critically important to identify the smallest unit cell, as it is helpful in extending our understanding of the fundamental properties to large-scale systems based on extended sheets and blocks of the material. Understanding the structure and properties at the macro level enables us to explore its stability and suitability for incorporation in device-level applications.

It is essential to study the fundamental electronic properties of WS_2 in order to progress to device level applications, and understand the benefits and limitations of device level integration in new and existing technology. The most fundamental feature of a semiconductor is the electronic band structure, which gives us a lot of vital information such as bandgap, nature of electronic transitions, density of states for excited carriers and absorptivity of incident photons. The electronic band structure gives us an insight into the nature of the material, such as conductivity of electrons and absorptivity of incident radiation.

The Kronig-Penney model demonstrates the evolution of energy bands as well as energy band gaps from a simple one-dimensional periodic potential [72]. Although it is an overly simplified model w.r.t the three-dimensional potential and band structure of an actual semiconductor crystal, it is an instructive tool to demonstrate and understand how the band structure of a material can be calculated for a periodic potential, and how allowed and forbidden energies are obtained when solving the corresponding Schrödinger equation [73].

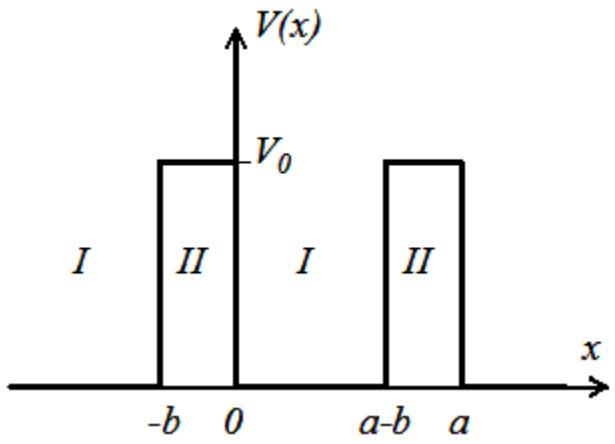

Figure 5. The periodic potential assumed in the Kronig-Penney model. The potential barriers with width *b* are spaced by a distance (a-b), and repeated with a period *a* [73].

The Kronig-Penney model assumes a periodic potential as shown in Figure 5. It consists of an infinite series of rectangular potential energy barriers with height V_0 and width b, separated by a distance (a-b) resulting in a periodic potential with period a. Solutions to this problem are given as Bloch functions, where traveling wave solutions are multiplied with a periodic function which has the same periodicity as the potential [72].

More specifically, solutions for k and E are obtained when the following equation is satisfied:

$$\cos ka = F = \frac{\alpha^2 - \beta^2}{2\alpha\beta} \sinh \alpha b \sin \beta(a-b) + \cosh \alpha b \cos \beta(a-b)$$

where

$$\alpha = \frac{\sqrt{2m(V_0 - E)}}{\hbar} \qquad \beta = \frac{\sqrt{2mE}}{\hbar}$$

This equation can be further simplified for the case where the barrier is a delta function with area $V_0 b$, when it becomes:

$$\cos ka = F = P\frac{\sin \beta a}{\beta a} + \cos \beta a$$

where

$$\beta = \frac{\sqrt{2mE}}{\hbar} \qquad P = \frac{mV_0 ba}{\hbar^2}$$

This equation can be solved numerically, and only if the function F is between -1 and 1 since it has to equal cos(ka). The energy E is plotted as function of ka/p and the function F in Figure 6. The corresponding band structure is shown in Figure 7.

From Figure 7(A), it can be seen that the $E(k)$ relation resembles a parabola except that only specific ranges of energies are valid solutions to Schrödinger's equation and therefore are allowed, while others are not. The range of energies for which there is no solution is referred to as an energy band gap; this is how the evolution of band gaps take place. The transitions between allowed and forbidden energies occur at non-zero integer multiples of ka/π. These correspond to local minima and maxima of the $E(k)$ relation. The reduced-zone diagram shown in Figure 7(C) shows the first three bands and energy bandgaps.

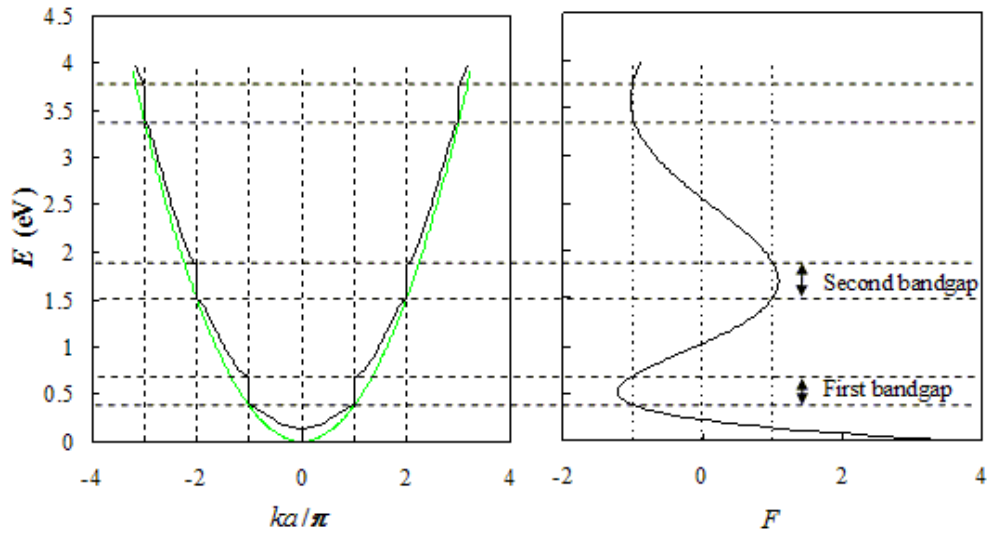

Figure 6. Solution to the Kronig-Penney model for a = 1 nm and V_0b = 0.2 nm-eV; energy E versus ka/π and F, which equals cos(ka), from which the allowed energies can be identified [73].

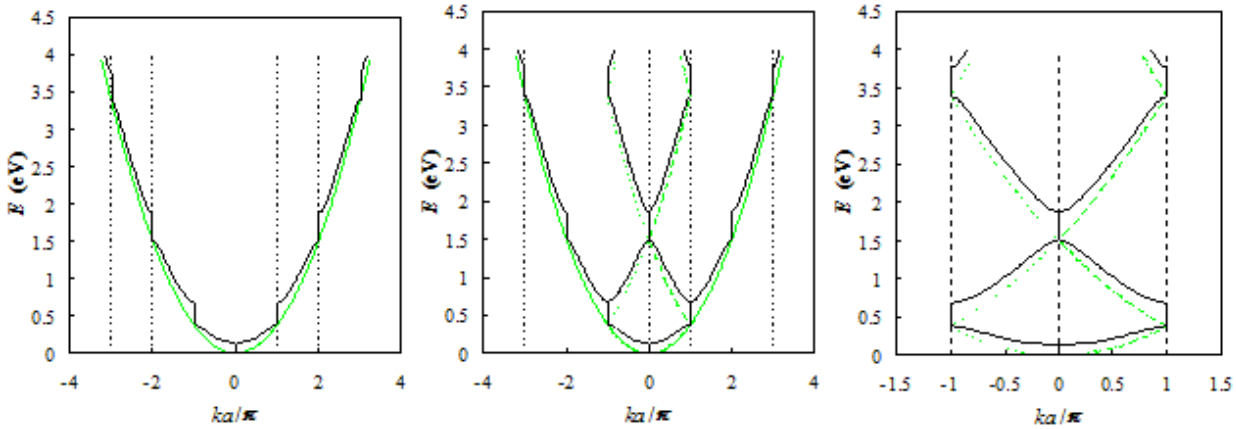

Figure 7. Energy versus ka/π. (A) the E(k) diagram, (B) the E(k) diagram combined with the reduced-zone diagram, and (C) the reduced-zone diagram only [73].

Starting with the band structure, additional properties such as effective density of states for carriers and absorption coefficient for incident photons can be calculated. These properties give us a deep insight into possible applications of these materials. Using these properties, we can progress towards understanding and investigating device-level applications of WS_2 in conjunction with existing technology and also exploring new technological advances.

2.2 Theory and Methods

2.2.1 Structure of Tungsten Disulfide (WS_2)

A sheet of WS_2 consists of a layer of hexagonally arranged W atoms sandwiched between two layers of hexagonally arranged S atoms [74]–[76]. The thickness of a single layer of WS_2 is 3.2 Å, while multiple layers are separated from each other by empty space of separation 2.96 Å. There are strong W-W, S-S and W-S covalent bonds within a layer, while adjacent layers are held together by weak inter-layer attraction from van der Waals' forces. The fundamental unit cell of WS_2 has a trigonal prismatic structure as shown in Figure 8. The lattice parameter *a* is 3.154 Å, as determined by single-crystal electron diffraction [75].

A primitive unit cell consists of one W atom and two S atoms in a trigonal prismatic configuration [74], [75], [77], [78]. Due to the weak nature of inter-layer attractions, it is possible to obtain individual layered sheets of WS_2 and other TMDCs containing any desired number of layers. This feature of TMDCs make them versatile 2D materials with the ability to tune their properties by controlling the number of layers in the structure. We can obtain any structure ranging from a single monolayer and bilayer materials to a bulk material with multiple sheets of layers. The electronic and optical properties of the material depend strongly on the number of layers present in the structure.

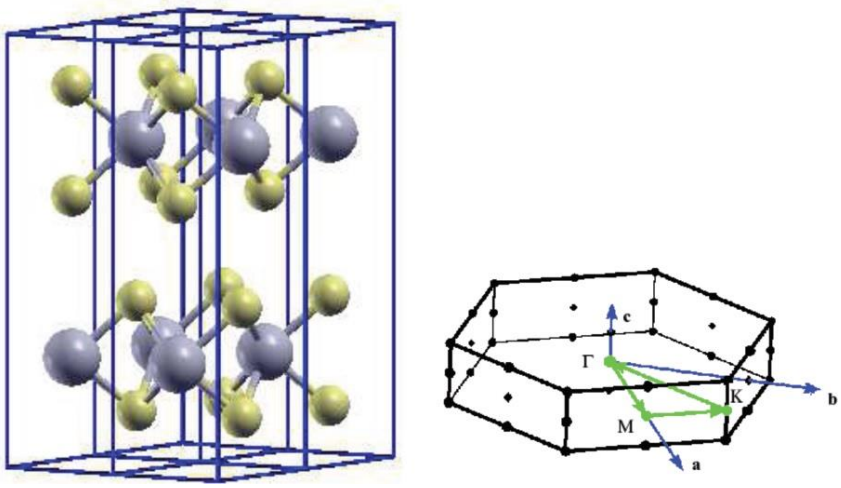

Figure 8. Left: illustration of the WS_2 structure where the big and small balls represent W and S atoms, respectively. Right: the corresponding Brillouin zone where the k path used to plot the band structure diagram is also shown (adapted from [74]).

2.2.2 Electronic Band Structure of Tungsten Disulfide from DFT and GW Calculations

The electronic band structure of monolayer, bilayer and bulk WS_2 were investigated. Electronic band structure is one of the most fundamental properties of a material and is the foundation for understanding its various electronic and optical properties. Density functional theory (DFT) was used to obtain the preliminary band structure of WS_2. DFT is a computational quantum mechanical modeling method used in physics, chemistry, and materials science to solve the Schrödinger equation [79] and investigate the electronic structure (density of states, band structure, etc.) of many-body systems, in particular atoms and molecules [80], [81]. Using this theory, the properties of a many-electron system can be determined by using functionals, i.e., functions of another function, of the spatially dependent electron density. DFT is among one of the most popular and powerful methods employed in solid-state physics, computational physics, and computational chemistry, for solving the many-body Schrödinger equation [82].

For a many-body electronic structure calculation, the nuclei of the treated molecules or clusters are represented as an electrostatic potential *V*, in which the electrons are moving. A stationary electronic state is then described by a wavefunction $\Psi(\mathbf{r}_1,\ldots,\mathbf{r}_N)$ satisfying the many-electron time-independent Schrödinger equation with the N-electron Hamiltonian, which included electron-electron interactions:

$$\hat{H}\Psi = \left[\hat{T} + \hat{V} + \hat{U}\right]\Psi = \sum_i \left[-\frac{\hbar^2}{2m}\nabla_i^2 + V(r_i) + \sum_j U(r_i, r_j)\right]\Psi = E\Psi$$

where, for the *N*-electron system, $\hat{H}$ is the Hamiltonian, *E* is the total energy, $\hat{T}$ is the kinetic energy, $\hat{V}$ is the potential energy from the external field due to positively charged nuclei, and $\hat{U}$ is the electron–electron interaction energy. The operators $\hat{T}$ and $\hat{U}$ are universal operators, as they are the same for any *N*-electron system, while $\hat{V}$ is a non-universal system-dependent operator [83].

It is possible to write all functions in terms of particle density:

$$n(r) = N\int d^3 r_2 \ldots\ldots \int d^3 r_N |\Psi(r_1, r_2, \ldots\ldots, r_N)|^2$$

Now the system energy becomes:

$$E[n] = T[n] + U[n] + \int d^3 r\, V(r) n(r)$$

where *T[n]* and *U[n]* are universal functionals and *V[n]* is a non-universal functional. Electron correlations mean greatest difficulty is in evaluating *V[n]*.

At the molecular level, solids can be often approximated as homogeneous electron gas immersed in a uniformly positive charged background. In this limit it is known that exchange and correlation (X-C) effects are local in character and the X-C energy is simply the integral of the X-C energy density at each point in space assumed to be the same as a homogeneous electron gas with that density. One well-known strategy involves local density approximation (LDA):

$$E_{XC}^{LDA}[n] = \int d^3r\, n(r)\, \varepsilon_{XC}(n)$$

The LDA assumes that the density is the same everywhere. Because of this, the LDA usually underestimates the exchange energy and overestimates the correlation energy. The errors due to the exchange and correlation parts tend to compensate each other to a certain degree. To compensate for this behavior, it is common to expand in terms of the gradient of the density in order to account for the non-homogeneity of the true electron density. This allows corrections based on the changes in density away from the reference location. These expansions, referred to as generalized gradient approximations (GGA), consists of functionals that depend both on the magnitude of the density *n(r)* and of its gradient $|\nabla n(r)|$:

$$E_{XC}^{GGA}[n_\uparrow, n_\downarrow] = \int d^3r\, n(r)\, \varepsilon_{XC}(n_\uparrow, n_\downarrow, \nabla n_\uparrow, \nabla n_\downarrow)$$

The DFT calculations were performed using the open-source code Quantum ESPRESSO [84], [85]. Quantum ESPRESSO is a quantum mechanical modeling tool to simulate many-body systems, using first-principles electronic-structure calculations and materials modeling. DFT calculations require pseudopotential files which simulate selected atoms from the periodic table. The pseudopotentials developed for Quantum ESPRESSO were used in our simulations. It is very important to correctly define the unit cell, such as position of atoms and cell dimensions, and use appropriate pseudopotential files. The unit cell, as defined in the input file, is simulated using periodic boundary conditions, such that the unit cell is copied in all directions in the 3D space for the calculations to give the results for an extended material system.

The most basic pseudopotentials (PPs) are obtained by LDA approach where the exchange energy per particle in each spatial point is taken as the exchange energy per particle from a uniform electron gas with a density equivalent to the density in this same point, e.g., Perdew-Zunger (PZ) PPs [86]. GGA PPs are obtained by adding gradient corrections to the LDA approach, e.g., Perdew-Burke-Ernzerhof (PBE) PPs [87]. We used LDA PPs in our initial calculations to validate the procedure and computational methods. For the final simulations, GGA PPs were used to simulate W and S atoms for better accuracy of the results.

The unit cell of WS_2 when periodically extended in the 2D plan simulates an extended sheet of the material. The materials were modeled as cuboidal slabs by including a vacuum region in the direction perpendicular to the surface. This allows for negligible interactions between the adjacent layers during the calculations. It has been observed that a vacuum space of 10 Å or more gives accurate results for simulations of independent, isolated sheets. We have used vacuum spacing of 20 Å for additional accuracy in the simulations.

Since WS_2 has a thin 2D structure, there is no electronic dispersion in the vertical out-of-plane direction. Thus, a horizontal sampling in the x-y plane of the first Brillouin zone is sufficient to obtain accurate electronic dispersion. The Brillouin zone was sampled according to the scheme proposed by Monkhorst-Pack [88] with a high-density in-plane 20x20x1 k-point grid with 400 k-points. The bands were plotted along the k-point path as in Figure 8 (right, green). The k-point path chosen covers all the significant high-symmetry points in the Brillouin zone; it gives an accurate plot of the important and notable features of the electronic band structure.

The band structure obtained from DFT gives accurate information about the shape of the energy bands, such as valence band maximum (VBM), conduction band minimum (CBM) and other local extrema. But a well-known major problem of DFT is that the bandgap of the material is significantly underestimated. The major reason behind this issue is that the calculated relative locations of the VBM and CBM w.r.t. vacuum are very poor estimates, thus, resulting in inaccurate predictions for the ionization potential *I*. A theoretically rigorous way to solve the issue of band gap underestimation is to go beyond the DFT results and formulating the electronic band structure using the GW approximation; it involves the expansion of the self-energy in terms of the single

particle Green's function *G* and the screened Coulomb interaction *W* to model the electronic properties of many-body systems [74], [89]–[92].

From DFT calculations, the ionization potential of the material can also be obtained, which is the difference between the electrostatic potential in the vacuum region (V_{vac}) and the DFT band energy at the valence band maximum ($\boldsymbol{\varepsilon}_{\mathrm{VBM}}$):

$$I^{DFT} = V_{vac} - \boldsymbol{\varepsilon}_{VBM}$$

For molecular systems, it is a well-known problem that the highest occupied molecular orbital (HOMO) energy in LDA/GGA gives a very poor approximation of the ionization potential due to the self-interaction error in the LDA/GGA X-C potential. Although DFT with LDA/GGA X-C functionals cannot describe the band gaps and ionization potentials accurately, it can give an accurate prediction of the band gap center (BGC), or the average of the energies at VBM and CBM. The GW corrected ionization potential can be defined as:

$$I^{GW} = \left[V_{vac} - \frac{1}{2}\left(\boldsymbol{\varepsilon}_{VBM} + \boldsymbol{\varepsilon}_{CBM}\right)\right] + \frac{1}{2}E_G^{GW}$$

where E_G^{GW} is the GW fundamental band gap system.

The results from DFT calculations were used as the starting point for the GW calculations; the simulations were carried out using the GWL package in Quantum ESPRESSO [84], [93]. The bandgap energy correction value was obtained from the GW approximation, which when added to the DFT bands gave the accurate band structure of bulk WS_2 matching with experiments [74]. The GW calculation is computationally intensive; so, it is much more efficient to perform the calculation for a single k-point instead of the entire Brillouin zone.

In summary, the first step is to run a DFT calculation over a specific k-point path to obtain the preliminary band structure; the next step is to use the DFT simulation results and run a GW calculation over a single k-point in the original k-point path. I have used the Γ-point of the k-point path as reference in my calculations. The energy gap between the conduction and valence bands at the Γ-point obtained using the DFT calculation results is lower than the actual experimental value. The GW-corrected band structure gives the accurate energy gap. The energy difference between the GW-corrected energy gap and the DFT energy gap is the essential bandgap correction. This bandgap correction energy when added to the DFT-obtained bandgap gives the accurate band

structure matching with experiments. This is a very accurate method to obtain the electronic band structure for bulk materials.

However, for a material of WS_2 consisting of only a few layers, namely monolayer and bilayer, it is important to include the excitonic effect due to the exciton binding energy [94]. The bandgaps of monolayer and bilayer WS_2 obtained by DFT calculations followed by adding the GW corrections are significantly higher than experimental results. The large overestimation in these structures is due to the large excitonic effect in a two-dimensional system. This is a well-known issue for 2D TMDCs in general. Subtracting the excitonic effect energy correction from the DFT+GW bands gives a very accurate band structure and bandgap prediction, matching closely with experimental results obtained via spectroscopic ellipsometry and electrochemical cyclic voltammetry [5], [94]–[96].

The DFT calculations and GW approximation were first attempted with known materials to become familiar with the calculation methods and the Quantum ESPRESSO tool. Preliminary calculations were performed with silicon to validate our procedure. The results obtained from the simulations with silicon were comparable to established results. The bandgap of bulk silicon obtained from DFT calculations was found to be 0.6 eV; the bandgap correction energy obtained from the GW calculations was found to be 0.54 eV. The actual bandgap, obtained by using the DFT-calculated band structure followed by inclusion of the GW correction, was calculated to be 1.14 eV which is very close to the actual bandgap of 1.12 eV [72]. All the calculations and simulations were carried out assuming a temperature of 300 K.

2.2.3 Absorption Coefficient Calculation

From the electronic band structure, the real and imaginary parts of the dielectric function (ε) of WS_2 can be calculated which gives us important information about the dielectric permittivity and absorptivity of the material. The real part of the epsilon data gave the relative dielectric constant of the monolayer, bilayer and bulk WS_2. Using the real and imaginary parts of the epsilon data, the values of the absorption coefficient (α) at the corresponding energies were calculated [97], [98] for WS_2. The plot of the absorption coefficient against energy gives a very clear picture of the photon energies which are most likely to be absorbed by the different structures of WS_2, and aid in the design of a suitable photovoltaic absorber material for potential future applications.

The absorption coefficient was calculated for monolayer, bilayer and bulk WS_2 materials. The band structure and energy data from the initial DFT results were used in post-processing calculations in Quantum ESPRESSO to obtain the real and imaginary parts of the dielectric tensor (ε) [99], [100]. The calculations were carried out using an energy range of 0 to 4 eV which covers the energy of visible light and incoming photons in the incident solar radiation on Earth. Increments of 0.01 eV in energy were used in the calculations to obtain accurate results for absorption coefficient. A thermal broadening of about 0.1 eV energy was used with the calculated results of the dielectric tensor to obtain realistic values of the absorption coefficient matching with experimental measurements, since it is much easier and more probable to take measurements at increments of 0.1 eV rather than 0.01 eV.

Initially, to test the validity and accuracy of the calculation method, the dielectric permittivity (ε) and absorption coefficient (α) of crystalline silicon (c-Si) was calculated using our model and compared with the established literature values. The results obtained with silicon were compared with data from the PhotonicsDB tool [101] on nanoHUB [102], which match the Handbook of Optical Constants of Solids [103]; the close similarity between our calculated results and the existing literature data confirm the validity and accuracy of the model. All the calculations and simulations were carried out assuming a temperature of 300 K.

2.2.4 Additional Properties of Tungsten Disulfide

From the electronic band structure results, the electron and hole effective masses were calculated from the band structure data of monolayer, bilayer and bulk WS_2, using $\frac{1}{m^*} = \frac{1}{\hbar^2}\frac{\partial^2 E}{\partial k^2}$. The effective mass values were then used to calculate the conduction band effective density of states N_C and the valence band effective density of states N_V [104].

$$N_C = 2\left(\frac{2\pi m_e^* k_B T}{h^2}\right)^{\frac{3}{2}}$$

$$N_V = 2\left(\frac{2\pi m_h^* k_B T}{h^2}\right)^{\frac{3}{2}}$$

These parameters give an accurate estimate of the maximum concentration of carriers that can be accommodated in the conduction band and valence band, respectively. We also get an

indication of the limits of carrier generation and dopant concentration, which are important considerations necessary for device-level design and implementation.

2.3 Results and Discussion

The DFT simulations of bulk WS_2 using Quantum ESPRESSO gave the initial band structure along the first Brillouin zone the bandgap was found to be 0.97 eV. A big limitation here is the value of the bandgap obtained (0.97 eV), which is significantly underestimated by DFT calculations. Using the dispersion and energy values obtained from the results of DFT calculation, the GW approximation gave the required bandgap energy correction (0.32 eV) to obtain the accurate bandgap. This correction, when added to the DFT results, gave the correct bandgap and band structure (Figure 9) matching with established results [74]. Bulk WS_2 was found to be an indirect bandgap material exhibiting a bandgap of 1.29 eV, with direct transition starting around 2.2 eV.

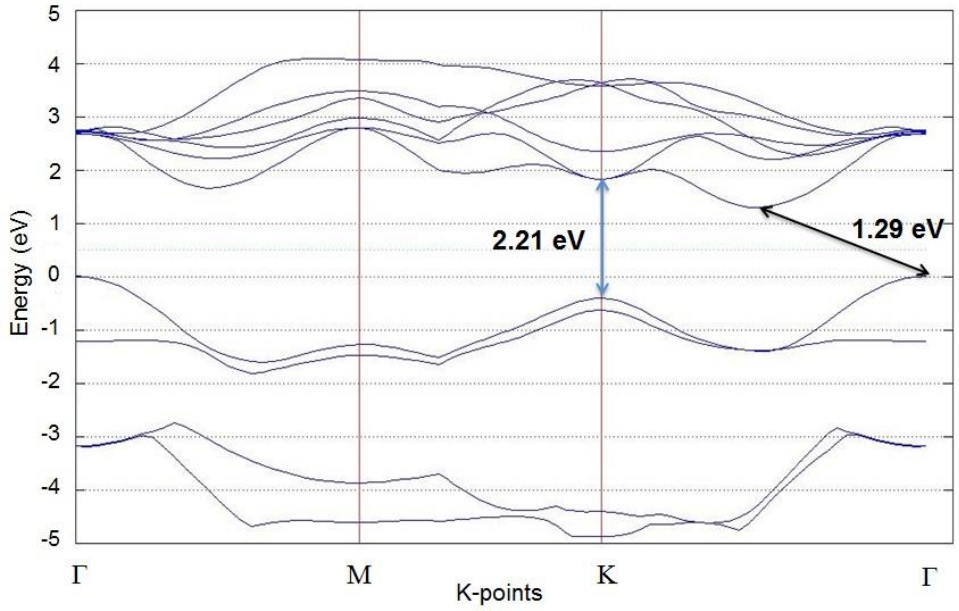

Figure 9. Band structure of bulk WS_2 showing indirect bandgap of 1.29 eV with direct transition possible at 2.21 eV.

The bandgap of WS_2 is similar to a typical photovoltaic material, which makes it a very good candidate for use in a solar cell. The band structure has a few interesting features in addition to the photovoltaically significant band gap. Both indirect and direct optical transitions can occur

in this material, depending on the energy of the incoming photon in the incident radiation. The electronic dispersion determines the relative location of the CBMs and VBMs, which correspond directly to the strength of these transitions. Subsequently, the regions where strong photon-electron interactions take place can be understood and an appropriate structure can be designed.

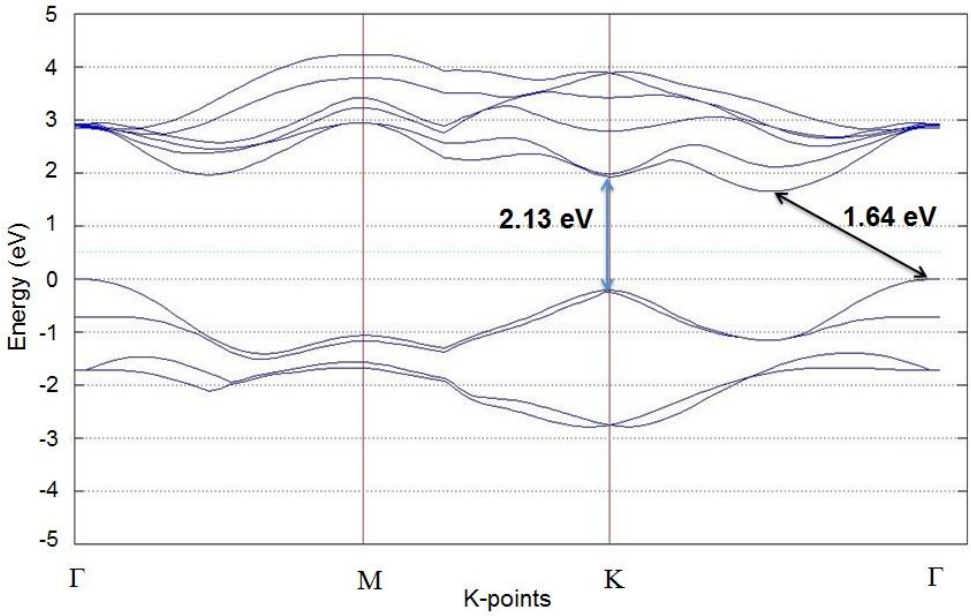

Figure 10. Band structure of bilayer WS_2 showing indirect bandgap of 1.64 eV with direct transition possible at 2.13 eV.

The band structures of bilayer and monolayer WS_2 were obtained using DFT calculations followed by inclusion of GW corrections and excitonic effects (Figure 10 and Figure 11, respectively). The bandgap of the bilayer WS_2 material was found to be 1.42 eV (indirect) from DFT calculations; the GW correction obtained was 0.64 eV which had to be added to the DFT results; and the exciton binding energy was calculated to be 0.42 eV which had to be subtracted from the GW-corrected band structure. Thus, bilayer WS_2 was found to be an indirect bandgap material exhibiting a bandgap of 1.64 eV, with direct transition starting around 2.13 eV.

The bandgap of the monolayer material was found to be 1.91 eV (direct) from DFT calculations; the GW correction obtained was 1.14 eV, which had to be added to the DFT results; and the exciton binding energy was calculated to be 0.9 eV which had to be subtracted from the GW-corrected band structure. Thus, monolayer WS_2 was found to be a direct bandgap material

exhibiting a bandgap of 2.15 eV. Based on the band structures, both monolayer and bilayer WS_2 can be considered suitable photovoltaic materials.

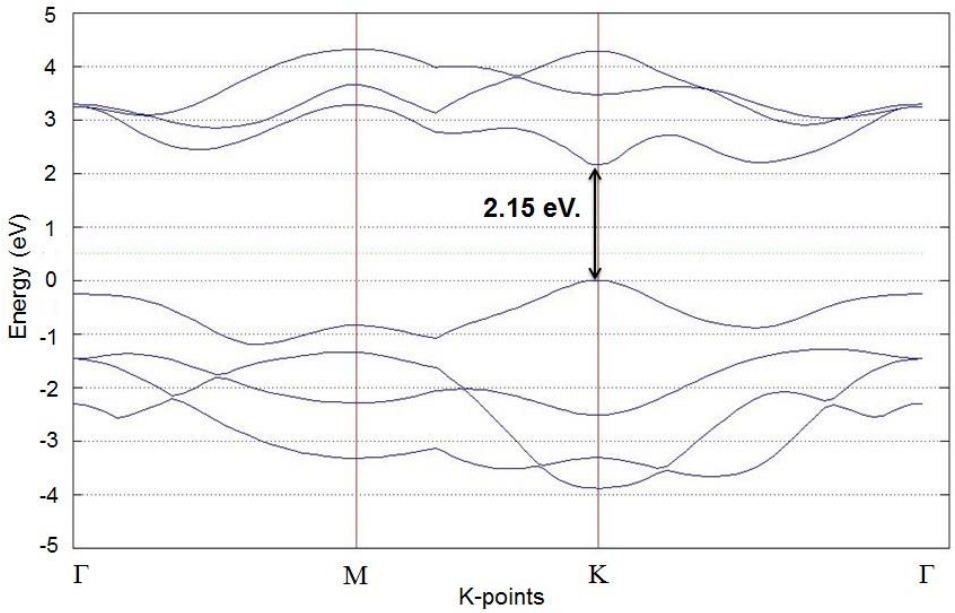

Figure 11. Band structure of monolayer WS_2 showing direct bandgap of 2.15 eV.

For all the calculations, the unit cells were defined to include a vacuum space of 20 Å above the layers, in order to simulate isolated layers and eliminate the influence of adjacent layers while using periodic boundary conditions. For the monolayer material, it was observed that a vacuum of 8 Å or higher was enough to obtain accurate simulation results without any multi-layer effect; the unit cells with 8 Å and 20 Å vacuum spacing gave identical results without interference from other layers above or below the unit cell. So, a spacing of 8 Å between successive WS_2 monolayers, where the W and S atoms are aligned in the same vertical axes respectively, can give a thick multi-layer stack of monolayer WS_2. Similarly, a vacuum space of 8 Å between pairs of WS_2 layers was used in the unit cell to obtain the accurate properties of a bilayer structure.

Using the energy eigenvalues and eigenvectors and the dispersion values from the DFT calculations, the real and imaginary parts of the dielectric permittivity ε were obtained for each of the monolayer, bilayer and bulk WS_2 materials. From the dielectric permittivity data, the relative dielectric constant (Table 1) and the value of the absorption coefficient α (μm^{-1}) for different energies of the incoming radiation for monolayer, bilayer and bulk WS_2 (Figure 12) were obtained.

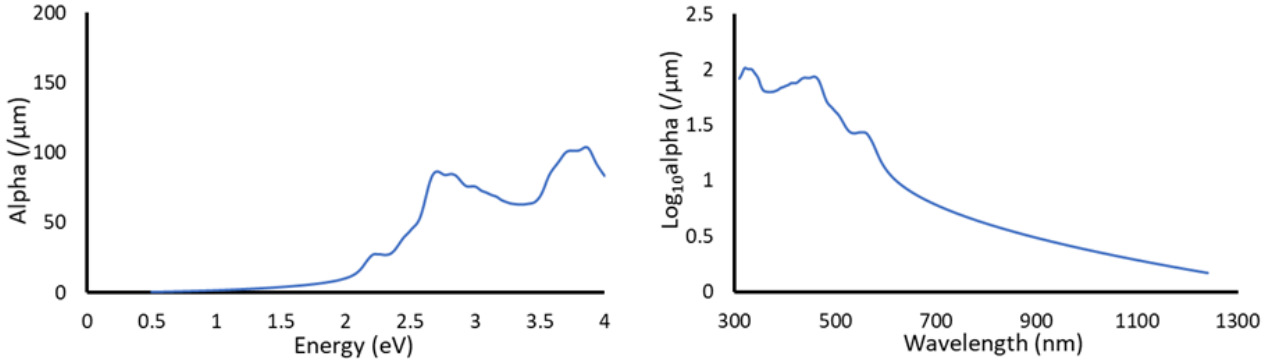

(A) Bulk WS_2

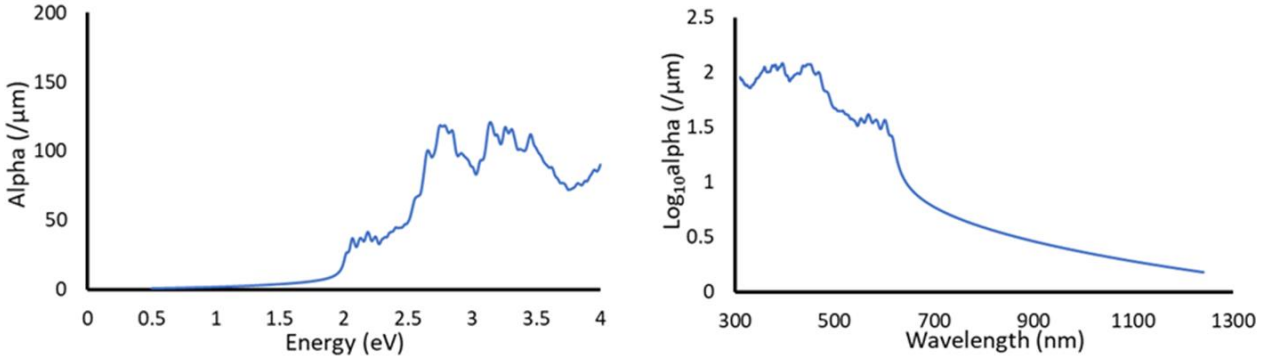

(B) Bilayer WS_2

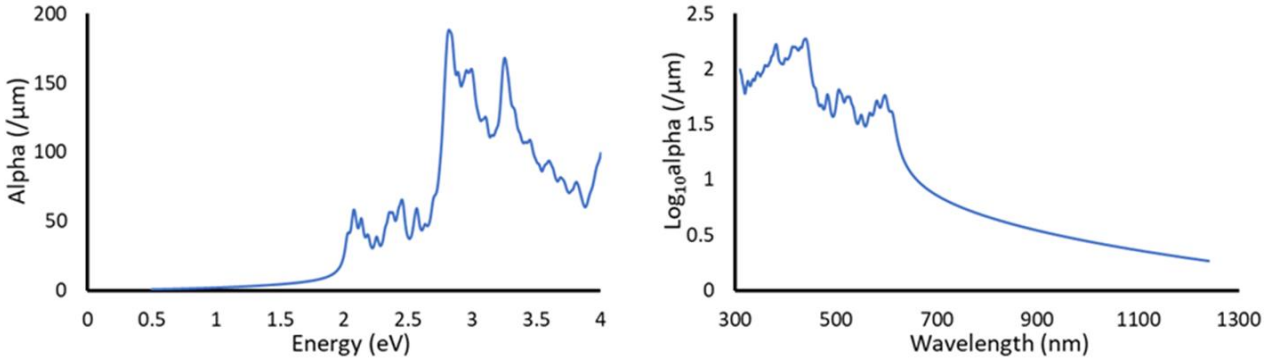

(C) Monolayer WS_2

Figure 12. Absorption coefficient α (/μm) vs. energy and wavelength for monolayer, bilayer and bulk WS_2.

Initial preliminary simulations were carried out with silicon to check for validity and accuracy of the calculation method; the dielectric permittivity (ε) and absorption coefficient (α) of crystalline silicon (c-Si) calculated using my model were consistent with existing literature. The next set of simulations were carried out and verified with well-known materials of the TMDC

family, namely MoS_2, for additional validation of the model and accuracy. The values of α obtained for MoS_2 are similar to the results reported in existing literature [105].

The values of α obtained show that there is significant absorption of incoming photons of energies above the direct transition energy value for monolayer, bilayer and bulk WS_2. Bulk WS_2 has decent absorption for photon energies above 2 eV. Bilayer WS_2 has better absorption for photons with similar energies, while monolayer WS_2 has the best absorption profile for photons with energies above 2 eV. The absorption profiles obtained for the different structures of WS_2 show that this material has good absorption of photons within the energy range of the incident solar radiation. This opens possibilities for implementation of WS_2 as a light absorbing material for photovoltaic applications.

Although the calculated absorption profiles show that there is some non-zero absorption for photons with energies below the bandgap energy, this scenario is realistically impossible and will not be observable in experimental demonstrations. In order to maintain consistency with experimental results and validation, all sub-bandgap absorption was neglected and the values of the absorption coefficient (α) for sub-bandgap energies were taken to be zero for future reference and device-level modeling.

Monolayer WS_2 has a direct bandgap of 2.15 eV; bulk WS_2 has an indirect bandgap of 1.3 eV, but direct transition is possible around 2.2 eV. There is high absorption above the direct transition energy, and very low absorption below that. If we look at the photoluminescence (PL) spectra of WS_2 [85], [106], we can observe a spike around the indirect bandgap energy for the bulk material while we see a spike around the direct bandgap energy for the monolayer material. Thus, we can have some photon absorption at the indirect bandgap energy for bulk WS_2, which is why we can consider bulk WS_2 to be an indirect bandgap material with a bandgap energy of 1.3 eV for future work and simulations.

From experimental observations, it is evident that there will be some photon absorption for energies between 1.3 eV and 2.2 eV for bulk WS_2 [105], [107]. This is our main reason to keep the calculated absorption coefficient values above the indirect bandgap (1.3 eV) and neglect all absorption for energies below this threshold. For monolayer WS_2, any photon absorption below its

direct bandgap energy (2.2 eV) is very unlikely, which is why we have used this energy value as its bandgap and neglected all absorption for energies below this threshold.

From the band structure data, the electron and hole effective masses were calculated for monolayer, bilayer and bulk WS_2. The effective mass values were then used to calculate the conduction band effective density of states N_C and the valence band effective density of states N_V. The calculated values are summarized in Table 1. The values of N_C and N_V obtained for the different structures are similar to those of many commonly used semiconductors, such as silicon and gallium arsenide. These parameters give us an accurate estimate of the limits of carrier generation and dopant concentration, which are important considerations necessary for device-level design and implementation.

The electronic properties and parameters of monolayer, bilayer and bulk WS_2 are summarized in Table 1.

Table 1. Summary of electronic properties of monolayer, bilayer and bulk WS_2.

	Monolayer WS_2	**Bilayer WS_2**	**Bulk WS_2**
Bandgap (eV)	2.15 (direct)	1.64 (indirect)	1.29 (indirect)
Direct Transition Energy (eV)	2.15	2.13	2.21
Conduction Band Effective Density of States N_C (cm^{-3})	$0.97*10^{19}$	$1.32*10^{19}$	$2.02*10^{19}$
Valence Band Effective Density of States N_V (cm^{-3})	$1.34*10^{19}$	$1.72*10^{19}$	$2.48*10^{19}$
Relative Dielectric Constant	5.1	7.5	13.4

2.4 Outlook and Conclusion

In this chapter, we have developed a DFT-based model to calculate the band structure and resulting key materials properties for various structures of WS_2, which have been validated against experimentally fabricated and characterized materials. The electronic and optical properties of

monolayer, bilayer and bulk WS_2 were calculated and analyzed for potential implementation in photovoltaic systems.

Bulk WS_2 was found to be an indirect bandgap material exhibiting a bandgap of 1.29 eV, with direct transition starting around 2.2 eV. Bilayer WS_2 was found to be an indirect bandgap material exhibiting a bandgap of 1.64 eV, with direct transition starting around 2.13 eV. Monolayer WS_2 was found to be a direct bandgap material exhibiting a bandgap of 2.15 eV. The electronic band structure and bandgap of monolayer, bilayer and bulk WS_2 are similar to a typical photovoltaic material, which makes them very good candidates for use in solar cells.

The values of the absorption spectrum $\alpha(\lambda)/\alpha(E)$ obtained for the different structures of WS_2 show that there is significant absorption of incoming photons with energies above the bandgap energy. The absorptivity is significantly higher for photons with energies higher than direct transition energy value for monolayer, bilayer and bulk WS_2. Bulk WS_2 has decent absorption for photon energies above 2 eV. Bilayer WS_2 has better absorption for photons with similar energies, while monolayer WS_2 has the best absorption profile for photons with energies above 2 eV. The absorption profiles of WS_2 show that this material has good absorption of photons within the energy range of the incident solar radiation on the surface of Earth. This enables implementation of WS_2 as a light absorbing material for photovoltaic applications.

These results show WS_2 has very favorable electronic and optical properties for use in photovoltaics, along with the natural advantages of the light weight, flexibility, and earth abundance of most TMDCs.

3. TMDC-BASED PHOTOVOLTAIC MODELS UNDER TERRESTRIAL AND SPACE SOLAR RADIATION

3.1 Background

Tungsten disulfide (WS_2), a 2D layered TMDC, has attracted a great deal of interest in recent research studies. It has significant and favorable electronic and optical properties which make it attractive for potential photovoltaic applications. The electronic band structure and corresponding bandgap, effective density of states for carriers, and absorption coefficient for incident photons of WS_2 are similar to many high-performance semiconductor materials used in existing photovoltaic technology. These properties present a great deal of promise for the potential implementation of WS2 in a solar cell design.

As we have established in Chapter 2, WS_2 has an electronically and optically favorable bandgap within the range of photovoltaic materials, which makes it a very good candidate for use in solar cells. The absorption coefficient of WS_2 shows that this material has good absorption of photons within the energy range of the incident solar radiation on the surface of Earth; This allows for implementation of WS_2 as a light absorbing material for photovoltaic applications. Its 2D layered structure enables modification and tunability of its electronic properties by doping with other atoms or molecules between weakly bonded layers. It also exhibits excellent carrier transport properties, as demonstrated by typically high electron and hole mobility values. In this work, we have used these calculated properties of WS_2 to progress towards understanding and investigating device-level applications of this unique material in a photovoltaic system.

Bulk WS_2 was used as the starting material for designing a solar cell device model. Using this as the baseline, monolayer WS_2 and amorphous silicon (a-Si) were added to improve the performance. The electronic properties of monolayer and bulk WS_2, absorption coefficient and other material parameters were taken from our results presented in Chapter 2. Using these results, a p-n junction solar cell was modeled and simulated using monolayer WS_2, bulk WS_2 and a-Si to

This work has been presented in *Optics for Solar Energy*, pp. OM2D-4. Optical Society of America, 2018.

It has also been published in *Solar Energy Materials and Solar Cells*, 174 (2018): 370-379.

obtain a structure similar to HIT (Heterojunction with Intrinsic Thin Layer) solar cells, which are known to have high efficiencies [108], [109]. The structure was simulated using the drift-diffusion model to obtain the device performance parameters such as open circuit voltage (V_{OC}), short circuit current (J_{SC}) and efficiency.

The primary device simulations which we have developed in this work are based on the terrestrial solar radiation on the surface of the Earth (AM 1.5G spectrum). The maximum device efficiency which we obtained from our models was 23.3%, with V_{OC} of 0.84 V and J_{SC} of 33.5 mA/cm^2. These values compare favorably with the best HIT silicon solar cells observed in experiments, with efficiencies around 25% [108].

In addition, we have also explored potential niche applications of our proposed solar cell model, where this material has the potential to outperform existing technology. We have investigated implementations of our WS_2-based solar cell model in space photovoltaic applications. The robust and extremity resistant nature of WS_2, and TMDCs in general, can be harnessed to develop high performing solar cells operating in extreme environments such as outer space. This material has the potential to be a strong competitor to existing solar cell modules in space photovoltaics. We have also simulated our solar models under space solar radiation (AM0 spectrum) to get a better understanding and insight into the performance of our device model for space photovoltaic applications.

3.2 Theory and Methods

3.2.1 Material Properties

The electronic and optical properties of monolayer and bulk WS_2 were taken from Chapter 2. We have used the electronic band structure, bandgap, absorption coefficient, conduction band effective density of states N_C, valence band effective density of states N_V and relative dielectric constant from the results presented in our previous work. The electron affinity of bulk WS_2 was taken to be 4.5 eV [110]. It has been seen that when a TMDC monolayer is aligned with bulk material, the conduction band of the monolayer is below the conduction band of the bulk material with a band offset of around 0.2 eV in the conduction band [111]; therefore, the electron affinity of monolayer WS_2 was taken to be 4.7 eV in our simulations. It has been observed in recent work that the electron

mobility of WS_2 can be as high as 234 $cm^2V^{-1}s^{-1}$ [112], [113]. Experimentally prepared WS_2 can exhibit some non-idealities, such as sulfur vacancies, which can lead to various electronic defects and non-ideal behavior. We have compensated for such issues by taking conservative values for the carrier lifetimes and mobilities, which are drawn directly from experiments. The electron mobility of WS_2 was taken to be 200 $cm^2V^{-1}s^{-1}$, while the hole mobility was found to be between one-third and one-fourth of the electron mobility [104], which can be as low as 50 $cm^2V^{-1}s^{-1}$. Because of this relatively low hole mobility, we have utilized a design that sidesteps hole minority carrier transport through the WS_2 layer, in favor of the comparatively higher electron mobility. The bandgap, electron affinity, relative dielectric constant, N_C and N_V of a-Si were taken from standard literature [114], [115]. The electron mobility was taken as 1 $cm^2V^{-1}s^{-1}$ and the hole mobility was taken as 0.003 $cm^2V^{-1}s^{-1}$ for a-Si [116].

To design an appropriate photovoltaic model, monolayer and bulk WS_2 were used together with amorphous silicon in p-n heterojunction model, similar to a silicon HIT structure. The electronic properties of monolayer WS_2, bulk WS_2 and a-Si which were used in the device simulations are summarized in Table 2.

Table 2. Electronic properties of monolayer WS_2, bulk WS_2 and a-Si used in device simulation.

	Monolayer WS_2	**Bulk WS_2**	**a-Si**
Bandgap (eV)	2.15 (direct)	1.29 (indirect)	1.7 (direct)
Electron Affinity (eV)	4.7	4.5	4
Relative Dielectric Constant	5.1	13.4	11.7
Conduction Band Effective Density of States N_C (cm^{-3})	$0.97*10^{19}$	$2.02*10^{19}$	$2.82*10^{19}$
Valence Band Effective Density of States N_V (cm^{-3})	$1.34*10^{19}$	$2.48*10^{19}$	$2.65*10^{19}$
Electron Mobility (cm^2 $V^{-1}s^{-1}$)	200	200	1
Hole Mobility (cm^2 $V^{-1}s^{-1}$)	50	50	0.003

3.2.2 Solar Spectrum

We have used both the terrestrial and space solar irradiance as the incident radiation on our solar cell model. The primary device simulations which we have presented are based on the AM 1.5G spectrum, which is the terrestrial solar radiation on the surface of the Earth [117]. To further develop our model for applications in diverse environments, we have also carried out our device simulations for the AM0 spectrum, which is the space solar radiation [117]. The spectral irradiance for the AM1.5G and AM0 solar spectra are shown in Figure 13.

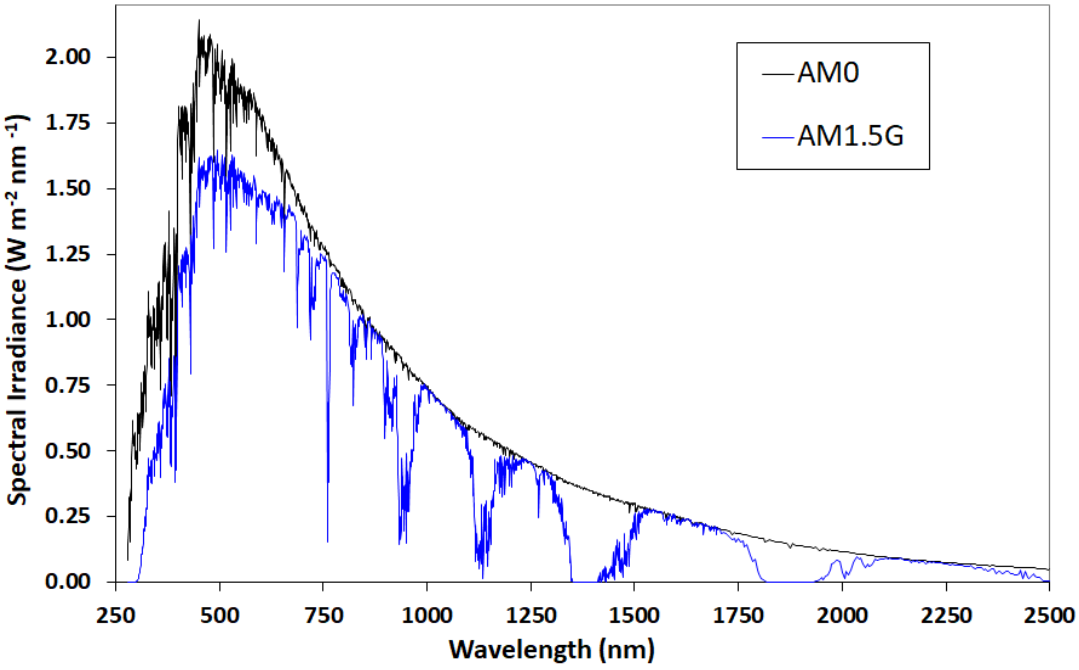

Figure 13. Terrestrial (AM1.5G) and Space (AM0) Solar Radiation [117].

The solar spectrum changes throughout the day and with location on Earth. Standard reference spectra are defined to enable the performance comparison of photovoltaic devices from different manufacturers and research laboratories in a convenient manner. The standard spectrum for space applications is referred to as AM0; it has an integrated power of 1366.1 W/m^2. For terrestrial applications, there are two defined standards in use. The AM1.5 Global spectrum is designed for flat plate modules and has an integrated power of 1000 W/m^2. The AM1.5 Direct (+circumsolar) spectrum is defined for solar concentrator work. It includes the direct beam from the sun plus the circumsolar component in a disk 2.5 degrees around the sun. The direct plus

circumsolar spectrum has an integrated power density of 900 W/m^2 [118]. For most photovoltaic measurements and performance monitoring, the AM1.5G spectrum is used as the standard incident solar radiation on the solar cells; this makes it easier and convenient to compare the power output and performance of different solar cells.

The air mass coefficient (AM) defines the direct optical path length through the Earth's atmosphere, expressed as a ratio relative to the path length vertically upwards. The air mass coefficient is used for characterizing the solar spectrum after solar radiation has traveled through the atmosphere. The air mass coefficient is defined as:

$$AM = \frac{1}{\cos(z)}$$

where z is the angle (in degrees) of the tilt of the sun from the vertical direction on the surface of the Earth. The standard AM1.5G spectrum is defined for a location where the sun is at angle of around 48-49° from the vertical.

3.2.3 Design of a Photovoltaic Device

A solar cell model was designed with the major concept being a p-n junction device which would be able to generate electron-hole pairs from incoming photons in the incident solar radiation [119]–[121]. The output current from the solar cell and the voltage across the terminals were calculated using the Drift-Diffusion model [104], [122]. The tool ADEPT (A Device Emulation Program and Tool) was used on nanoHUB to simulate our structure models [123]. The simulation results obtained from ADEPT have been shown to match closely with measurements of the current-voltage relationships in light and dark conditions, as well as the external quantum efficiency, of experimentally fabricated solar cells [124]–[126].

The quantum efficiency of a solar cell is the ratio of the number of carriers generated to the number of photons of a given energy/wavelength incident on the solar cell. It can be regarded as the collection probability of photons from the generation profile of a single wavelength, integrated over the device thickness and normalized to the incident number of photons. The external quantum efficiency (EQE) of a solar cell accounts for optical losses due to transmission and reflection [127].

The short-circuit current (I_{SC}) is the current through the solar cell when the voltage across the solar cell is zero (short circuit condition). The short-circuit current arises from the generation and collection of light-generated carriers. For an ideal solar cell with low or moderate resistive losses, the short-circuit current is the largest current which can be obtained from the solar cell. The short-circuit current depends on several factors; the primary factor is the area of the solar cell. It is more common to mention the short-circuit current density (Jsc) to remove the dependence on the area of the solar cell. The J_{SC} is directly dependent on the light intensity, or the number of photons, in the incident solar spectrum. For most terrestrial solar cells, the standard AM1.5G solar spectrum is used as reference. The J_{SC} also depends on the optical properties (absorption and reflection) and the collection probability of the solar cell, which is reflected in the EQE [128].

$$J_{SC} = \int \frac{q\lambda}{hc} EQE(\lambda) S(\lambda) d\lambda$$

where,

EQE(λ) – external quantum efficiency of photons with wavelength λ

S(λ) – intensity of photons of a particular wavelength λ in the solar spectrum of a given air mass

λ – wavelength of light

q – elementary charge

h – Planck's constant

c – speed of light

The open-circuit voltage (V_{OC}) of a solar cell is the maximum voltage available at zero current [129]. The open-circuit voltage corresponds to the amount of forward bias on the solar cell due to the bias of the solar cell junction with the light-generated current.

$$V_{OC} = \frac{nkT}{q} \ln\left(\frac{I_L}{I_0} + 1\right)$$

where,

I_L – light generated current

I_0 – dark saturation current

n – semiconductor ideality factor (typically 1)

k – Boltzmann constant

T – temperature

q – elementary charge

The V_{OC} can also be determined from the carrier concentration:

$$V_{OC} = \frac{kT}{q} \ln\left[\frac{(N_A + \Delta n)\Delta n}{n_i^2}\right]$$

where,

N_A – doping concentration

Δn – excess carrier concentration

n_i – intrinsic carrier concentration

The efficiency of a solar cell is the fraction of incident power in the solar spectrum which is converted to electricity. It is the most commonly used parameter to compare the performance of different solar cells. Efficiency is defined as the ratio of energy output from the solar cell to input energy from the sun.

ADEPT is a detailed numerical device simulation code developed at Purdue University. The semiconductor current equations, Poisson's equation, and the hole and electron continuity equations (assuming drift-diffusion transport), are solved numerically in 1D, subject to appropriate boundary conditions (an ideal Ohmic contact in our case). The electronic and optical properties of each material, together with the operating conditions and device parameters, are defined in the input files of the ADEPT simulations.

The complete drift-diffusion model is based on the following set of equations in 1D:

Current equations

$$J_n = qn(x)\mu_n E(x) + qD_n\frac{dn}{dx} \qquad (1)$$

$$J_p = qp(x)\mu_p E(x) - qD_p\frac{dp}{dx} \qquad (2)$$

Continuity equations

$$\frac{\partial n}{\partial t} = \frac{1}{q}\nabla . J_N - r_N + g_N \qquad (3)$$

$$\frac{\partial p}{\partial t} = -\frac{1}{q}\nabla . J_p - r_P + g_P \qquad (4)$$

Poisson's equation

$$\nabla . D = q\ (p - n + N_D^+ - N_A^-) \qquad (5)$$

The devices were primarily simulated using the AM 1.5G spectrum [117] as the incident solar radiation input for our model to obtain the optimum structure with best performance. For some of our simulations, we have assumed a perfectly reflecting back surface optical reflector in our system, so that all unabsorbed incident photons are reflected back into the absorbing layers. We have studied both cases of no back surface optical reflection and full back surface optical reflection for our device models. A temperature of 300K was assumed for all simulations.

We have developed three solar cell models to explore and study the photovoltaic properties of WS_2 and obtain the device with the best performance. We have investigated a 3-layer device for our photovoltaic model where the top layer is a thin highly-doped layer (n-type), the middle layer is a thick intrinsic or light-doped layer (p-type), and the bottom layer is a thin highly-doped layer (p-type). All of our solar cell models have a 3-layer n^+-p-p^+ device architecture, similar to a silicon HIT solar cell structure. We have developed and studied the following solar cell device models using WS_2 to investigate its properties and performance in photovoltaic applications:

1. **Model A**: Bulk WS_2 – Bulk WS_2 – Bulk WS_2 [Figure 14(A)]
2. **Model B**: Monolayer WS_2 – Bulk WS_2 – Bulk WS_2 [Figure 15(A)]
3. **Model C**: Monolayer WS_2 – Bulk WS_2 – Amorphous silicon [Figure 16(A)]

We have used model A as our baseline device and explored mechanisms to improve operating performance, leading to the development of models B and C which have significantly higher device efficiencies. We have explored and studied models B and C further to understand their behavior and performance in a different operating environment. Following on from our studies under terrestrial solar radiation, we have investigated the performance of models B and C under the space solar radiation (AM0 spectrum) to explore potential implementations our WS_2-based solar cell models in space photovoltaic applications.

We have taken measures and precautions in our simulations to present our results which are consistent with experimentally fabricable and measurable devices. We have accounted for non-

idealities in our materials and device architecture wherever possible. The goal of this project was to present a solar cell model which would give the predicted performance and features when tested and characterized experimentally. Thus, we refrained from incorporating near-ideal device parameters and operating conditions.

It is evident that significant carrier recombination will occur in our proposed structures in experiments, which can be accounted for by using conservative values of the carrier lifetimes in our simulations. Based on prior experimental results in related TMDCs, the electron and hole lifetimes for all the layers with moderate to high doping were taken as 10 ns, while for intrinsically-doped or lightly-doped bulk WS_2 the lifetimes were taken as 100 ns. For the carrier lifetimes, both radiative and non-radiative recombination have been considered. For 2D semiconductor TMDCs like WS_2, the non-radiative electron and hole lifetimes are much higher than radiative lifetimes, which is consistent with their direct bandgaps; thus, it is the radiative lifetime that is dominant in the effective carrier lifetime [130]. The lifetimes used in our simulations account for the radiative recombination of electrons and holes, which is the dominant recombination process. The carrier lifetimes used in our simulations are lower for heavily doped layers than lightly doped layers, since there is a reduction in carrier mobility with increased doping which can lead to higher recombination rates [131].

We have reviewed the literature on high levels of doping in silicon and WS_2 to determine the maximum activated doping levels at room temperature. Several researchers have reported doping levels as high as 10^{20} cm^{-3} in silicon [132]–[134]. As for WS_2, there has not been nearly as much work regarding its properties, since it is a relatively new material; but it has a lot of properties similar to molybdenum disulfide (MoS_2) such as band structure, bandgap, absorption profile, physical properties, etc., as they belong to the same family of transition-metal disulfides. Doping levels as high as 10^{20} cm^{-3} have been experimentally demonstrated in MoS_2 [135]. This result is also physically plausible, as the density of sulfur atoms in a transition-metal disulfide is around ~ 10^{22} cm^{-3}. In fact, it is possible to fabricate a doped MoS_2 structure where as much as 10% of the sulfur atoms are replaced by dopant atoms [37], which would correspond to a doping level of 10^{21} cm^{-3}. Since WS_2 and MoS_2 have similar physical, chemical and electronic properties, this provides evidence that it is possible to have doping levels as high as 10^{20} cm^{-3} in WS_2. Nonetheless, out of an abundance of caution, we have used conservative values for the doping levels, with the full

understanding that experimental verification is ultimately needed for any assumed level of doping. In this work, we have ensured that the doping in any layer does not exceed the values of N_C or N_V (effective density of states in conduction and valence bands, respectively) to avoid a scenario where a significant number of dopant atoms are inactivated. With this limitation taken into consideration and incorporation of fully activated donors and acceptors, there will not be any issues with incomplete ionization. If there is any loss of majority carriers from inactivated dopants, the loss can be compensated by injecting a higher concentration of dopants, within limits.

We have assumed Ohmic contacts in our simulations. The electron affinities of monolayer WS_2, bulk WS_2 and a-Si are 4.7, 4.5 and 4 eV respectively. The metals of choice should have appropriate work functions to provide a favorable Ohmic contact, with a zero or negative Schottky barrier height. For an n-type semiconductor, the work function of the metal must be close to or smaller than the electron affinity of the semiconductor. For a p-type semiconductor, the work function of the metal must be close to or larger than the sum of the electron affinity and the bandgap energy. For n-type monolayer WS_2 and bulk WS_2, we can have aluminum, chromium or silver as the metal contacts, since they have work functions close to or lower than 4.5 eV. For p-type bulk WS_2, we can potentially use platinum, palladium, tungsten, gold, nickel or cobalt as the metal contacts, since their work functions are above 5 eV. As for p-type a-Si, platinum [136] and titanium/palladium [137] have been experimentally demonstrated to provide Ohmic contacts; there is also potential to use lower cost metals with slightly lower work functions, such as tungsten and cobalt. We have given some examples of metals which can be used in our device models in experimental studies, but the list is not exhaustive; several commonly-used metals with an appropriate work function can be used.

3.3 Results and Discussion

3.3.1 Device Modeling under AM1.5G Solar Spectrum

The initial device model which we have considered is an n^+-p-p^+ homojunction structure made from bulk WS_2 (Model A). The device was then modified by replacing the top bulk WS_2 layer with monolayer WS_2 to obtain a heterojunction device (Model B) with improved performance, since monolayer WS_2 has a higher direct bandgap and better absorption than bulk WS_2. The final

device was designed by replacing the bottom bulk WS_2 layer with a-Si (Model C) to obtain a structure similar to HIT solar cells [109]. Incorporating a-Si in the device improves the performance by creating monotonically increasing conduction and valence bands, which improve carrier separation and electron and hole collection. Monolayer WS_2 and a-Si function as carrier selective contacts, where the electrons are collected at the monolayer WS_2 end and the holes are collected at the a-Si end.

Although one could compare the changes of individual parameters such as layer thickness or material parameters, each individual comparison is not always very informative by itself, because the carrier transport and optical absorption interact in a nonlinear fashion with respect to certain parameters – for example, changing the electron affinity can exponentially decrease electron current. Therefore, we have chosen to optimize three distinctive photovoltaic structures (A, B, C) representing distinctive material sets with suitable device architectures.

A three-layer junction device was designed to operate as a solar cell. The initial structure (Model A) was an n^+-p-p^+ device designed using only bulk WS_2 for all the three layers. The top layer was a thin layer of highly-doped n-type WS_2; the middle layer was a relatively thick layer of lightly-doped (almost intrinsic) p-type WS_2; and the bottom layer was a thin layer of highly-doped p-type WS_2 [Figure 14(A)]. We then optimized the layer thicknesses and doping for highest efficiency. The optimal device structure of model A is summarized in Table 3.

The device model was simulated for both cases of with and without back surface optical reflector. The open circuit voltage (V_{OC}) for the optimum case was obtained to be 0.76 V and the short circuit current density (J_{SC}) was 24.1 mA/cm^2; the efficiency of the solar cell was 15.2%. The significant parameters and features of the solar cell such as short circuit current density (J_{SC}), open circuit voltage (V_{OC}), maximum power voltage (V_{MP}), maximum power current density (J_{MP}), fill factor (FF) and efficiency were recorded for both the cases of with and without back surface reflection (Table 4).

The band structure, current-voltage (I-V) relationship and external quantum efficiency (EQE) plots for the case of full back surface optical reflection are shown in Figure 14(B-D). The conduction and valence bands are monotonically increasing, which favor carrier collection. It can be seen from the plot of the EQE that there is a significant improvement in carrier generation for

wavelengths greater than 0.6 µm, which corresponds to absorption in the space-charge region. The current-voltage relationship shows excellent rectification, which is consistent with a low series and high shunt resistance.

Table 3. Summary of Model A device structure.

	Top Layer	**Middle Layer**	**Bottom Layer**
Material	Bulk WS_2	Bulk WS_2	Bulk WS_2
Bandgap (eV)	1.29	1.29	1.29
Doping Type	N	P	P
Doping concentration (cm^{-3})	$2*10^{19}$	10^{13}	$2.4*10^{19}$
Thickness (nm)	40	400	40

The open circuit voltage (V_{OC}) obtained is similar to that of silicon solar cells [138]; the short circuit current density (J_{SC}) is reasonable for a solar cell, although well below the theoretical limit for the 1.29 eV bandgap of WS_2. While the overall efficiency is not very high, it is promising as a starting point to systematically improve our device. It can be seen that using a perfect back surface optical reflector increases J_{SC} by a significant amount, and improves the performance and efficiency of the device.

Table 4. Performance parameters of Model A device.

	No Back Surface Reflection	**Full Back Surface Reflection**
Open Circuit Voltage V_{OC} (V)	0.76	0.76
Short Circuit Current Density J_{SC} (mA/cm^2)	22.3	24.1
Maximum Power Voltage V_{MP} (V)	0.66	0.66
Maximum Power Current Density J_{MP} (mA/cm^2)	21.1	22.8
Fill Factor FF	0.82	0.82
Efficiency (%)	14	15.2

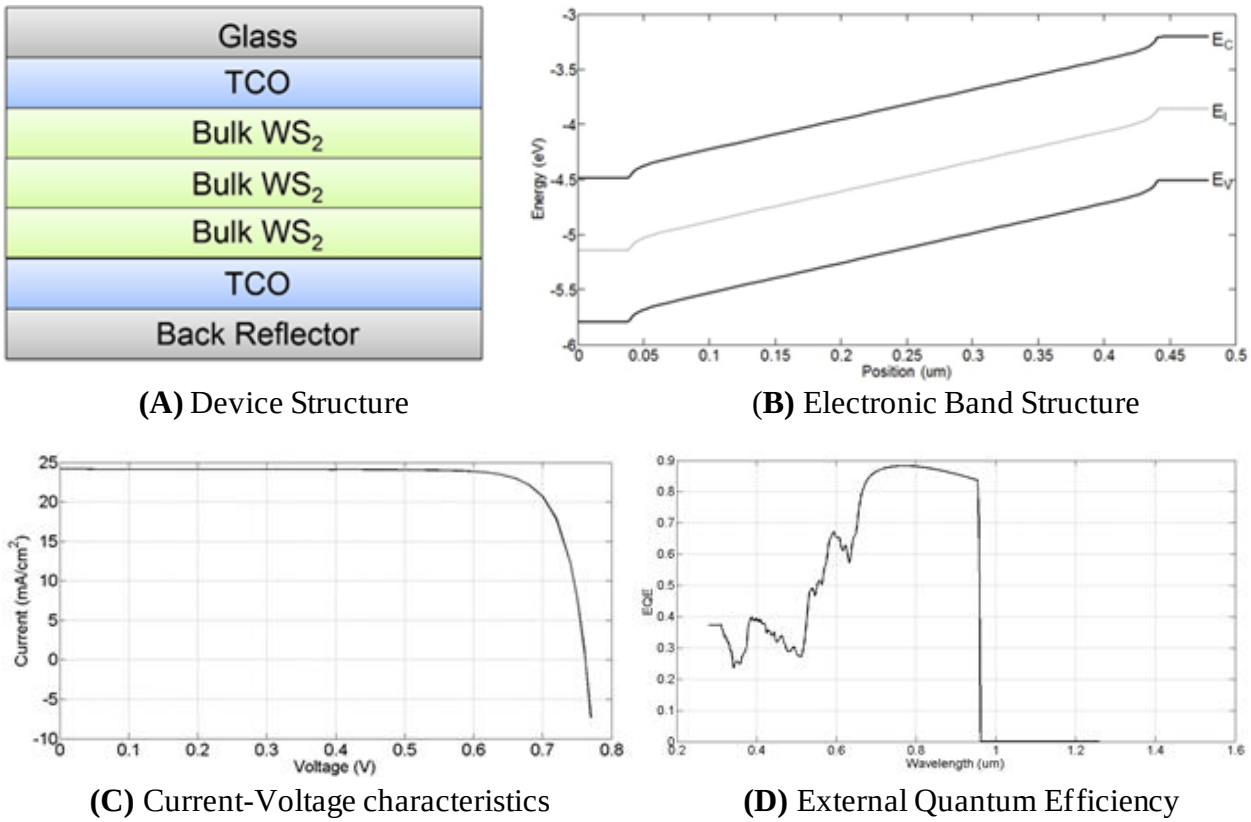

(A) Device Structure (**B)** Electronic Band Structure

(C) Current-Voltage characteristics **(D)** External Quantum Efficiency

Figure 14. Device structure and performance parameters of Model A: (A) Device structure; (B) Band structure; (C) I-V plot; and (D) EQE.

This initial device was then modified by replacing the top bulk WS_2 layer with monolayer WS_2 of same doping type [Figure 15(A)] to obtain a heterojunction device structure (Model B). Monolayer WS_2 has a direct bandgap and provides a higher bandgap window layer for light absorption at the n^+-p junction. This structure was then re-optimized for the highest efficiency with respect to all the layers' doping and thickness, subject to a monolayer maximum thickness of 10 nm and a maximal doping of $0.95*10^{19}$ cm^{-3}. The optimal device structure of model B is summarized in Table 5.

Model B device was simulated for both cases with and without back surface optical reflection, and the performance parameters were recorded (Table 6). The band structure, current-voltage (I-V) relationship and EQE plots for the case of full back surface optical reflection are shown in Figure 15(B-D). The conduction and valence bands are also monotonically increasing in this case, which favor carrier collection. There is an abrupt drop in the bands on the monolayer

WS_2 side which helps in improved electron collection. It can be seen from the plot of the EQE that there is a slight improvement in carrier collection for wavelengths between 0.6 µm and the band edge. The introduction of a non-zero slope near the front of the cell also significantly improves carrier collection for wavelengths below 0.6 µm. For the optimized device structure of model B, the open circuit voltage (V_{OC}) was 0.77 V and the short circuit current density (J_{SC}) was 32.6 mA/cm^2; the efficiency of the solar cell was 20.5% with a perfect back surface optical reflector.

Table 5. Summary of Model B device structure.

	Top Layer	**Middle Layer**	**Bottom Layer**
Material	Monolayer WS_2	Bulk WS_2	Bulk WS_2
Bandgap (eV)	2.15	1.29	1.29
Doping Type	N	P	P
Doping concentration (cm^{-3})	$0.95*10^{19}$	10^{13}	$2.4*10^{19}$
Thickness (nm)	10	2000	100

Table 6. Performance parameters of Model B device.

	No Back Surface Reflection	**Full Back Surface Reflection**
Open Circuit Voltage V_{OC} (V)	0.77	0.77
Short Circuit Current Density J_{SC} (mA/cm^2)	32.6	32.6
Maximum Power Voltage V_{MP} (V)	0.67	0.67
Maximum Power Current Density J_{MP} (mA/cm^2)	30.4	30.4
Fill Factor FF	0.81	0.81
Efficiency (%)	20.5	20.5

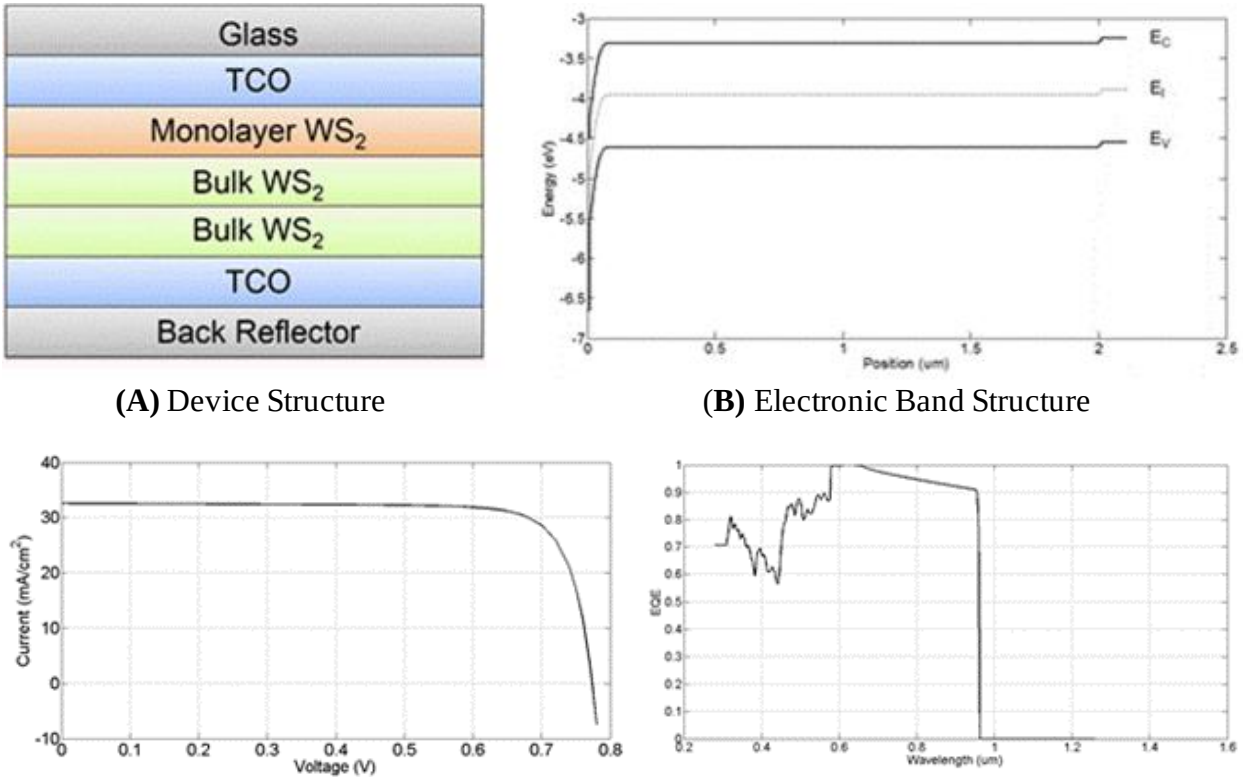

(A) Device Structure (**B)** Electronic Band Structure

(C) Current-Voltage characteristics **(D)** External Quantum Efficiency

Figure 15. Device structure and performance parameters of Model B: (A) Device structure; (B) Band structure; (C) I-V plot; and (D) EQE.

Compared to the homojunction device model A discussed previously, the open circuit voltage (V_{OC}) improves by about 2%; the short circuit current density (J_{SC}) increases greatly by about 35%, and is now comparable to that of silicon solar cells. Overall, then, the efficiency of the device model B is about 35% higher than the device model A, which is quite high and comparable to commercial solar cells. The results are very promising, but it is possible to improve the device even further, since there are still losses due to recombination of carriers, unsuitable band structure, incomplete absorption, inefficient carrier collection, etc. For instance, the band structure is still non-ideal which penalizes our open circuit voltage by at least 50 mV, and also degrades the short circuit current by at least 1.0 mA/cm^2. Thus, additional modifications were investigated to help us approach the Shockley-Queisser limit as closely as possible.

The device model B was further modified to improve performance by replacing the bottom bulk WS_2 layer with a-Si of same doping type [Figure 16(A)] to obtain a structure similar to HIT

solar cells (Model C). Since a-Si has a lower electron affinity than WS_2, it was used to provide monotonically increasing conduction and valence energy bands so that electrons and holes can easily move towards the opposite contacts and there are no areas in the structure where there could be accumulation and consequent recombination of the carriers. a-Si was also used in the structure to prevent recombination of carriers at the back surface contact. This structure was re-optimized with respect to the layers' thicknesses and doping levels. The final device structure of model C which gave highest efficiency is summarized in Table 7.

Table 7. Summary of Model C device structure.

	Top Layer	**Middle Layer**	**Bottom Layer**
Material	Monolayer WS_2	Bulk WS_2	a-Si
Bandgap (eV)	2.15	1.29	1.7
Doping Type	N	P	P
Doping concentration (cm^{-3})	$0.95*10^{19}$	$0.5*10^{18}$	$2.65*10^{19}$
Thickness (nm)	10	800	10

Model C device was simulated for both cases with and without back surface optical reflection, and the performance parameters were recorded (Table 8). The band structure, current-voltage (I-V) relationship and EQE plots for the case of full back surface optical reflection are shown in Figure 16(B-D). The conduction and valence bands are also monotonically increasing in this case, which provide nearly ideal carrier collection. Also, the abrupt drop in the conduction band on the monolayer WS_2 side which facilitates electron collection, while the abrupt jump in the valence band on the a-Si side improves hole collection. The plot of the EQE is similar to the previous case, with a small improvement near the band edge from a deeper space charge region, resulting in a slightly higher J_{SC}. There is also an improvement in the V_{OC} realized by a back surface field plus an improved band structure achieved through the introduction of a-Si.

Table 8. Performance parameters of Model C device.

	No Back Surface Reflection	Full Back Surface Reflection
Open Circuit Voltage V_{OC} (V)	0.84	0.84
Short Circuit Current Density J_{SC} (mA/cm^2)	32.8	33.5
Maximum Power Voltage V_{MP} (V)	0.75	0.75
Maximum Power Current Density J_{MP} (mA/cm^2)	30.5	31.2
Fill Factor FF	0.82	0.82
Efficiency (%)	22.7	23.3

(A) Device Structure

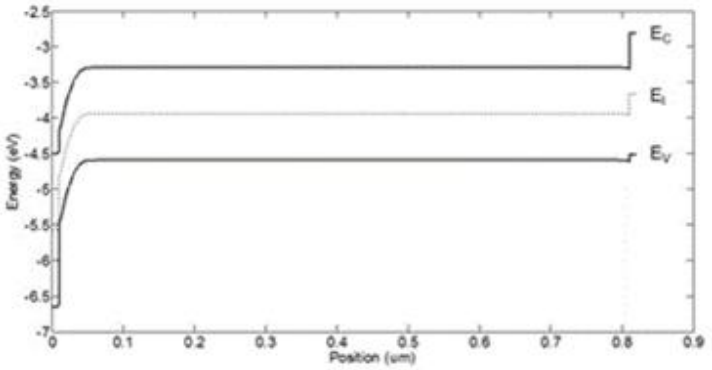

(**B)** Electronic Band Structure

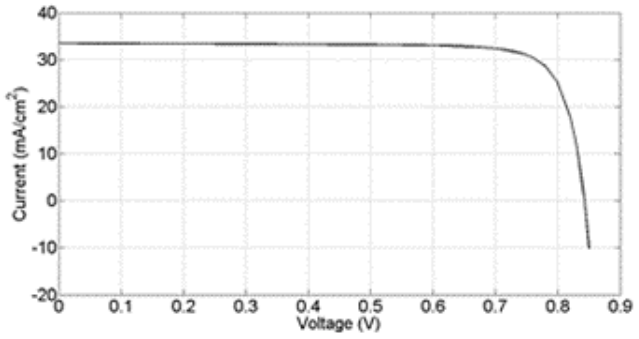

(C) Current-Voltage characteristics

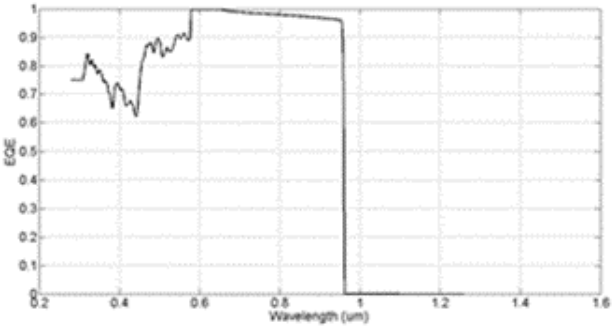

(D) External Quantum Efficiency

Figure 16. Device structure and performance parameters of Model C: (A) Device structure; (B) Band structure; (C) I-V plot; and (D) EQE.

The performance of our final device model C is found to be much improved after the incorporation of a-Si. The open circuit voltage (V_{OC}) for the best case is 0.84 V and the short circuit current density (J_{SC}) is 33.5 mA/cm^2; the efficiency of the solar cell is 23.3%. The open circuit voltage (V_{OC}) for model C is much better than the previous structures (models A and B), and has increased significantly (by about 10% relative, compared to the initial homojunction device model A); the short circuit current density (J_{SC}) has also increased substantially (by about 38% relative, compared to the initial device model A). Overall, the efficiency of the solar cell model C has improved by about 53% relative versus the homojunction device model A; it is quite high, and comparable to many high-efficiency single junction solar cells [115]. The presence of a perfect back surface optical reflector helps slightly in improving J_{SC}, and thus, the V_{OC}, as well as the overall efficiency of the solar cell. These results create new possibilities for the fabrication and use of ultra-thin 2D high-efficiency solar cells using a new material which has the advantages of ultra-low weight per unit of power production, mechanical flexibility, as well as earth abundance, compared to several commonly-used photovoltaic materials.

3.3.2 Device Modeling under AM0 Solar Spectrum

Using the optimized device model from our results with the AM1.5G terrestrial solar radiation, further simulations were carried out with the AM0 space solar spectrum to investigate the performance and features of our WS_2-based solar cell model in potential space photovoltaic applications. The temperature of most satellite orbits is between 40-70°C [14]; so, we have used two temperatures of 313K and 343K for our device model simulations under the space solar radiation. From our results presented in section 3.3.1, it can be seen that the best performing device structure is model C [Figure 16(A)]. So, we have chosen this device model as the starting point for our simulations under the AM0 spectrum.

We have used the same layers as presented in model C in section 3.3.1. It is a three-layer n^+-p-p^+ junction device designed to operate as a solar cell. The top layer is a thin layer of highly-doped n-type monolayer WS_2; the middle layer is a relatively thick layer of lightly-doped p-type bulk WS_2; and the bottom layer is a thin layer of highly-doped p-type a-Si, as shown in Figure 16(A). Some modifications were made to the thickness of the constituent layers to better understand the performance of our model with various thicknesses in a space environment. The

thicknesses of the top and bottom highly-doped layers were kept unchanged at 10 nm each. The thickness of the lightly-doped middle layer was initially taken as 980 nm, so the total thickness of the device was 1 µm. The initial structure model is described in Table 9.

Table 9. Summary of modified Model C device structure for space applications.

	Top Layer	**Middle Layer**	**Bottom Layer**
Material	Monolayer WS_2	Bulk WS_2	a-Si
Bandgap (eV)	2.15	1.29	1.7
Doping Type	N	P	P
Doping concentration (cm^{-3})	$0.95*10^{19}$	$5*10^{17}$	$2.65*10^{19}$
Thickness (nm)	10	980	10

It is beneficial to design devices with thickness much less than 1 µm for space applications, since thicker devices can be significantly damaged by high energy radiation and cosmic rays in the space environment without additional radiation shielding mechanisms. Most solar cells used in space photovoltaic applications with high radiation concentrations typically have thicknesses of around 100-500 nm of active layers to minimize radiation damage. So, we have decided to limit our device thickness to 1 µm in order to present realistic models and maintain consistency with experimentally feasible device architectures.

We have investigated our modified device model C with the total device thickness ranging from 100 nm to 1 µm. Each model was simulated under the AM0 spectrum for temperatures of 313K and 343K. The significant parameters and features of the solar cell model such as short circuit current density (J_{SC}), open circuit voltage (V_{OC}) and efficiency were recorded for both the temperatures 313K (Table 10) and 343K (Table 11). All the device simulations were carried out using the tool ADEPT on nanoHUB.

Table 10. Performance parameters of modified Model C device at 313K.

Thickness (nm)	V_{OC} (V)	J_{SC} (mA/cm^2)	Efficiency (%)
100	0.87	25.6	12.5
200	0.86	31.8	15.8
400	0.85	36.2	18.1
600	0.84	38.3	19.1
800	0.84	39.9	19.9
1000	0.83	41.1	20.5

Table 11. Performance parameters of modified Model C device at 343K.

Thickness (nm)	V_{OC} (V)	J_{SC} (mA/cm^2)	Efficiency (%)
100	0.82	25.6	11.3
200	0.81	31.8	14.3
400	0.80	36.2	16.4
600	0.79	38.3	17.3
800	0.79	39.9	18.1
1000	0.78	41.1	18.6

We can see that our device model gives an efficiency of 20% for the 1 um thick device at a temperature of 313K. The efficiency drops to 18.6% for a temperature of 343K; this is an expected drop in the efficiency since there is a reduction of the V_{OC} due to an increase in the temperature. The performance of our device model at around 20% efficiency is comparable to existing space photovoltaic technology [15]. But our proposed solar cell model gives us only an insight and not a conclusive picture of the applicability of our device in space photovoltaics. For space applications, it is most beneficial to have the active layer thickness around 100-200 nm to minimize radiation damage without using additional radiation shielding structures. We can see that for a device thickness of 200 nm, the efficiency of our model is around 14.3-15.8% over the temperature range of satellite orbits (313-343K). This is much lower than the efficiency of existing space photovoltaic systems currently in use. Therefore, additional modifications and

improvements to our photovoltaic model are required to propose a realistic and experimentally viable device structure which can be competitive and comparable to existing space solar cells.

3.4 Outlook and Conclusion

In this work, we have developed several solar cell models to demonstrate photovoltaic properties and applications of a WS_2-based solar cell design. To compensate for expected fabrication impurities and crystal defects, conservative values for parameters such as carrier mobilities and lifetimes were utilized in our device simulations. Initially, we developed a baseline solar cell design using bulk WS_2 gives reasonable performance with an optimal efficiency of around 14%. After making some modifications, such as introducing monolayer WS_2 and a-Si, which improve the band structure and optical performance, the overall efficiency of the optimal solar cell model increased significantly to over 23%, which is comparable to the performance of many commercial single-junction solar cells. These results show that 2D monolayers of WS_2 have very favorable electronic and optical properties for use in photovoltaics, along with the natural advantages of light weight, flexibility, and earth abundance of most TMDCs.

One key challenge is to obtain high quality a-Si/WS_2 interfaces. It is assumed in this work that crystalline WS_2 is grown on a-Si to best preserve the electronic and chemical properties of the individual components, and to allow efficient carrier transport across the interface [139]. Nonetheless, WS_2 warrants further investigation, since there are several approaches that could lead to further improvement of performance of our device. For instance, bilayer WS_2 can be used to replace bulk WS_2, since it has a higher bandgap than the bulk material, but with the same direct transition energy, which can lead to a higher V_{OC} and comparable J_{SC}. Second, applying a horizontal strain or a vertical compressive force to WS_2 can tune its band structure and bandgap, which can pave the way for a spectrally-adaptable photovoltaic cell; this could potentially also be part of a multi-junction array. Third, the optical reflection implied by the non-ideal EQE of the device can be investigated using various light trapping approaches, such as plasmonics. This approach has yielded methods for guiding and localizing light at the nanoscale in previous work, allowing for greatly improved absorption in photovoltaic devices [140]. Finally, since we are working with ultra-thin layers, it might be beneficial and more accurate to go beyond the semi-

classical drift-diffusion model, and look at quantum effects such as ballistic transport to better understand electron transport and photon absorption at the atomic level.

As far as experimental validation of the optimized design goes, the full device structure should have a back surface optical reflector, such as a screen-printed metal with an appropriate work function as the first layer from the bottom [141]. On top of that, there should be a layer of TCO (Transparent Conducting Oxide), such as ITO (Indium Tin Oxide), of appropriate thickness. The TCO layer is used to collect the free carriers generated in our solar cell. On top of the TCO would be our three-layer structure, which would be covered by another layer of TCO to collect the generated carriers and allow transmission of incoming solar radiation with minimal surface optical reflection. A layer of glass can be placed as the topmost layer to protect the inner layers from environmental impurities and disturbances. The monolayer WS_2 layer needs to be prepared such that multiple layers can be stacked together with appropriate interlayer spacing which preserves the electronic properties of monolayer WS_2 [78]. Since WS_2 has properties similar to MoS_2, similar dopants can be used in our device, such as alkali metals (Na, K, etc.) in place of tungsten atom (W) as p-type dopants and halogen atoms (Cl, F, etc.) in place of sulfur atoms (S) as n-type dopants [142]. In conclusion, there is a great deal of work yet to be performed on this emerging 2D materials system, but the work to date presented in this paper provide specific predictions based on first principles to help guide further theoretical and experimental investigations.

We have also demonstrated our WS_2-based photovoltaic model for applications under space solar radiation. Our solar cell design shows that it is possible to obtain efficiencies above 20% with the space solar spectrum, but a major issue encountered here is the total thickness of the active layers in our device and possible radiation-induced degradation. The simulation results are still a preliminary insight as much work is needed to be done in order to propose an experimentally feasible solar cell model for space photovoltaic applications. It is most beneficial to develop an ultra-thin device of around a few hundred nanometers or less, while incorporating additional features such as light trapping structures and anti-reflection coating layers to get a higher device performance. This would have the potential to make our solar cell model proposals competitive with current technology; it would also strengthen our predicted results and make them comparable with existing space photovoltaic systems.

4. LIGHT TRAPPING FOR PERFORMANCE ENHANCEMENT OF TMDC-BASED PHOTOVOLTAIC SYSTEMS IN SPACE APPLICATIONS

4.1 Background

Photovoltaics is the primary power source in outer space for Earth orbiting satellites and many space exploratory missions, since the radiation originating from the sun can be received in high concentrations in outer space. The space environment is heavily characterized by a harsh radiation environment consisting of high energy particles and cosmic rays; therefore, it is vitally important to develop solar cell with semiconductor materials which have a high degree of radiation resistance and resilience in the space environment; this is essential to minimize degradation of the end-of-life performance of the solar cell [143]. Devices based on two-dimensional (2D) materials are characterized by their low size and weight, together with high resilience and reliability. This makes them advantageous and beneficial for implementation in high radiation environments. Transition Metal Di-Chalcogenides (TMDCs) have been demonstrated to exhibit resistance to radiation-induced damage, and are very good candidates for space photovoltaic applications [16].

As we have seen in Chapter 3, the photovoltaic model based on tungsten disulfide (WS_2) which gave the best performing solar cell in terrestrial conditions was Model C. This model was simulated under space solar radiation (AM0 spectrum). We demonstrated that Model C with total thickness of 1 um gave an efficiency above 20% for 313K and above 18% for 343K temperature. These efficiency values are comparable to high performing solar cells currently used in space photovoltaics. But the thickness of this model is too thick for space applications.

For space applications, it is most beneficial to have the total active layer thickness around a few hundred nanometers to minimize radiation damage without using additional radiation shielding structures [144]. Solar cells with thick active layers of magnitudes in the order of microns are prone to significant damage from the high energy radiation and particles in the space environment; while ultra-thin materials with sub-micron thicknesses are much more resistant to radiation damage with less degradation in their performances over extended periods of time [145], [146]. With consideration for possible structural damage of the material from radiation and corresponding degradation of performance, we have investigated our device models with thickness

limit of around 200 nm; we have explored our device structures with the total thickness of the active layers in the range 100-200 nm [147].

The photovoltaic model with thickness of 200 nm gave efficiencies around 14.3-15.8% over the temperature range of satellite orbits (313-343K). This is much lower than the efficiency of current space photovoltaic technology. It is necessary to incorporate additional modifications and improvements in our photovoltaic model to propose a realistic and experimentally viable device structure which can be competitive and comparable to existing space solar cells.

In this work, we have used the 200 nm thick Model C from Chapter 3 as the baseline solar cell device and introduced additional features in the structure so the efficiency can be higher than 20%. The major issue here is reduction of the absorption due to the ultra-thin device structure. We have incorporated a light trapping structure and an anti-reflection coating layer in our solar cell model which increase the absorption of the incident solar radiation, and lead to better performance of the device with higher current. These additional optical features lead to an enhancement of the J_{SC} resulting from the increased photon absorption. There is no significant effect on the V_{OC}. Our goal of increasing the device performance efficiency is through enhancement of the J_{SC}; we have not explored mechanisms of increasing the V_{OC} in this study.

We have used a 1D silver grating light trapping structure in our photovoltaic model to increase the optical path length of light inside the solar cell. In photovoltaics, light trapping is used to reduce the thickness of the solar cell without compromising the light absorption within the device. The optimal improvement of the device performance was obtained by optimizing the light trapping grating structure for maximum absorption enhancement. This resulted in an increase in the J_{SC} from the increased photon absorption in the device, without affecting the V_{OC}. The efficiencies of our solar cell increased to 18.5-20.4% over the temperature range 313-343K as a result of absorption enhancement from light trapping.

In addition to the optimized light trapping structure, we have also added an appropriate dielectric material layer in our photovoltaic model to function as an anti-reflection coating to further reduce the surface reflection from our solar cell and enhance the absorption. The dielectric layer material and thickness was optimized to minimize the surface reflection and exhibit the maximum improvement of the device performance. This led to further increase in the J_{SC} from the

additional photon absorption in the device, without affecting the V_{OC}. The efficiencies of our final solar cell model increased to 21.4-23.6% over the temperature range 313-343K because of the effect of the anti-reflection coating layer.

4.2 Theory and Methods

4.2.1 Photovoltaic Model

A solar cell model was designed with the major concept being a p-n junction device which would be able to generate electron-hole pairs from incoming photons in the incident solar radiation [119], [121]. We have investigated a 3-layer device architecture for our photovoltaic model where the top layer is a thin highly-doped layer (n-type), the middle layer is a relatively thick intrinsic or light-doped layer (p-type), and the bottom layer is a thin highly-doped layer (p-type), similar to a silicon HIT solar cell structure.

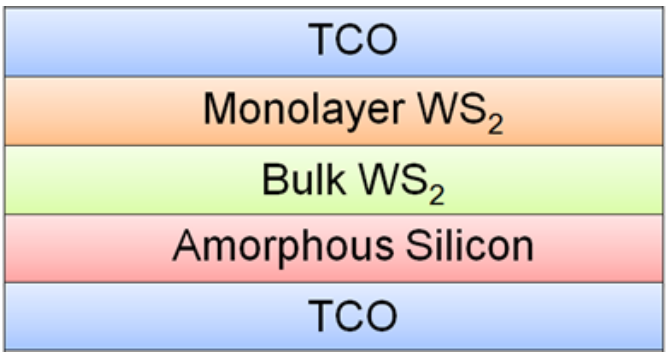

Figure 17. Initial photovoltaic model.

As we have seen in Chapter 3, the photovoltaic model which gave the best performing solar cell in terrestrial conditions was Model C as shown here in Figure 17. A three-layer n^+-p-p^+ junction device was designed to operate as a solar cell. The top layer was a thin layer of highly-doped n-type monolayer WS_2 stack; the middle layer was a relatively thick layer of lightly-doped (almost intrinsic) p-type bulk WS_2; and the bottom layer was a thin layer of highly-doped p-type WS_2 (Figure 17). The total thickness of our device structure was kept limited to 200 nm. The optimal device structure of our photovoltaic model is summarized in Table 12. We have named it Model C1 in this work.

Table 12. Summary of device structure Model C1.

	Top Layer	**Middle Layer**	**Bottom Layer**
Material	Monolayer WS_2	Bulk WS_2	a-Si
Bandgap (eV)	2.15	1.29	1.7
Doping Type	N	P	P
Doping concentration (cm^{-3})	$0.95*10^{19}$	$5*10^{17}$	$2.65*10^{19}$
Thickness (nm)	10	180	10

To account for the non-negligible carrier recombination in our materials, we have incorporated conservative values of the carrier lifetimes in our simulations. The electron and hole lifetimes for the top and bottom layers with moderate to high doping were taken as 10 ns, while for the lightly-doped bulk WS_2 middle layer the lifetimes were taken as 100 ns. We have also used conservative values for the doping levels, with the full understanding that experimental verification is ultimately needed for any assumed level of doping. In this work, we have ensured that the doping in any layer does not exceed the values of N_C or N_V (effective density of states in conduction and valence bands, respectively) to avoid a scenario where a significant number of dopant atoms are inactivated. With this limitation taken into consideration and incorporation of fully activated donors and acceptors, there will not be any issues with incomplete ionization.

We have assumed Ohmic contacts in our simulations. The electron affinities of monolayer WS_2, bulk WS_2 and a-Si are 4.7, 4.5 and 4 eV respectively. The metals of choice should have appropriate work functions to provide a favorable Ohmic contact, with a zero or negative Schottky barrier height. For an n-type semiconductor, the work function of the metal must be close to or smaller than the electron affinity of the semiconductor. For a p-type semiconductor, the work function of the metal must be close to or larger than the sum of the electron affinity and the bandgap energy. Carrier collection mechanisms have also been taken into account so that the free carriers can be efficiently collected from the device. We have proposed a layer of TCO (Transparent Conducting Oxide), such as ITO (Indium Tin Oxide), of appropriate thickness on both the top and bottom of our device to collect the free carriers generated in our solar cell.

Our device simulations were carried out with the AM0 space solar spectrum to investigate the performance and features of our WS_2-based solar cell model in potential space photovoltaic applications. The standard spectrum for space applications is referred to as AM0; it has an integrated power of 1366.1 W/m^2 [117]. The temperature of most satellite orbits is between 40-70°C [14]; so, we have used two temperatures of 313K and 343K for our device model simulations under the space solar radiation. The output current from the solar cell and the voltage across the terminals were calculated using the Drift-Diffusion model [104], [122]. The tool ADEPT (A Device Emulation Program and Tool) was used on nanoHUB to simulate our structure models [123]. Additional details about the material properties and simulation methodology have been discussed in Chapter 3. The device performance parameters and features of our initial solar cell model such as short circuit current density (J_{SC}), open circuit voltage (V_{OC}) and efficiency for both the temperatures 313K and 343K are summarized in Table 13.

Table 13. Performance parameters of Model C1 device.

Temperature	**313K**	**343K**
Open Circuit Voltage V_{OC} (V)	0.86	0.81
Short Circuit Current Density J_{SC} (mA/cm^2)	31.8	31.8
Efficiency (%)	15.8	14.3

We can see that for our solar cell model of thickness 200 nm, the device performance efficiency is around 14.3-15.8% over the temperature range of satellite orbits (313-343K). The expected drop in the efficiency arises from the reduction of the V_{OC} due to an increase in the temperature [148]. These efficiency values are much lower than the efficiency of space photovoltaic systems currently in use [15]. It is necessary for our model to have efficiencies above 20% to compete with existing space photovoltaic technology. Additional modifications and improvements were incorporated in our initial photovoltaic model to enhance the absorption of the incident solar radiation, and correspondingly increase the device performance efficiency. We have added a suitable light trapping structure and an appropriate anti-reflection coating layer to our

initial solar cell model to obtain improved device performance. The final device structure of our photovoltaic system is shown in Figure 18.

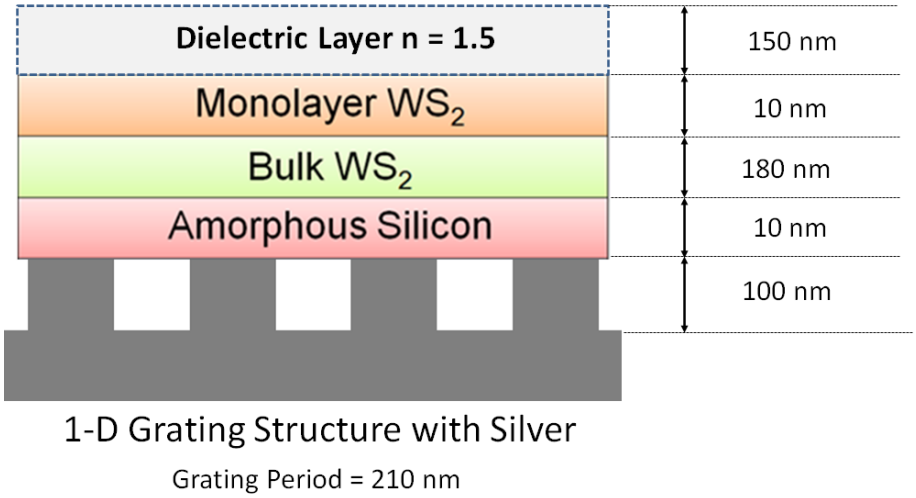

Figure 18. Photovoltaic model with light trapping and anti-reflection coating.

The initial solar cell model together with light trapping and anti-reflection coating was simulated using the tool S4 on nanoHUB [149]–[151] to obtain the absorptivity of our initial device and investigate the enhancement of absorption due to effect of adding the light trapping structure and the anti-reflection coating layer. S4 was used to obtain the improved optical performance and absorption profiles for our device model after incorporation of a suitable light trapping structure and an appropriate anti-reflection coating layer.

S4 stands for Stanford Stratified Structure Solver, a frequency domain code to solve the linear Maxwell's equations in layered periodic structures. Internally, it uses Rigorous Coupled Wave Analysis (RCWA, also called the Fourier Modal Method (FMM)) and the S-matrix algorithm [18]. This tool allows for fast and accurate prediction of optical propagation through layered periodic structures. S4 can compute transmission, reflection and absorption spectra of structures composed of periodic, patterned, planar layers.

The S-matrix method is well-known method used to solve transfer matrix problems for all grating models with upward- or downward-propagating and decaying waves as shown in Figure 19. The horizontal lines in Figure 19 represent real or numerical material interfaces. The letters **u**

and **d** represent a set of wave amplitudes as column vectors for upward- and downward-propagation waves in each layer, respectively.

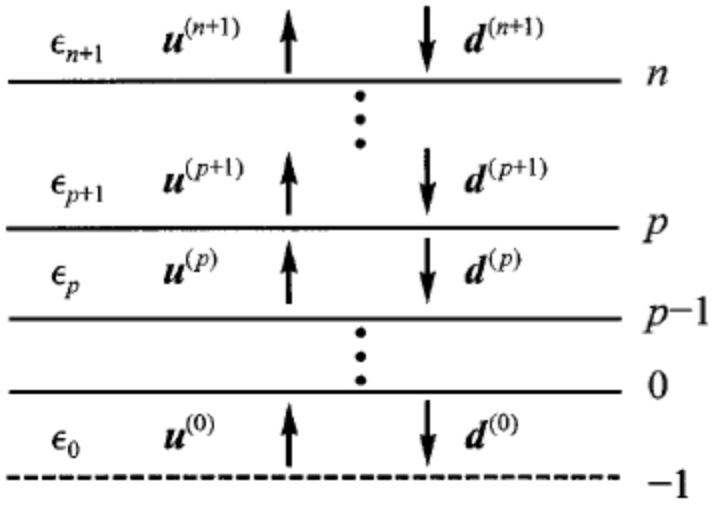

Figure 19. Abstract layered grating structure (adapted from [18]).

For an arbitrary layer p, where $0 \leq p \leq n$, there is a stack S matrix $\mathbf{S}^{(p)}$ satisfying the equation:

$$\begin{bmatrix} \mathbf{u}^{(p+1)} \\ \mathbf{d}^{(0)} \end{bmatrix} = \mathbf{S}^{(P)} \begin{bmatrix} \mathbf{u}^{(0)} \\ \mathbf{d}^{(P+1)} \end{bmatrix}$$

so that the waves in layer p+1 can be linked with medium 0. This equation can also be written in a two-by-two sub-matrix form:

$$\begin{bmatrix} \mathbf{u}^{(p+1)} \\ \mathbf{d}^{(0)} \end{bmatrix} = \begin{bmatrix} T_{uu}^{(p)} & R_{ud}^{(p)} \\ R_{du}^{(p)} & T_{dd}^{(p)} \end{bmatrix} \begin{bmatrix} \mathbf{u}^{(0)} \\ \mathbf{d}^{(P+1)} \end{bmatrix}$$

where T and R are the transmission and reflection matrices, respectively. Therefore, given the transmission of the upward incident wave amplitudes in medium 0 and the reflection of the downward incident wave amplitudes in layer p+1, the upward wave amplitudes in layer p+1 and the downward wave amplitudes in medium 0 can be calculated [18], [151].

Specifically, for the structure solved by S4, $\mathbf{u}^{(0)} = 0$, and $\mathbf{d}^{(n)}$, which is the incident planewave, is given. So $\mathbf{u}^{(n)}$, which is the total reflection, and $\mathbf{d}^{(0)}$, which is the total transmission, can be easily computed as:

$$\mathbf{u}^{(n)} = R_{ud}^{(n-1)} \mathbf{d}^{(n)}$$

and

$$\mathbf{d}^{(0)} = \mathrm{T}_{\mathrm{dd}}^{(\mathrm{n}-1)}\mathbf{d}^{(\mathrm{n})}$$

Then, the total absorption can be obtained by subtracting reflection and transmission from the total incident wave amplitude.

The constituent materials and layers in the periodic device structure, together with their corresponding real and imaginary dielectric functions, are defined in the input file. Each layer can be modified to incorporate specific patterns in their structure to simulate complex geometries. The multi-layer structure is simulated using periodicity to model optical performance of extended systems. The S4 tool on nanoHUB has been demonstrated to be capable of reproducing published experimental research results [151].

Initially, only our primitive solar cell Model C1 with the active layers was simulated to obtain the absorption profile. The dielectric functions of monolayer WS_2, bulk WS_2 and a-Si were obtained from our results in Chapter 2. A suitable light trapping structure was then added to the solar cell model, and this new system was simulated to investigate the enhancement of absorption and obtain the new improved absorption profile. This new device has been called Model C2. This new absorption profile was used in the device performance simulation in ADEPT to obtain the new enhanced device efficiency and performance parameters of Model C2. Finally, an appropriate anti-reflection coating layer was incorporated in our photovoltaic system in addition to the light trapping structure. This final device model has been named Model C3. This model was again simulated to investigate additional absorption enhancement and obtain a further improved absorption profile. The absorption profile, thus obtained, was used in our device simulation on ADEPT to obtain the maximally enhanced efficiency and parameters of our optimal photovoltaic system using Model C3.

4.2.2 Light Trapping Structure

In solar cells with simple geometrical structures, the incident light rays enter the cell through the front surface and, if not absorbed, leave through the rear surface of the cell, or are reflected back into the material if there is a planar reflector surface. Many sophisticated arrangements and complex structures have been developed that extend the effective path length of light inside the device; this is often referred to as optical confinement or light trapping. In photovoltaics, light

trapping is used to reduce the thickness of the cell without lowering the light absorption within the cell. Light trapping can also be used to enhance the open-circuit voltage [18], [19]. With an appropriate light trapping structure, a thinner solar cell can retain the absorption of the thicker device and also have a higher voltage.

Consequently, an optimum solar cell structure with light trapping is one in which the optical path length is several times the actual device thickness, where the optical path length of a device is the distance that an unabsorbed photon travels within the device before it escapes out of the device. A solar cell with no light trapping features will usually have an optical path length of one device thickness, while a solar cell with good light trapping may have an optical path length of up to 50, indicating that light bounces back and forth within the cell many times [17], [152]. Light trapping is achieved by changing the angle at which light travels in the solar cell. A textured surface will couple light obliquely into the photovoltaic material, thus giving a longer optical path length than the physical device thickness.

Optically thin absorbers support discrete guided modes, with a photonic mode density that is dependent on the thickness and material properties of the film. In general, the maximum enhancement is reduced as the number of available guided modes is decreased [153]. Periodic grating structures can couple diffracted light into specific modes within a narrow wavelength range [154]. This provides a mechanism of coupling into guiding modes in the active materials as the solar cell exhibits the trapping of light.

One-dimensional (1D) surface gratings have become one of the most studied diffractive structures [154], [155] used in light trapping. Simple grating lines diffract the incident light to the absorbing material and significantly increase the interaction length of long wavelength photons. The single-pass absorption of photons in the band edge region of the active material is very low. An appropriately design 1D grating structure can significantly enhance the absorption of the incident photons around the band edge by light trapping [156].

The materials in our solar cell support guided optical modes. In the region where the absorption of the active layer is weak, these guided modes typically have a propagation distance along the film that is much longer than the thickness of the film. Light trapping is accomplished by coupling incident plane-waves into these guided modes with the 1D grating structure [157]. As

long as the periodicity and height of the grating are appropriately designed, i.e. at least comparable to the free-space wavelength of the incident light, each incident plane-wave can couple into at least one guided mode. Similarly, such a guided mode can couple to external planewaves, creating a guided resonance [158].

In this work, we have considered a 1D grating structure composed of silver for light trapping in our solar cell design, since silver is highly reflective, and it is easy to fabricate and integrate with a variety of photovoltaic systems. We have explored various parameters of the light trapping structure design and investigated a wide range of grating periods and heights. For each configuration of the light trapping structure, the device performance of our solar cell model was obtained and compared for the cases with and without the silver grating layer.

The simulations of our device model with the light trapping structure were carried using the tool S4 on nanoHUB [151]. In order to accurately model the light trapping in our solar cell, precise knowledge of the imaginary part of the dielectric function of silver, i.e. the extinction coefficient, is very important. The dielectric function of the light trapping grating material was obtained from the PhotonicsDB tool on nanoHUB [101]. We used our initial solar cell model and added a 1D grating layer of silver with the appropriate period and height for our light trapping structure (Model C2). This gave us the new absorption profile of our photovoltaic system, and enabled us to study the absorption enhancement of the incident solar radiation due to the effect of light trapping from the 1D silver grating. The new absorption profile was used in the device modeling simulations in ADEPT to investigate improvement of our device performance in the space solar spectrum.

4.2.3 Anti-Reflection Coating Layer

For most semiconductors, a large portion of the incident radiation is lost by surface reflection. This loss can be reduced by a great extent by using a suitable anti-reflection coating layer which minimizes surface reflection for a range of wavelengths in the incident spectrum. Anti-reflection coatings consist of a thin layer of dielectric material, with a specially chosen refractive index and thickness, such that interference effects in the coating cause the wave reflected from the top surface of the anti-reflection coating to be out-of-phase with the wave reflected from the semiconductor

surface [19]. These out-of-phase reflected waves interfere destructively with one another which results in net zero reflected energy, as shown in Figure 20.

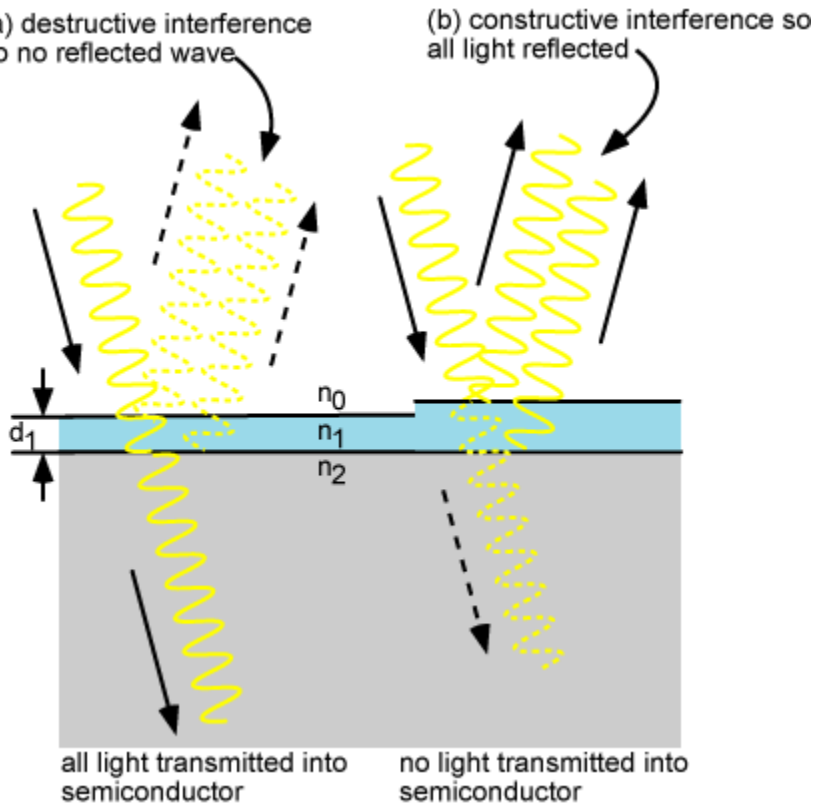

Figure 20. Constructive and destructive interference due to dielectric coating [21].

For our solar cell model, we have chosen a thin layer of a dielectric (an anti-reflection coating) to reduce the reflection of light from the front surface of the cell. The reflection coefficient from a bare semiconductor material for light incident from air is given by:

$$R = \frac{(\mathbf{n}-1)^2 + k^2}{(\mathbf{n}-1)^2 + k^2}$$

where **n** is the refractive index and k is the extinction coefficient of the semiconductor, both in general functions of the wavelength λ of light in vacuum. The extinction coefficient is related to the absorption coefficient α by

$$k = \frac{\alpha\lambda}{4\pi\mathbf{n}}$$

For a single layer anti-reflection coating of refractive index $\mathbf{n_{ar}}$ between a top medium of refractive index $\mathbf{n_0}$ (glass or air) and a semiconductor of refractive index $\mathbf{n_{sc}}$, the reflection coefficient becomes:

$$R = \frac{r_0^2 + r_{sc}^2 + 2r_0 r_{sc}\cos(2\beta)}{1 + r_{sc}^2 + 2r_0 r_{sc}\cos(2\beta)}$$

where

$$r_0 = \frac{\mathbf{n_{ar}} - \mathbf{n_o}}{\mathbf{n_{ar}} + \mathbf{n_o}}\ ; \quad r_{sc} = \frac{\mathbf{n_{sc}} - \mathbf{n_{ar}}}{\mathbf{n_{sc}} + \mathbf{n_{ar}}}\ ; \quad \beta = \frac{2\pi}{\lambda}\mathbf{n_{ar}}d$$

and d denotes the thickness of the coating. The transmission coefficient is:

$$T = 1 - R$$

In most cases of interest for all practical purposes, both r_0 and r_{sc} are positive and R goes to zero when:

$$d = \frac{\lambda}{4\mathbf{n_{ar}}};\ \frac{3\lambda}{4\mathbf{n_{ar}}}\ ;\ \frac{5\lambda}{4\mathbf{n_{ar}}}\ , \ldots\ldots$$

$$\mathbf{n_{ar}} = \sqrt{\mathbf{n_0}\,\mathbf{n_{sc}}}$$

The first value of d is often used under the name of quarter-wavelength rule in all practical applications since $\lambda/\mathbf{n_{ar}}$ is the wavelength of light in the anti-reflection coating material. The thickness of the anti-reflection coating is chosen so that the wavelength in the dielectric material is one quarter of the wavelength of the incoming wave. For a quarter wavelength anti-reflection coating of a transparent material with a refractive index $\mathbf{n_{ar}}$ and light incident on the coating with a free-space wavelength λ_0, the thickness d which causes minimum reflection is:

$$d = \frac{\lambda_0}{4\mathbf{n_{ar}}}$$

Reflection is further minimized if the refractive index of the anti-reflection coating is the geometric mean of that of the materials on either side; that is, glass or air and the semiconductor.

$$\mathbf{n_{ar}} = \sqrt{\mathbf{n_0}\,\mathbf{n_{sc}}}$$

For our system, there is vacuum on top of the dielectric layer, which makes the optimized refractive index of the anti-reflection coating:

$$\mathbf{n_{ar}} = \sqrt{\mathbf{n_{sc}}}$$

While the reflection for a given thickness, refractive index and wavelength can be reduced to zero using the equations above, the refractive index of a material is dependent on wavelength; so, zero reflection occurs only at a single wavelength λ_0. For our system, the value of this wavelength is chosen where the reflection from the solar cell is the greatest. This can lead to the maximum enhancement of the incident radiation absorption.

The simulations of our device model with the anti-reflection coating layer were carried using the tool S4 on nanoHUB [151]. The dielectric function of the anti-reflection coating material was obtained from the PhotonicsDB tool on nanoHUB [101]. We used our initial solar cell model together with the light trapping structure and added a suitable dielectric layer on top with the appropriate refractive index and thickness (Model C3). This gave us the new absorption profile of our photovoltaic system, and enabled us to study the absorption enhancement of the incident solar radiation due to the effect of anti-reflection coating. The new absorption profile was used in the device modeling simulations in ADEPT to investigate improvement of our device performance in the space solar spectrum.

4.3 Results and Discussion

4.3.1 Absorption Enhancement due to Light Trapping

The absorption enhancement in our photovoltaic device due to the light trapping structure is shown in Figure 21. It can be seen that there is significant improvement in the absorption of the incident solar radiation as a result of addition of the 1D silver grating structure which enhances the light absorption in our device. When normalized with the AM0 solar spectrum irradiance [117], the improved absorption corresponds to an enhancement of the short-circuit current (J_{SC}) by about 26% for the optimized grating structure. The optimal light trapping structure was obtained by investigating the silver grating period and height which gave the maximum enhancement of absorption of the AM0 solar spectrum.

The 1D silver grating diffracts the incident light back into the absorbing material and significantly increase the interaction length of long wavelength photons. The single-pass absorption of incident photons in the band edge region (1.3-1.7 eV) of the active materials of our

solar cell is very low. An appropriately designed 1D grating structure with silver significantly enhances the absorption of the incident photons around this energy range by light trapping.

In the region where the absorption of the active layers is weak, the guided modes have a propagation distance along the material that is much longer than the thickness of the device. The incident plane-waves diffracted by the light trapping structure are coupled into these guided modes with the 1D silver grating. As long as the periodicity and height of the grating are appropriately designed, each incident plane-wave in the low absorption region can couple into at least one guided mode, leading to significantly enhanced absorption in our solar cell.

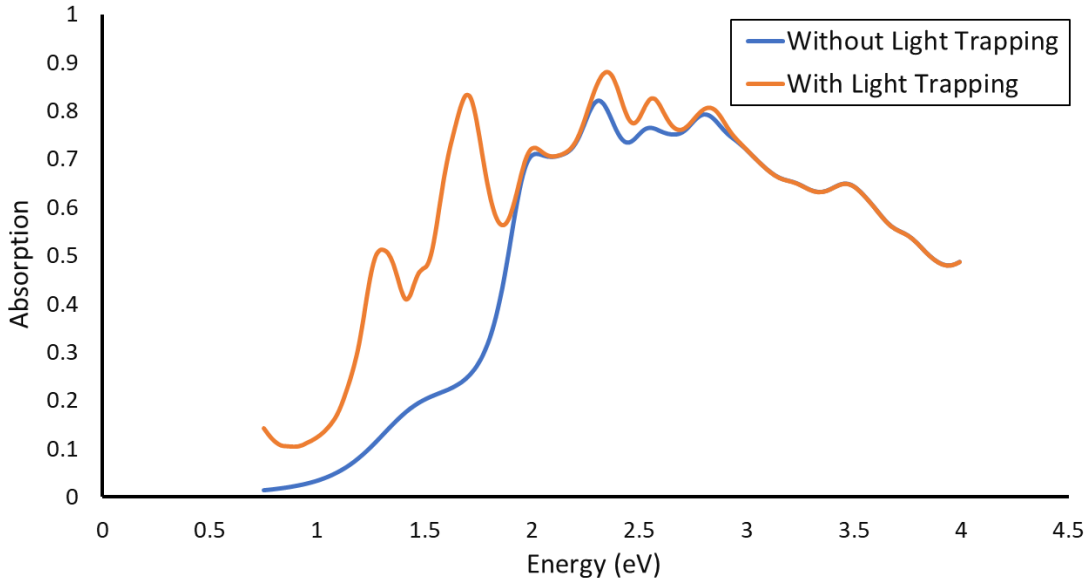

Figure 21. Absorption enhancement with light trapping structure (Model C2).

The peaks in the original absorption profile of our solar cell corresponds to the resonance modes in the active materials which are absorbed in our device. The resultant absorption spectrum consists of additional peaks, each corresponding to a guided resonance. The low energy incident photons are diffracted by the 1D grating into the resonance modes of the material, leading to a much longer optical path of these photons in the solar cell material. These guided modes have a propagation distance along the material that is much longer than the thickness of the device. The incident plane-waves diffracted by the light trapping structure are coupled into these guided modes

with the 1D silver grating. The absorption of incident radiation is strongly enhanced in the vicinity of each resonance.

However, a major limitation of a 1D grating light trapping structure is that each individual resonance has a narrow spectral width. In order to enhance absorption over a substantial portion of the solar spectrum and obtain broadband absorption enhancement, it is essential to design a much more complex light trapping architecture (for example, 2D gratings and grooves) which can additionally create a collection of significantly wider peaks over the energy range of the photons in the incident solar radiation.

The enhancement of J_{SC} in our photovoltaic system for various geometries of the 1D silver grating are summarized in Figure 22 and Table 14. The period and height of the grating were optimized to obtain the structure with the maximum absorption enhancement. It can be seen that the maximum enhancement of absorption is obtained from the grating with a height of 100 nm. The enhancement increases with the higher periodicity of the grating up to a period of 210 nm, and then drops off after the threshold value. The maximum enhancement of the device performance is obtained for a grating with height 100 nm and period 210 nm; this corresponds to an improvement of the J_{SC} by 26.4%.

Table 14. J_{SC} enhancement for various light trapping grating heights and periods (Model C2).

J_{SC} Enhancement (%)

Period (nm) \ Thickness (nm)	**100**	**200**	**300**	**400**
110	18.6	16.4	13.8	11.3
160	22.7	20.1	17.6	15.4
210	26.4	23.9	21.4	18.9
270	20.8	18.2	16.1	13.5
335	14.2	11.9	9.4	7.2

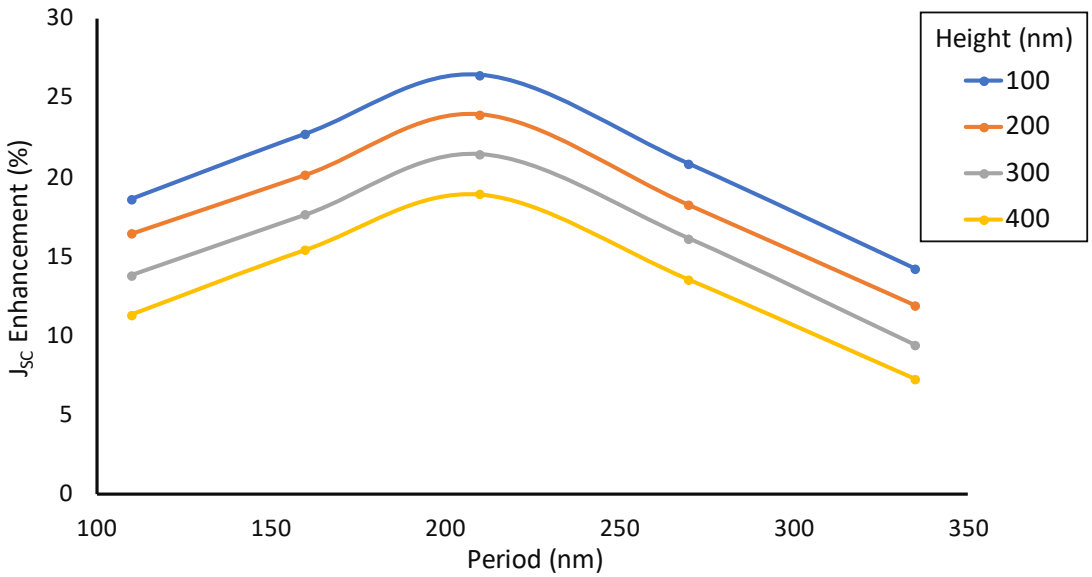

Figure 22. J_{SC} enhancement for various light trapping grating heights and periods (Model C2).

For our optimized photovoltaic Model C2, we have taken our light trapping structure as a periodic 1D silver grating with period 210 nm and height 100 nm to obtain the maximum enhancement of device performance arising from improved absorption of incident solar radiation. Although we could have investigated much finer and complex grating geometries, we decided to limit our features to measurements of 100 nm or higher to account for experimental considerations. We took these measures to propose models which are consistent with experimentally fabricable and measurable devices.

4.3.2 Absorption Enhancement due to Anti-Reflection Coating

Using our optimized photovoltaic Model C2, having a periodic 1D silver grating with period 210 nm and height 100 nm as the optimized light trapping structure, we added a dielectric material layer on top to function as an anti-reflection coating. This photovoltaic model with the additional modification has been named Model C3.

The refractive index of WS_2 is around 3 for incident photons of energies 1.5-3 eV which corresponds to the region of high intensity in the AM0 solar spectrum [159], [160]. The ideal refractive index of our dielectric layer should be:

$$\mathbf{n_{ar}} \approx \sqrt{3} \approx 1.7$$

But the major purpose of this work is not to present an ideal system with the highest theoretical performance using near-ideal device parameters and operating conditions. The goal of this project is to present an experimentally realizable device architecture with performance as close as possible to experimental conditions. We have proposed models which are consistent with experimentally fabricable and measurable devices, and would give the predicted performance and features when tested and characterized experimentally.

We have chosen our dielectric layer with a refractive index ($\mathbf{n_{ar}}$) of 1.5, which is similar to glass (SiO_2). Our proposed material for our anti-reflection coating is Spin-on-Glass (SOG) which can be accurately and uniformly deposited as a coating layer with sub-micron thickness on a variety of semiconductor materials [161], [162].

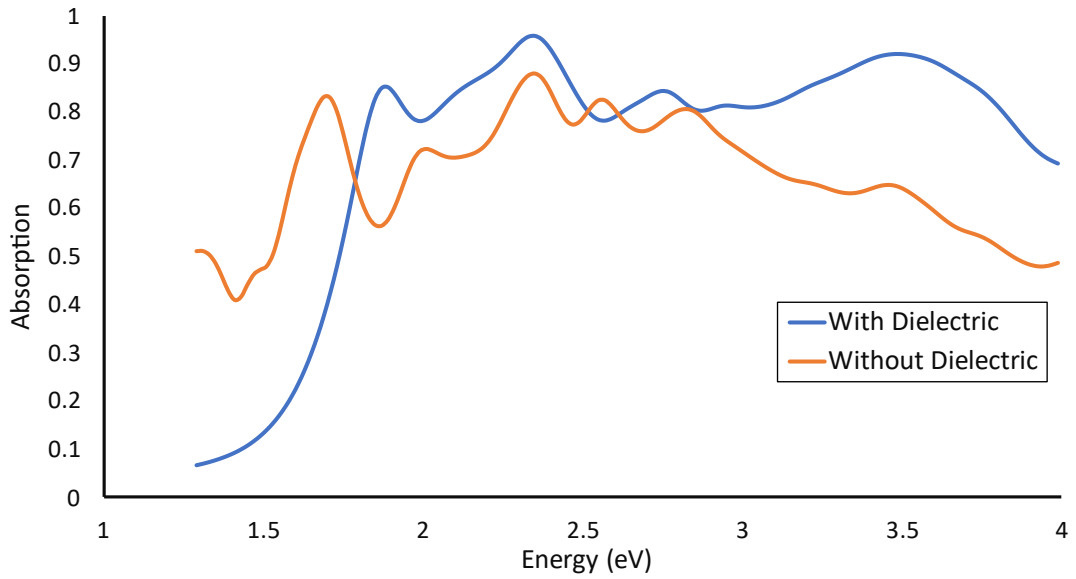

Figure 23. Absorption enhancement with anti-reflection coating dielectric layer (Model C3).

Based on our choice of the dielectric material, we chose the starting thickness of the dielectric layer as 100 nm and investigated the additional absorption enhancement in our device. Our device is not a single material device; it has a complex architecture. The actual thickness of the dielectric layer which gave the best performance was obtained by exploring a range of layer thicknesses and converging on the optimal value. We looked at various thickness values ranging

from 100 nm to 200 nm and found that a thickness of 150 nm for the dielectric layer gives the best absorption enhancement by minimizing surface reflection.

The absorption enhancement in our device due to the anti-reflection coating layer is shown in Figure 23. We can see that there is significant improvement in the absorption of the incident solar radiation as a result of addition of the dielectric layer which reduces the surface reflection. When normalized with the AM0 solar spectrum irradiance [117], the improved absorption corresponds to an enhancement of the short-circuit current (J_{SC}) by about 15% for the optimized structure. Since our photovoltaic model structure consists of ultra-thin materials, the system is very responsive to the effect of the additional anti-reflection coating layer. There are several local maxima in the original absorption profile, which corresponds to the resonance modes of the materials. There are also several local minima, which corresponds to high surface reflection from the material. Due to the effect of the dielectric layer, there is a change in the absorption peaks of the material; the resonance modes are shifted which accounts for the higher absorption of the previously lower absorption minima in the absorption profile. The surface reflection for photons with energies in the local minima ranges is greatly reduced, which leads to the formation of new absorption peaks in the enhanced absorption profile resulting from changes in the resonance modes. The optimal dielectric layer was obtained by investigating the material structure which gave the maximum enhancement of absorption of the AM0 solar spectrum.

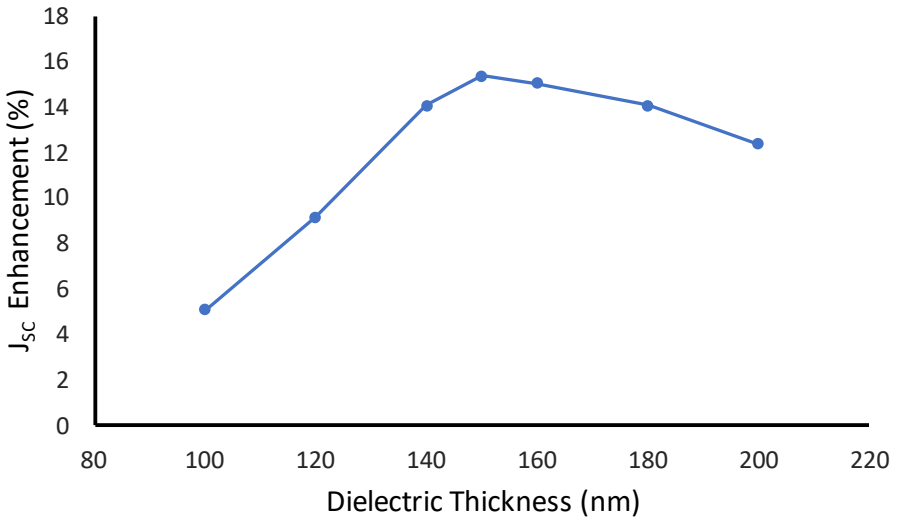

Figure 24. J_{SC} enhancement for various dielectric layer thicknesses (Model C3).

The enhancement of J_{SC} in our photovoltaic system for various thicknesses of the dielectric layer ranging from 100 nm to 200 nm are summarized in Figure 24. It can see that there is some enhancement of performance (about 5%) for a thickness of 100 nm; the enhancement increases with an increase in the thickness of the material. The maximum enhancement of the device performance is obtained for a 150 nm thick anti-reflection coating layer; this corresponds to an improvement of the J_{SC} by 15.4%. The absorption enhancement then drops again for thicknesses higher than 150 nm.

For our optimized photovoltaic device Model C3, we have taken our dielectric layer material with a thickness of 150 nm to obtain the maximum enhancement of device performance arising from improved absorption of incident solar radiation. Thus, our optimized Model C3 consists of a 150 nm thick dielectric layer with refractive index of 1.5 together with the optimized Model C2 having the optimized light trapping structure with a periodic 1D silver grating of period 210 nm and height 100 nm.

4.3.3 Performance Enhancement of Photovoltaic System

Initially, only our primitive solar cell Model C1 with the active layers was simulated to obtain the performance parameters. A suitable light trapping structure, composed of a periodic 1D silver grating with period 210 nm and height 100 nm, was then added to the solar cell (Model C2); this new system was simulated to investigate the enhancement of device performance. Our final device (Model C3) consists of appropriate anti-reflection coating layer in addition to the light trapping structure. This model is composed of a 150 nm thick dielectric layer with refractive index of 1.5 together with the optimized light trapping structure having a periodic 1D silver grating of period 210 nm and height 100 nm. This was again simulated to investigate additional performance enhancement and obtain a further improved photovoltaic device. The device models were simulated on ADEPT for two temperatures (313K and 343K).

The performance parameters of our three photovoltaic models, such as short circuit current density (J_{SC}), open circuit voltage (V_{OC}) and efficiency, were recorded for both the cases temperatures 313K (Table 15) and 343K (Table 16). The current-voltage relationship of our

models (C1, C2 and C3), showing the J_{SC} and V_{OC}, for both the temperatures are shown in Figure 25 (313K) and Figure 26 (343K).

Table 15. Performance parameters of device models C1, C2 and C3 at 313K.

Model	**C1**	**C2**	**C3**
Open Circuit Voltage V_{OC} (V)	0.86	0.87	0.87
Short Circuit Current Density J_{SC} (mA/cm^2)	31.8	40.2	46.4
Efficiency (%)	15.8	20.4	23.6

Table 16. Performance parameters of device models C1, C2 and C3 at 343K.

Model	**C1**	**C2**	**C3**
Open Circuit Voltage V_{OC} (V)	0.81	0.82	0.82
Short Circuit Current Density J_{SC} (mA/cm^2)	31.8	40.2	46.4
Efficiency (%)	14.3	18.5	21.4

The open circuit voltage (V_{OC}) for Model C1 at 313K was obtained to be 0.86 V and the short circuit current density (J_{SC}) was 31.8 mA/cm^2; the efficiency of the solar cell was 15.8%. The open circuit voltage (V_{OC}) obtained is similar to that of many conventional solar cells; the short circuit current density (J_{SC}) is reasonable for a solar cell, although well below the performance of most commercial photovoltaic systems [15], [138]. While the overall efficiency is not very high, it is promising as a starting point to systematically improve our device.

This initial device was then modified by adding the light trapping structure (Model C2). For the optimized device structure of Model C2, the open circuit voltage (V_{OC}) was 0.87 V and the short circuit current density (J_{SC}) was 40.2 mA/cm^2; the efficiency of the solar cell was 20.4%. This enhancement of the J_{SC}, and correspondingly efficiency, is the result of improved absorption of the incident solar radiation from the additional light trapping structure.

Compared to Model C1 discussed previously, the short circuit current density (J_{SC}) increases greatly by about 26%, and is now comparable to that of current space photovoltaic technology. Overall, the efficiency of the device Model C2 is significantly higher than C1, and is comparable to commercial solar cells. The results are very promising, but it is possible to improve the device even further, since there are still losses due to surface reflection of the incident radiation.

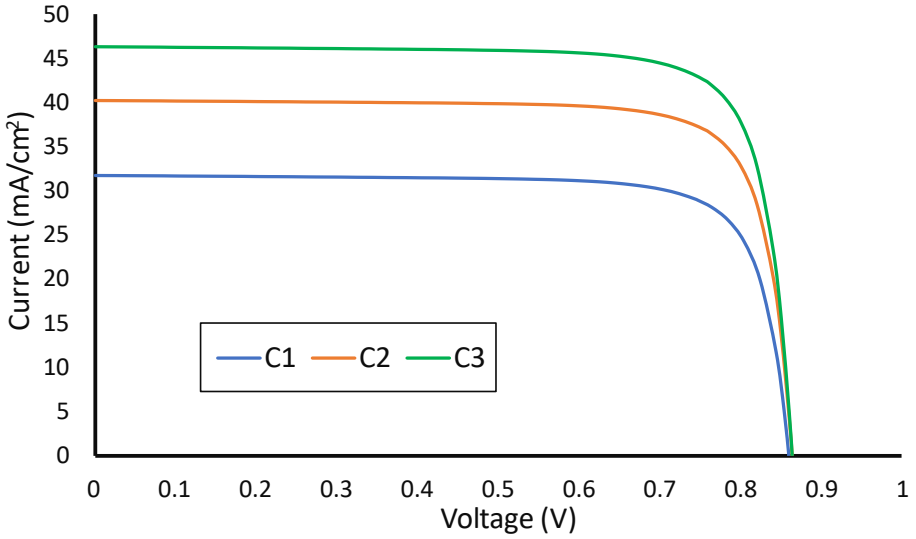

Figure 25. Current-Voltage characteristics of our photovoltaic models at 313K.

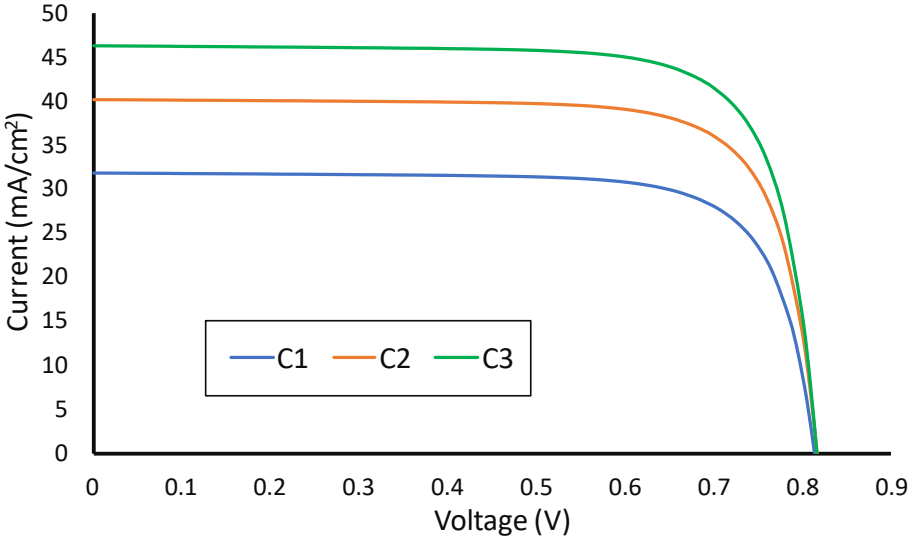

Figure 26. Current-Voltage characteristics of our photovoltaic models at 343K.

The device Model C2 was further modified by incorporating an anti-reflection coating layer on top (Model C3). The performance of our final device Model C3 is found to be much improved because of additional absorption arising from reduction of surface reflection. For the optimized device structure of Model C3, the open circuit voltage (V_{OC}) was 0.87 V and the short circuit current density (J_{SC}) was 46.4 mA/cm^2; the efficiency of the solar cell was 23.6%. The short circuit current density (J_{SC}) for Model C3 is much better than the previous structures (models C1 and C2), and has increased significantly (by about 46% relative, compared to the initial device Model C1). Overall, the efficiency of the solar cell model is very high, and comparable to many high-efficiency single junction solar cells.

The performance trends are similar for a temperature of 343K. For Model C1, the open circuit voltage (V_{OC}) was obtained to be 0.81 V, the short circuit current density (J_{SC}) was 31.8 mA/cm^2, and the efficiency of the solar cell was 14.3%. For Model C2, the open circuit voltage (V_{OC}) was 0.82 V, the short circuit current density (J_{SC}) was 40.2 mA/cm^2, and the efficiency of the solar cell was 18.5%. For Model C3, the open circuit voltage (V_{OC}) was 0.87 V, the short circuit current density (J_{SC}) was 46.4 mA/cm^2, and the efficiency of the solar cell was 21.4%. The expected drop in the efficiency at the higher temperature arises from the reduction of the V_{OC} due to increase in temperature. This enhancement of the J_{SC}, and correspondingly efficiency, is the result of improved absorption of the incident solar radiation from the additional light trapping structure and anti-reflection coating layer.

We have incorporated a light trapping structure and an anti-reflection coating layer in our solar cell model to increase the absorption of the incident solar radiation, and lead to better performance of the device with higher current. The additional optical features in our device lead to an enhancement of the J_{SC} resulting from the increased photon absorption, without affecting the V_{OC}. Our goal in this project was to increase the device performance efficiency through enhancement of the J_{SC}; we have not explored mechanisms of increasing the V_{OC} in this study.

In addition, there is no significant deterioration of the intrinsic bandgap energy of WS_2 due to the effect of increase in the temperature. For a temperature increase from 313K to 343K, the bandgap of WS_2 reduces by around 8-9 meV [148]. This is similar to the drop in the bandgap

energy value for silicon; it's bandgap drops by around 10 meV for increase in temperature from 313K to 343K [163].

We have analyzed the proton stopping power *S(E)* of WS_2 and silicon, and also compared the parameters to those of lead which is known to be very resistant to radiation. We obtained the stopping power for high energy protons with energies 1-100 MeV, as shown in Table 17 [164]. The retarding effect on the protons due to the proton stopping power is almost linear in the depth of the material. Using the proton stopping power, we calculated the mean range, or continuous slowing down approximation (CSDA) range, of the protons inside the materials for energies 1-100 MeV. Our results are summarized in Table 18.

$$\Delta x = \int_0^{E_0} \frac{1}{S(E)} dE$$

For a 1 MeV proton, the stopping power of WS_2 is about 20% higher than that of silicon. If we look at higher energy protons of 10-100 MeV, we can see that the stopping power of WS_2 is almost double that of silicon. For comparison, the stopping power of lead is about thrice as much as that of silicon for high energy protons. If we look at the CSDA ranges for the protons with energies 10-100 MeV, the range in silicon is almost twice that of WS_2 and about thrice that of lead. From these results, it can be concluded that WS_2 has a much higher radiation resistance than silicon; WS_2 is intermediate of silicon and lead in terms of resistance to radiation.

Table 17. Proton stopping powers for silicon, WS_2 and lead (MeV/cm).

Proton Energy (MeV)	***S(E)* Silicon**	***S(E)* WS_2**	***S(E)* Lead**
1	404.7	478.7	711
10	80.6	136.5	200.8
50	22.9	45	65.5
100	13.6	27.2	40.1

Table 18. CSDA ranges for silicon, WS_2 and lead (μm).

Proton Energy (MeV)	Δx Silicon	Δx WS_2	Δx Lead
1	17	15	11
10	715	461	312
50	12240	6577	4479
100	41790	21280	14632

If we compare a 10 μm thick silicon solar cell and 10 μm thick WS_2 solar cell, the WS_2-based device is twice as much resistant than silicon on exposure to high energy proton radiation (10-100 MeV). Furthermore, if we compare two WS_2-based solar cells of thicknesses 200 nm and 10 μm, we can infer that our 200 nm ultra-thin device is about 50 times more resistant to radiation than the 10 μm device due to the reduction of thickness. On comparison of our 200 nm WS_2-based solar cell to a 10 μm thick silicon-based solar cell, it can be concluded that our device is around 100 times more resistant to radiation-induced damage compared to the silicon device. Thus, by using an ultra-thin WS_2-based solar cell, we can achieve an enhancement of the resistivity to high energy radiation by a couple of orders of magnitude in the space environment.

It has been demonstrated in recent studies that solar cells with thicknesses of the order of a micron are prone to significant damage from high energy radiation [147]. The primary reason behind this degradation is the reduction of the minority carrier diffusion lengths on exposure to radiation. This leads to a loss of free carriers due to recombination in the material, and reduced carrier collection efficiency at the end contacts. However, a solar cell with a thickness of around 100-200 nm is much more resistant to this effect. Even with a reduction of the minority carrier diffusion length, these devices are enough thin for efficient carrier collection of the photon-generated free carriers in the material. Since our device has a thickness of 200 nm, we expect there won't be significant degradation of performance due to reduction of the minority carrier diffusion lengths, as most of the generated carriers will be collected efficiently at the end contacts due to the ultra-thin nature of our solar cell model.

These results create new possibilities for the fabrication and use of ultra-thin 2D high-efficiency solar cells for space photovoltaic applications using a new material which has the

advantages of ultra-low weight per unit of power production, mechanical flexibility, resilience and reliability, compared to several commonly-used photovoltaic materials in existing space photovoltaic systems.

4.4 Outlook and Conclusion

In this work, we have developed a solar cell model based on tungsten disulfide (WS_2) for proposed implementation in space photovoltaic applications. The electronic and optical properties of monolayer and bulk WS_2 were obtained from the results presented in Chapters 2 and 3. We carried out the device performance simulations with the AM0 space solar spectrum over the temperature range encountered in satellite orbits (313-343K).

Initially, we developed a baseline solar cell model with a total thickness of 200 nm, based on Model C presented in Chapter 3. This model gave reasonable performance with optimal efficiencies around 14.3-15.8% over the temperature range 313-343K. After adding a light trapping structure consisting of a 1D silver grating to our solar cell, the absorption of the incident was greatly enhanced. The overall efficiency of the optimal solar cell model with light trapping increased significantly to 18.5-20.4%, which is comparable to the performance of many commercial single-junction solar cells used in space applications. Further modification was made to our device by incorporating a dielectric material layer to function as an anti-reflection coating. The device performance of our final photovoltaic model was further enhanced to 21.4-23.6% due to reduction of surface reflection. These results show that a solar cell based on WS_2 have very favorable performance features and properties for use in space photovoltaics, along with the natural advantages of light weight, flexibility, earth abundance and resilience.

Our solar cell design shows that it is possible to obtain efficiencies above 20% with the space solar spectrum. We have solved the issue of low absorption in ultra-thin layers by incorporating a light trapping structure and an anti-reflection coating layer. The simulation results provide an insight towards development of an experimentally feasible solar cell model for space photovoltaic applications. Nonetheless, our photovoltaic system warrants further investigation, since there are several approaches that could lead to further improvement of performance of our device. In light trapping, simple grating lines are often regarded as disadvantageous, because one-dimensional structures mostly affect the absorption enhancement of a plane of incident angles

instead of the full hemisphere. In addition, 1D gratings lead to sharp and not broad resonance peaks in the absorption spectrum, restricting the absorption enhancement to only narrow wavelength intervals. Investigation of 2D light trapping architectures can lead further enhancement of our device performance. In our anti-reflection coating, there is room for improvement in further reduction of surface reflection of the incident radiation. It may be possible to design and fabricate a perfect anti-reflection coating layer using complex dielectric architecture to obtain even lower reflection of the incident spectrum.

We have taken measures and precautions in our simulations to propose models which are consistent with experimentally fabricable and measurable devices. We have accounted for non-idealities in our materials and device architecture wherever possible. The goal of this project was to present a solar cell model which would give the predicted performance and features when tested and characterized experimentally. Thus, we refrained from incorporating near-ideal device parameters and operating conditions.

5. ELECTRONIC PROPERTIES OF HYBRID TUNGSTEN-BASED TMDC ALLOYS AND OXIDES

5.1 Background

TMDCs have attracted significant attention in recent years due to their fascinating chemical and physical properties which make them attractive for a variety of electronic and optical applications. Most TMDCs have optically favorable bandgaps and promising electronic properties. The 2D layered structure of TMDCs makes it possible to modify and tune their electronic properties by doping with other atoms and manufacturing hybrid alloys. We have looked into ways to make these materials more versatile with further modification and tunability of their physical and chemical properties, advancing the work presented in Chapter 2.

It is possible to obtain alloys of binary TMDCs with more than one kind of chalcogen atoms [37], leading to the formation of hybrid TMDCs with tunable electronic and optical properties. In this work, we have explored monolayers of tungsten-based TMDC alloys containing sulfur and selenium, whose properties are intermediate between pure tungsten dilsulfide (WS_2) and pure tungsten diselenide (WSe_2) – for example, with tunable direct bandgaps dependent on the sulfur and selenium concentrations. TMDC alloys were investigated by altering the composition to contain more than one chalcogen atom, leading to hybrid TMDCs with tunable electronic and optical properties and significant dipole moments. The band structure and corresponding bandgap of pure and hybrid TMDCs were obtained by Density Functional Theory (DFT) calculations together with GW corrections using Quantum ESPRESSO [82], [84], [89], [94]. The calculated electronic properties of the hybrid TMDC alloys show a strong linear dependence on their respective chalcogen compositions; this allows for fabrication of TMDCs with any target desirable bandgaps. The TMDC alloys exhibit tunability of electronic properties and other unique features which allow for a variety of novel applications.

This work has been presented in *2019 IEEE 46th Photovoltaic Specialists Conference (PVSC)*, pp. 0772-0776. IEEE, 2019.

It has also been published in *Advanced Functional Materials*, March 2021.

Ultrathin 2D TMDCs for photovoltaics have gained considerable interest; but it also essential to consider related, robust materials which are resistant to atmospheric conditions and extremities. Transition metal oxides have significant potential for photovoltaic applications as a wide bandgap semiconductor [40], [41]. Transition metal oxides are very sturdy and resistant to atmospheric degradation. Tungsten trioxide (WO_3) is a particularly versatile material; it can be deposited on and is compatible for fabrication with many semiconductors. It also has strong absorption for high energy photons. The electronic properties of WO_3 were also investigated with DFT calculations. The electronic band structure, bandgap and density of states were calculated to study the unique features of this material and explore possible electronic and optical applications. The electronic properties of WO_3 make it suitable for implementation as a wide-bandgap semiconductor in solar cells. It can be used in tandem with existing solar cells, or as the top junction of a multi-junction solar cell.

5.2 Theory and Methods

5.2.1 Hybrid Tungsten-based TMDC Alloys

TMDCs have a trigonal prismatic structure where each layer consists of a plane of hexagonally arranged transition metal atoms sandwiched between two planes of hexagonally arranged chalcogen atoms [74]–[76], as shown in Figure 27. The thickness of a single layer of a typical TMDC is 3.2 Å, while multiple layers are separated from each other by empty space of separation around 3 Å. The fundamental unit cell of WS_2 has a trigonal prismatic structure, as shown in Figure 27, where the lattice parameter a is around 3.16 Å for WS_2 and 3.29 Å for WSe_2.

Tungsten-based monolayer TMDC alloys were investigated by altering the composition to contain more than one chalcogen atom, leading to hybrid TMDCs with tunable properties. We have studied monolayers of tungsten-based TMDC alloys containing both S and Se atoms; the bandgap is an intermediate value depending on the chalcogen composition. To simulate the alloys and understand their properties, we modeled a periodic supercell containing four individual unit cells of the TMDC containing a total of 4 tungsten atoms and 8 chalcogen atoms. The composition of tungsten was kept fixed at 4 atoms. The pure TMDC layers were modeled by using 8 S atoms for WS_2 and 8 Se atoms for WSe_2 in a monolayer configuration. The alloys were modeled by

introducing both S and Se atoms together in the supercell of the monolayer, in all possible combinations starting from pure WS_2 to pure WSe_2, to obtain a hybrid structure. We started from a supercell of pure WS_2; then, we replaced a S atom with a Se atom to obtain a hybrid alloy with 87.5% S and 12.5% Se concentrations. We investigated various hybrid alloys by replacing a S atom in the supercell with a Se atom to obtain structures with 12.5%, 25%, 37.5%, 50%, 62.5%, 75% and 87.5% Se concentrations. A cell relaxation calculation was carried out for each of alloy to obtain the lattice parameter of the supercell with the lowest energy and most stable structure. The band structure and corresponding bandgap of each alloy were obtained and studied to identify unique features of the hybrid materials.

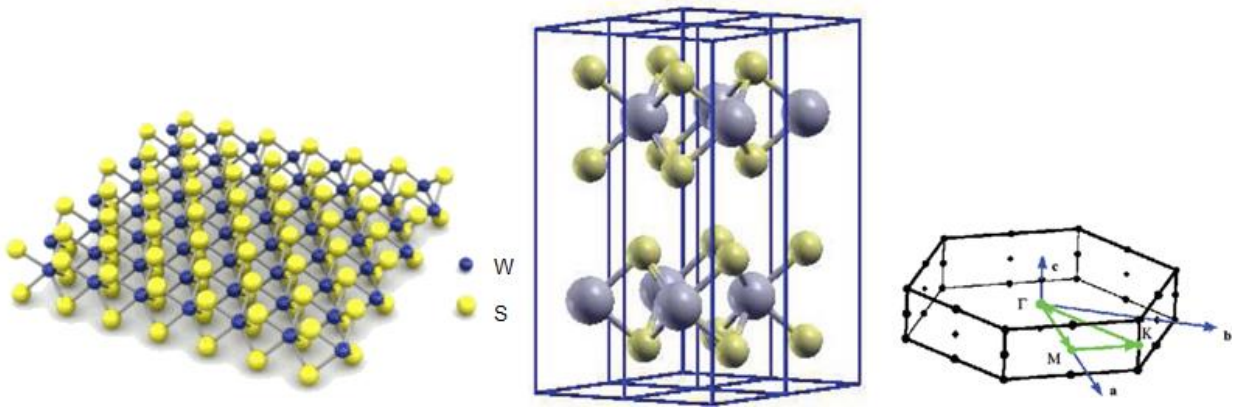

Figure 27. Left: 2D monolayer WS_2. Center: Trigonal prismatic structure of WS_2. Right: Brillouin zone with the k-point path (green) used to plot the band structure [74], [165].

5.2.2 Band Structure Calculation

The DFT calculation technique was used to investigate the electronic properties of the TMDC materials. DFT is a powerful quantum mechanical method to study properties of a material using many-body perturbation theory [82]. The DFT calculations were performed using the tool Quantum ESPRESSO [84], [166], [167]. Quantum ESPRESSO is a quantum mechanical modeling tool to simulate many-body systems. DFT calculations require pseudopotential files which simulate individual atoms from the periodic table. GGA pseudopotentials (which add gradient correction to the more basic LDA ones), as described by the Perdew-Burke-Ernzerhof (PBE) scheme [87], were used to simulate the W and S atoms. The Brillouin zone was sampled according

to the scheme proposed by Monkhorst-Pack [88] with a high-density in-plane 20×20×1 k-point grid with 400 k-points. Since TMDCs have an ultra-thin 2D structure, there is no electronic dispersion in the vertical out-of-plane direction. The bands were plotted along the k-point path as in Figure 27 (right, green). Additional details about DFT calculations and techniques have been discussed in Chapter 2.

Before getting started on the band structure calculations, it is important to identify the unit cell of the materials under study accurately. WS_2 and WSe_2 have the same trigonal prismatic unit cell with a thickness of 3.2 Å; but their unit cells have different lattice parameters. The lattice parameter of WS_2 is 3.16 Å, while that of WSe_2 is 3.29 Å; the lattice parameters of the alloys are intermediate values depending on the chalcogen composition. It is vitally important to use the correct lattice parameter for the simulations of the alloys in order to obtain accurate properties.

For each intermediate alloy, a cell relaxation calculation was carried out with the unit cell to find the corresponding lattice parameter. A relax calculation is simulation carried out for a unit cell or super cell to obtain the most stable structure with the lowest energy [84]. It is an iterative process to find the optimum cellular dimensions of the stable structure. The most primitive relaxation calculation involves changing the cellular dimensions in small increments to obtain the parameters which give the lowest energy, keeping the relative positions of the atoms intact. For a typical cell, all the dimensions are increased/decreased in increments to find the optimum cell dimensions which exhibit the lowest energy and hence the most stable structure.

For our choice of TMDC materials, both WS_2 and WSe_2 have the same unit cell height. So, it is a fair assumption that all the intermediate alloys will also have a unit cell of similar height. We have kept this parameter fixed in our calculations in order to run faster simulations. The only cell dimension which is varied in our simulations is the in-plane lattice parameter which varies from 3.16 Å to 3.29 Å depending on the alloy composition. Initial cell relaxation calculations were carried with WS_2 and WSe_2 to validate our methodology and simulation techniques. Starting from both higher and lower initial values, we were able to obtain the relaxed lattice parameters of 3.16 Å and 3.29 Å for WS_2 and WSe_2, respectively. For the hybrid monolayer TMDCs, the relaxation calculations were carried for each alloy ranging from 12.5% to 87.5% Se concentrations, corresponding to 2-7 Se atoms in the defined input cell. Using the calculated lattice parameters of

the intermediate alloys, the band structure and corresponding bandgap were calculated for each material under consideration.

The band structure obtained from DFT gives accurate information about the shape of the energy bands (such as valence band maxima and conduction band minima), but the bandgap is significantly underestimated. This problem was solved by formulating the electronic band structure using the GW approximation together with the DFT results; it involves the expansion of the self-energy in terms of the single particle Green's function G and the screened Coulomb interaction W to model many body systems [89], [92], [93]. The simulations were carried using the GWL package in Quantum ESPRESSO. The bandgap energy correction value obtained from the GW approximation was added to the DFT bands to account for the underestimation of the bandgap; however, for a TMDC monolayer, it is necessary to include the effect of the exciton binding energy [94]. The bandgaps of monolayer TMDCs obtained by DFT and GW calculations are higher than experimental results; this overestimation is due to the large excitonic effect in a two-dimensional system. When the energy correction due to the excitonic effect is subtracted from the DFT+GW bands, we get very accurate band structure and bandgap that match closely with experimental results [1], [2], [5]. All the calculations and simulations were carried out assuming a temperature of 300K.

The band structure calculations were validated using similar molybdenum-based TMDC alloys containing both S and Se atoms. Recent experimental studies have investigated electronic properties of such Mo-based hybrid alloys [37]. We have compared our results to the experimental studies to authenticate our calculations and simulation techniques. Our calculated results were in close agreement with the experimentally established electronic properties.

5.2.3 Dipole Moment of Hybrid TMDC Alloys

Pure TMDCs (WS_2 and WSe_2) have no dipole moment due to symmetrical structure. Introducing multiple chalcogen atoms in a hybrid material breaks the structure symmetry and leads to significant dipole moments. For each intermediate alloy, the electronic charge distribution in the unit cell was calculated, from which the net dipole moment per unit cell was obtained. The DFT results from the band structure calculation were used to obtain the charge distribution in the pure and hybrid TMDCs, from which the dipole moment of each material was calculated. The

calculations were performed using the post-processing operations in Quantum ESPRESSO [84]. The calculation methodology was initially tested with a water molecule to validate our simulation techniques. From our calculations, we obtained a dipole moment of 1.8 D for a single water molecule which is consistent with previously established results [168].

5.2.4 Structure and Electronic Properties of Tungsten Trioxide

Tungsten Trioxide (WO_3) is a layered material, similar to TMDCs, with a single layer thickness of 7 Å (Figure 28). It has an orthorhombic unit cell with in-plane lattice parameters of 3.70 Å and 3.96 Å [169]. Its stratified structure enables the addition of different donor atoms into the free spaces, and thus allowing for customizable physical and chemical properties. Bulk WO_3 consists of double-layers of linked distorted WO_6 octahedra (Figure 28). In each double-layer, WO_6 octahedra form edge-sharing zig-zag rows. The adjacent layers of WO_3 are held together only by weak van der Waals forces to make the lamellar formation, while the intra-layer interactions between W and O atoms within a single layer are dominated by strong ionic and covalent bonding. The nature of the W–O bond changes considerably with the equilibrium bond distance, and varies from strongly covalent for the shortest bond to predominantly ionic for the longest bonds in the WO_6 octahedron. The fundamental thickness of the double-layer structure of WO_3 including one van der Waals gap is 1.4 nm.

The structure of WO_3 is much more complicated to simulate, compared to most TMDCs. A unit cell of WO_3 was defined with 8 W atoms and 24 O atoms. In order to validate that our defined unit cell for WO_3 is the lowest energy and most stable structure, a cell relaxation calculation was carried out with the unit cell parameters to confirm that the lattice parameters are consistent with stability and lowest energy.

The electronic band structure and corresponding bandgap of WO_3 was obtained by DFT calculations, together with GW calculation for bandgap correction, using the tool Quantum ESPRESSO. GGA pseudopotentials were used to simulate the W and O atoms. The Brillouin zone was sampled according to the scheme proposed by Monkhorst-Pack with a 20×20×5 k-point grid consisting of 2000 k-points.

The band structure calculation results from the DFT simulations were used to obtain the density of states of WO_3 to get an in-depth understanding of the electron distribution in the valence bands and available states in the conduction bands. This would give us a broad overview and important information about the optical properties of this material, such as availability of electrons for excitation from the valence bands, photons with energies which can be most favorably absorbed, and the concentration of electrons which can be excited to the conduction bands. These features will be useful in determining possible implementations of WO_3 in electronic and photonic applications. The density of state calculations were performed using the post-processing operations in Quantum ESPRESSO [84].

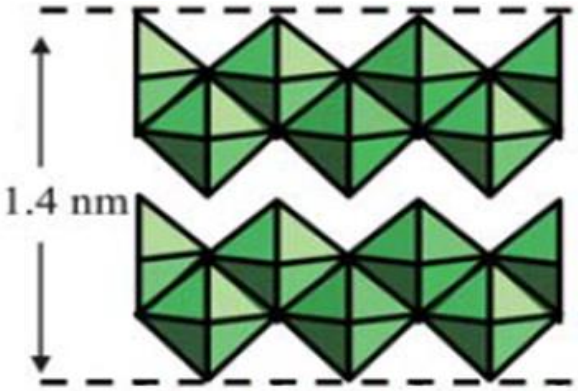

Figure 28. Structure of Tungsten Trioxide (WO_3) [169].

5.3 Results and Discussion

5.3.1 Band Structure of Tungsten-based TMDC Alloys

The lattice parameters of unit cells for WS_2 and WSe_2 were known from previous experimental studies and referenced literature, and further verified by our cell relaxation calculations using DFT simulations on Quantum ESPRESSO. The relaxation calculations for the intermediate alloys gave us the lattice parameters of the unit cells for each alloy. We investigated tungsten-based TMDC alloys containing both S and Se chalcogen atoms, with Se atom concentrations of 12.5%, 25%, 37.5%, 50%, 62.5%, 75% and 87.5%.

The height of the individual layers is around 3.2 Å for all the TMDC materials under consideration, regardless of the chalcogen composition. A relaxation calculation was not needed for the height of the unit cells. The in-plane lattice parameter varied depending on the constituent chalcogen atom composition. We obtained the in-plane lattice parameter for each of the seven hybrid alloys. It was found that the lattice parameter varies approximately linearly with the Se atom concentration; it increases proportionately with the Se atom composition starting from 3.16 Å (WS_2, 0% Se) to 3.29 Å (WSe_2, 100% Se). The results are summarized in Figure 29.

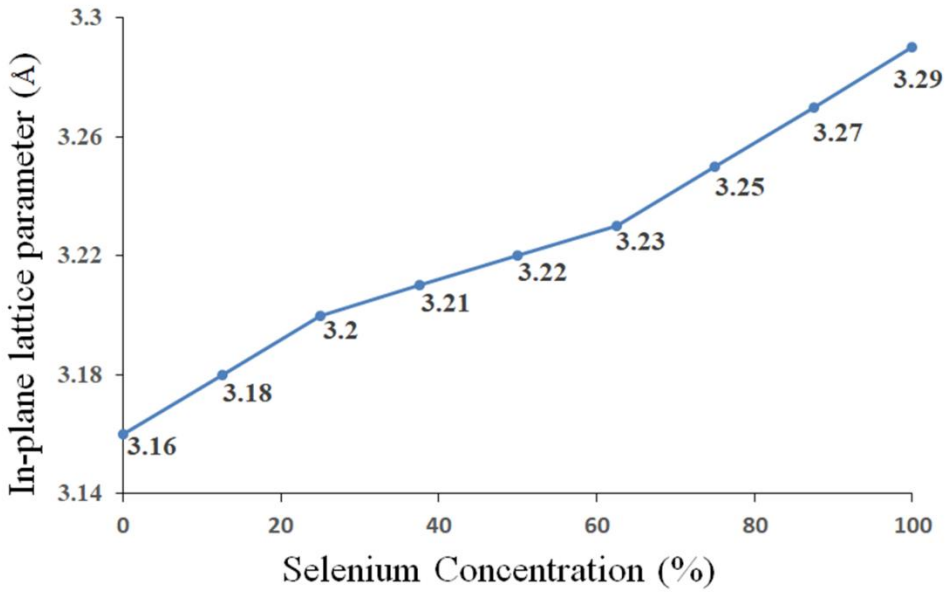

Figure 29. Variation of in-plane lattice parameter in a tungsten-based TMDC alloy as a function of selenium concentration.

Using the calculated lattice parameters for each alloy and the pure TMDCs, the unit cells and atomic locations were defined in our input files for the electronic band structure calculations. The electronic band structures and corresponding bandgaps of WS_2, WSe_2 and the intermediate alloys were obtained from the DFT calculations. The bandgaps of WS_2 and WSe_2 were found to be 2.15 eV and 1.67 eV, respectively. These values are consistent with experimental studies on tungsten-based TMDCs [166], [170]. For a tungsten-based TMDC alloy containing both S and Se atoms, the bandgap is an intermediate value between 1.67 eV and 2.15 eV depending on the chalcogen composition. It was found that the bandgap of the alloys exhibits an inverse linear relationship with the corresponding Se atom concentration; it shows an approximately linear

decrease with increasing Se concentration from WS_2 (2.15 eV) to WSe_2 (1.67 eV). The results are summarized in Figure 30.

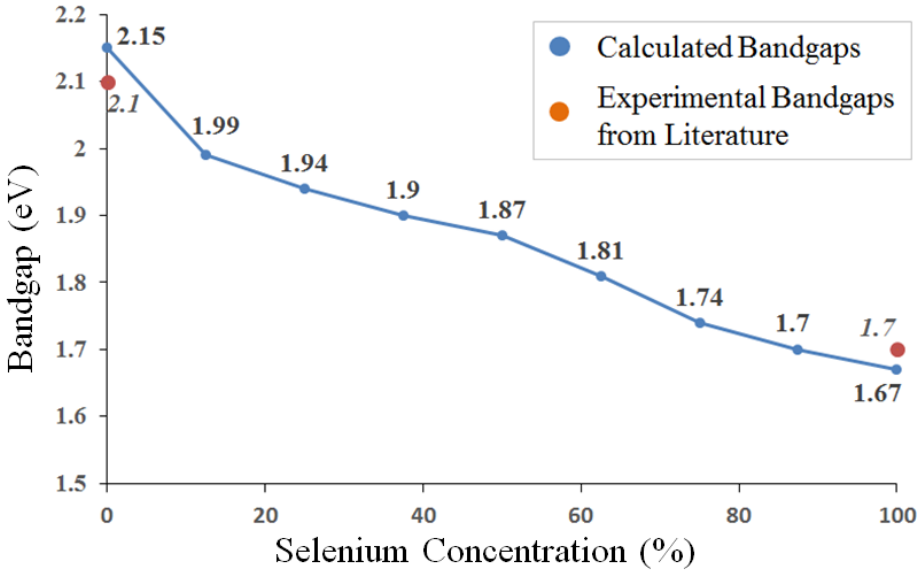

Figure 30. Variation of bandgap in a tungsten-based TMDC alloy as a function of selenium concentration and comparison to experimental bandgaps from existing literature.

The band structure of a monolayer of pure WS_2 is consistent with our results from Chapter 2 (section 2.3). The band structures of monolayers of pure WSe_2 and the hybrid alloy WSeS (50% S, 50% Se composition) are shown in Figure 31. The band structures of each material were plotted along the same k-point path in the Brillouin zone. The bandgaps of all the hybrid alloys are direct in nature, similar to WS_2 and WSe_2. The band structures of the pure and hybrid materials show similar features such as the valence band maximum (VBM), conduction band minimum (CBM), and other local extrema. It can be seen from the band structure figures that the direct transition point for electrons is located at the K-point in the Brillouin zone. Thus, we see that the hybrid tungsten-based alloys have very similar electronic properties compared to pure tungsten-based TMDCs. The primary feature which changes in each of the materials is the bandgap energy, which is dependent on the chalcogen composition. These results show that it is possible to engineer a material which can exhibit any desired bandgap for a target application. If we just consider a tungsten-based TMDC containing sulfur and selenium, it is possible to fabricate a hybrid material which can have any desirable direct bandgap in the range 1.67-2.15 eV, and also exhibit the

favorable electronic and optical properties of TMDC semiconductors. This unique feature can be extended for other TMDCs to obtain hybrid materials with any customizable bandgap over a wider energy range. This has the potential to open up new possibilities in fabrication and manufacture of tunable bandgap semiconductors.

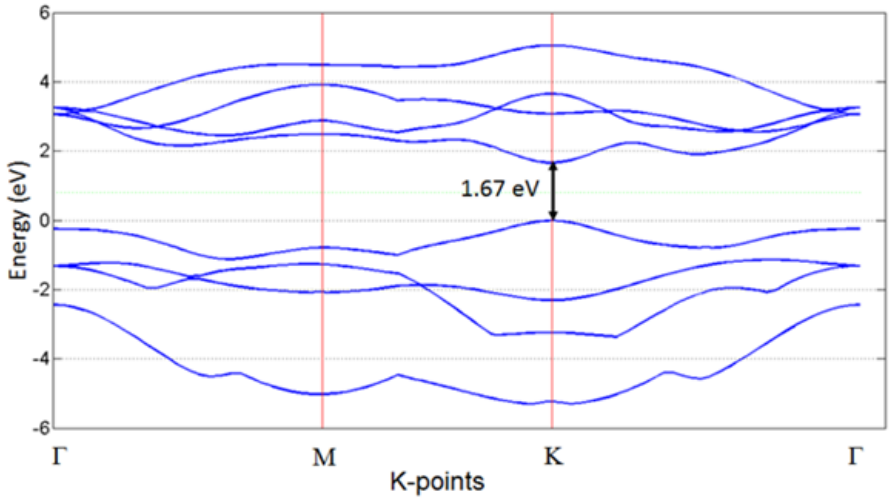

(A) Pure Tungsten Diselenide (WSe_2)

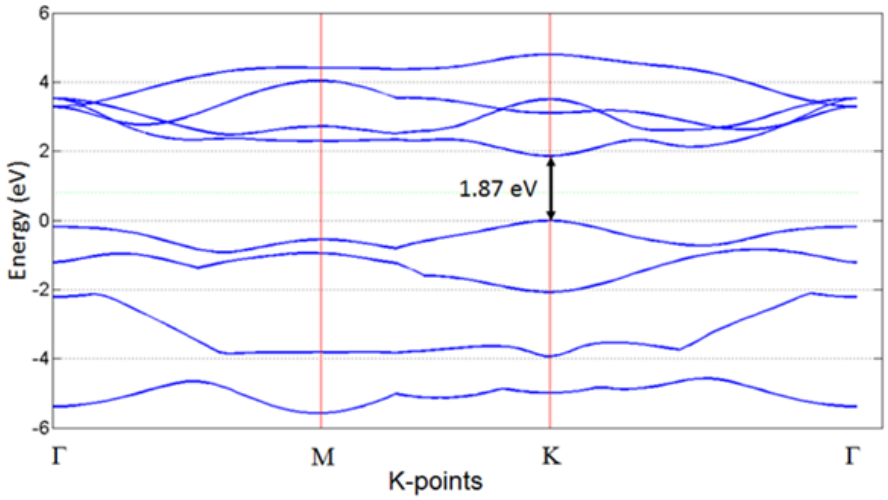

(B) Tungsten Sulfo-Selenide (WSeS)

Figure 31. Band Structure of tungsten-based TMDCs.

5.3.2 Dipole Moment of Hybrid Tungsten-based TMDCs

Pure TMDCs, in general, have no dipole moment due to symmetrical molecular structures and corresponding symmetric charge distributions in their structures. The dipole moments of WS_2 and WSe_2 have been confirmed to be zero from our DFT calculations; they have the same chalcogen atoms located symmetrically on both sides of the tungsten atoms. Any localized charge density is neutralized by the structural symmetry of the material.

Starting from pure WS_2, the dipole moment of the hybrid TMDC alloys was found to increase linearly with increasing Se concentration from 0% to 50% because of a break in the symmetrical molecular structure and appearance of asymmetrical electronic charge distributions. For Se concentrations above 50%, the dipole moment of the alloys decreased with further increase of Se concentration due to reappearance of symmetric atomic positions and charge distribution. Among the alloys, tungsten sulfo-selenide (WSeS) was found to have the highest dipole moment (0.27 D per molecule) since it has the most asymmetrical structure with only S atoms on one side of W atoms, and only Se atoms on the other side of W atoms. The dipole moments of the hybrid and pure TMDCs are summarized in Table 19.

Table 19. Dipole Moments of TMDC Alloys [$WSe_{2X}S_{2(1-X)}$].

Selenium Concentration [X]	Dipole Moment [D]
0	0.0
0.125	0.07
0.25	0.14
0.375	0.21
0.5	0.27
0.625	0.21
0.75	0.14
0.875	0.07
1	0.0

1 D (Debye) = $3.33564*10^{-30}$ C.m

The charge distribution of the intermediate alloy, WSeS, through vertical sections of the material is shown in Figure 32. It can be seen in Figure 32(A) that there is an asymmetrical distribution of the electronic charge on either side of the tungsten atom because of the presence of

different kinds of chalcogen atoms on the top and bottom of the material layer. The charge distribution is different for the individual S and Se atoms in the hybrid alloys, which breaks the charge distribution symmetry in the structures and leads to the formation of significant dipole moments in the materials.

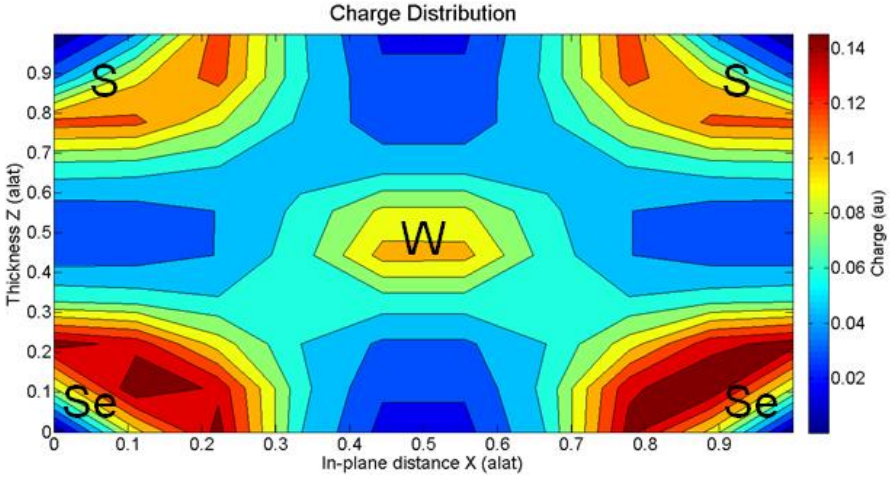

(A) Vertical section through chalcogen atoms

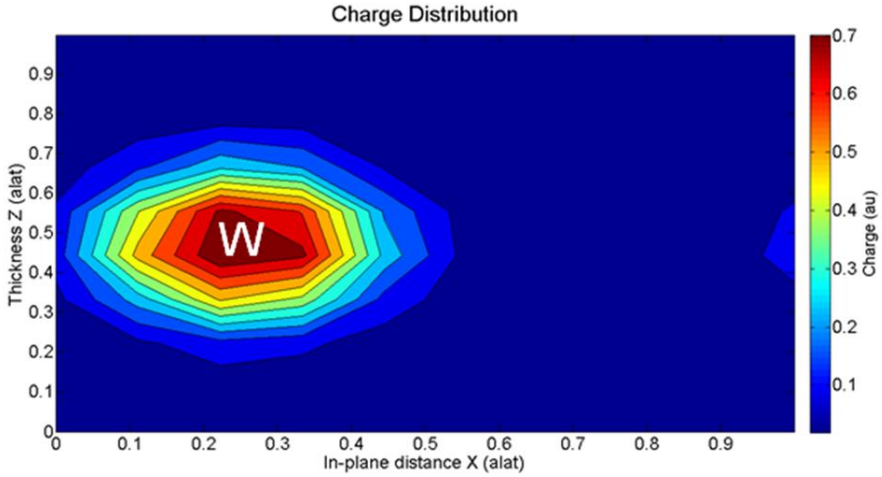

(B) Vertical section through tungsten atom

Figure 32. Charge Distribution in Tungsten Sulfo-Selenide (WSeS).

5.3.3 Electronic Properties of Tungsten Trioxide (WO_3)

The electronic band structure of WO_3 was obtained by DFT calculations together with GW corrections on Quantum ESPRESSO. WO_3 was found to be an indirect bandgap material exhibiting a bandgap of 1.86 eV with direct transition starting around 2.72 eV, as shown in Figure 33. The bandgap of WO_3 is similar to a typical wide bandgap semiconductor, which makes it a strong candidate for use in variety of electronic and photonic applications. Our results are consistent with established experimental results for the electronic properties of WO_3 [171].

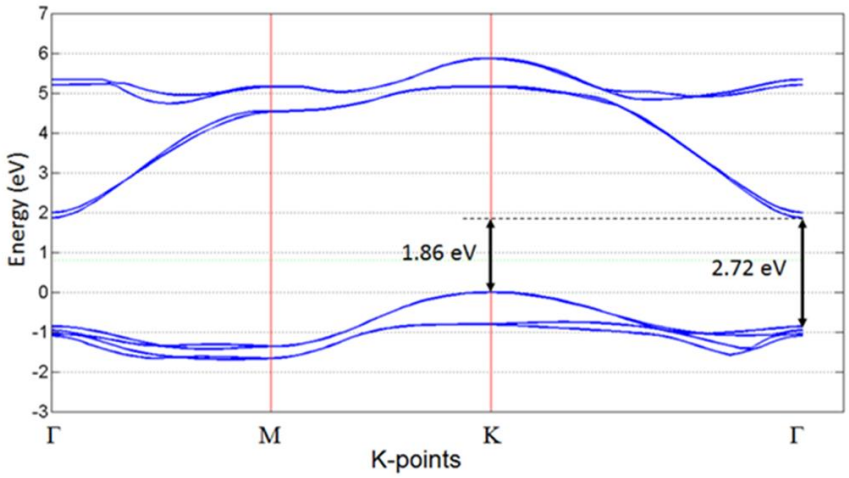

Figure 33. Band Structure of Tungsten Trioxide (WO_3).

The band structure shows an interesting feature typical of most TMDCs; both indirect and direct optical transitions can occur in this material depending on the energy of the incoming photon in the incident radiation. The electronic dispersion determines the relative location of the CBMs and VBMs, which correspond directly to the strength of the electronic transitions. Subsequently, the regions where strong photon-electron interactions take place can be understood and an appropriate device-level structure can be designed.

The density of states of WO_3 was calculated by DFT post-processing simulations using the results of the band structure calculations. The density of states of WO_3 is shown in Figure 34; it gives us an in-depth understanding of the electron distribution in the valence bands and the available states in the conduction bands. It can be observed that there is distinct energy gap of 1.86 eV which corresponds to the bandgap of the material.

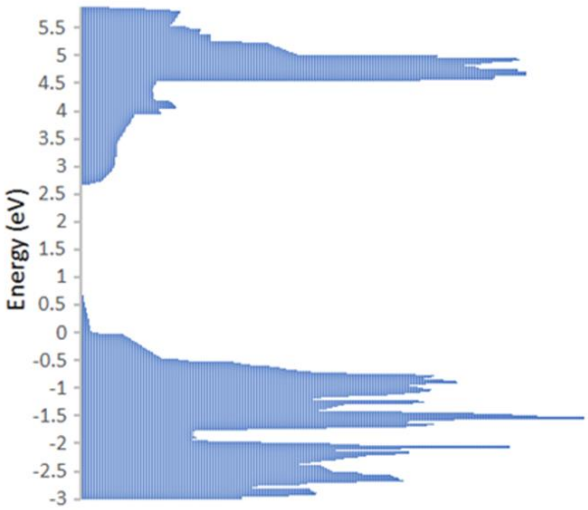

Figure 34. Density of States of Tungsten Trioxide (WO_3).

If we look at the top of the valence band over an energy range of around 0.8 eV, we can see that there are very low number of states where electrons can reside; these states are also known as pseudo-gap states. But for energies just lower than this range, there are a large number of electronic states which correspond to higher concentrations of electrons. This shows that although indirect transitions of electrons are preferred because of energy considerations, direct transitions are also very favorable in this material for higher concentrations of high energy photons as there are much more electrons available at the direct transition energy of around 2.7 eV in the electronic band structure. These results show that WO_3 is a very promising candidate for implementation as a wide bandgap semiconductor in various electronic and photonic applications.

5.4 Outlook and Conclusion

In this work, we have developed a DFT-based model to calculate electronic properties of hybrid TMDC alloys and oxides based on tungsten. Our methodology and simulation techniques have been validated against experimentally fabricated and characterized materials. The electronic band structure and bandgap of hybrid tungsten-based TMDC alloys containing both sulfur and selenium atoms were calculated and analyzed for electronic and photonic applications. Our results show that it is possible to engineer a hybrid material which can target a range of bandgap values suitable for a particular desired application, such as a photovoltaic cell.

If we consider tungsten-based TMDCs containing sulfur and selenium, it is possible to obtain a hybrid material which can have any desirable direct bandgap in the range 1.67-2.15 eV, and also exhibit the favorable electronic and optical properties of semiconducting TMDCs. Recent studies have shown that is possible to experimentally fabricate hybrid TMDC alloys based on molybdenum [37]. This unique feature of bandgap tunability in hybrid TMDCs can be extended for other TMDC alloys to obtain hybrid materials with any customizable bandgap over a wider energy range. This has the potential to open up new possibilities in fabrication and manufacture of tunable bandgap semiconductors and materials engineered for desired target applications.

The significant dipole moments of the hybrid TMDCs open up further possibilities to explore novel applications in nanoelectronics. Recent studies have shown that dipole-dipole interactions between molecules with dipole moments leads to the formation of dark states in the conduction band which can suppress radiative recombination. This mechanism of dark state protection can lead to an increase in the efficiency of photovoltaic systems. In the next chapter, we have investigated dark state protection due to dipole-dipole interactions in a photovoltaic model based on hybrid TMDCs for increasing the photovoltaic efficiency with a realistic material model to facilitate experimental realization.

Transition metal oxides have strong potential as wide bandgap semiconductors in photovoltaic applications. These materials are sturdy, resilient and resistant to environmental degradation. WO_3 is a very promising photovoltaic material. It has good absorption of high energy photons; it can be deposited on a wide variety of materials; and it is compatible for incorporation with many semiconductor devices. The electronic properties of WO_3 show that this material is a promising candidate for use as a wide bandgap semiconductor. Transition metal oxides are known to exhibit good absorptivity of high energy photons [171]. WO_3 can be implemented in device-level designs for a variety of electronic and photonic applications. It can be implemented in multi-junction solar cells in conjunction with existing photovoltaic materials and technology; WO_3 would allow better absorption of high energy photons and lead to higher efficiencies. It can be implemented in tandem with silicon and TMDC-based solar cells to obtain higher efficiencies due to incorporation of WO_3 as a wide bandgap photovoltaic material. WO_3 can be deposited favorably on a variety of materials, including silicon and other TMDCs, which makes it easy to fabricate and incorporate this material with existing photovoltaic systems.

6. CURRENT ENHANCEMENT THROUGH DARK STATE PROTECTION

6.1 Background

Recent studies [61]–[65] have investigated dark states created by dipole-dipole interaction between molecular exciton states in chromophore complexes, which can increase the photocell efficiency by protecting the excitation from radiative recombination [66]–[68]. Such interactions and the formation of stable bright and dark states are widely observed phenomena in experimental studies of pigment-protein complexes in photosynthesis and have been associated with the very high exciton capture efficiency in such processes. Although these studies point to a promising design principle for artificial photocells, they are quite limited to elementary models consisting of few interacting chromophore centers, and the dark state protection mechanism has not been applied to a specific material-based photovoltaic model. Therefore, it is the goal of the current study to investigate the possibility of creating dark states in a realistic material to enable dark state protection and increase photocell efficiency by suppressing radiative recombination with a realistic material model to facilitate experimental realization.

In this work, we have used a photovoltaic model based on TMDC materials to demonstrate the dark state protection mechanism's ability to enhance the photocurrent, thus getting closer to an actual material design to overcome the Shockley-Queisser limit. Our primary focus is on suppressing radiative recombination. We have investigated an ideal model where losses occur primarily through recombination from the excited state; losses from the dark state, as well as other losses, are considered to be negligible. For sufficiently high-quality materials, non-radiative loss is much smaller than radiative loss. Additionally, the Shockley-Queisser Limit is derived by considering the non-radiative loss preventable, while treating radiative losses as unavoidable, which is thermodynamically required for a two-level system without dark state protection [172].

This work has been presented in *2019 IEEE 46th Photovoltaic Specialists Conference (PVSC)*, pp. 0772-0776. IEEE, 2019.

It has also been published in *Advanced Functional Materials*, March 2021.

A donor-acceptor solar cell has been modeled composed of pure tungsten diselenide (WSe_2) as the acceptor material and a TMDC alloy, tungsten sulfo-selenide (WSeS), as the donor material, in analogy with a heterojunction solar cell. For the donor, two layers of WSeS are placed one on top of the other and the dipole-dipole interaction between the two layers splits the conduction band into a bright band and a dark band. The dark band can then enable the dark state protection mechanism and enhance the photocurrent generated. WSeS has a large permanent dipole moment, whereas WSe_2 does not have any permanent dipole moment, thus the donor-acceptor coupling is a dipole-induced dipole interaction.

It should be mentioned that a similar mechanism can also be theoretically observed in bulk semiconductors which have an indirect bandgap together with possible direct transition of excitons of comparable energies. In such a material, an electron can be excited by incident photons to the conduction band at the direct transition point. The excited electrons can then be transported to the lower energy valleys, corresponding to an indirect bandgap, by thermalization and phonon-assisted transfer. If the impact of phonons at this state can be suppressed, then it would inhibit decay of the electrons through indirect radiative transitions. Such a state, under ideal operating conditions including very low temperature, could also be regarded as a dark state in the bulk material.

But there are major challenges in realizing such dark states in bulk material systems, particularly at room temperature. Bulk materials have broad phonon spectrum, which limits the effectiveness of protecting the electrons in these dark states. It is very complicated to create a scenario where electrons can be transported to the lower energy valleys with phonon-assisted transfer, and at a same time phononic effects are suppressed at these valleys to prevent radiative decay of the electrons. That is why it is difficult to fully suppress indirect transition of electrons in bulk materials at room temperature. By contrast, ultra-thin 2D material systems are much more effective than bulk materials in suppressing the effect of phonons and controlling radiative recombination processes.

Our numerical model demonstrates the first application of the dark state protection mechanism to a material based photovoltaic system with a photon current enhancement of up to 35%. We have also calculated the carrier and energy dynamics, to understand all the possible energy losses in our photovoltaic model assuming perfect dark state protection. Using this

information, we have made a preliminary estimate of the maximum possible efficiency of a photovoltaic system exhibiting dark state protection. Our results show that it is possible to design a system with an ideal energy conversion efficiency exceeding the Shockley-Queisser limit.

The electronic properties of WSe_2 and WSeS, namely band structure with corresponding bandgaps and dipole moments were taken from the results presented in Chapter 5. The exciton transfer dynamics were calculated by a model based on Pauli master equations [61], [62] and the photocurrent was calculated by the standard model for photocells [63], [66], [67].

6.2 Theory and Methods

6.2.1 Donor-Acceptor Photovoltaic Model

We have used a donor-acceptor photovoltaic model composed of TMDC materials (Figure 35). The material structure model is shown in Figure 35(A). We have modeled our photovoltaic system based on a two-layer single junction heterojunction solar cell, where the top layer is the photon-absorbing layer, described as the donor layer, and the bottom layer is the current extraction layer, described as the acceptor.

The energy diagrams and photovoltaic dynamical models are shown in Figure 35(B) and Figure 35(C). Figure 35(B) shows the standard donor-acceptor model without dark state protection. A standard donor-acceptor model is a four-level system where electrons in the donor are initially in the ground state g. The cycle begins with the absorption of photons, leading to generation of excitons in the excited state e with the γ_R process. The excitation can then be transferred to the acceptor through electronic coupling and emission of phonons by the γ_C process. The γ_R process is reversible which leads to radiative recombination loss; excitons can fall back to the ground state due to radiative recombination. In the acceptor, excitons in the excited state α decay to the ground state β, where the output current is determined by the decay rate between levels α and β with the Γ process. The cycle is completed by the decay of excitons from the β state in the acceptor to the ground state g in the donor.

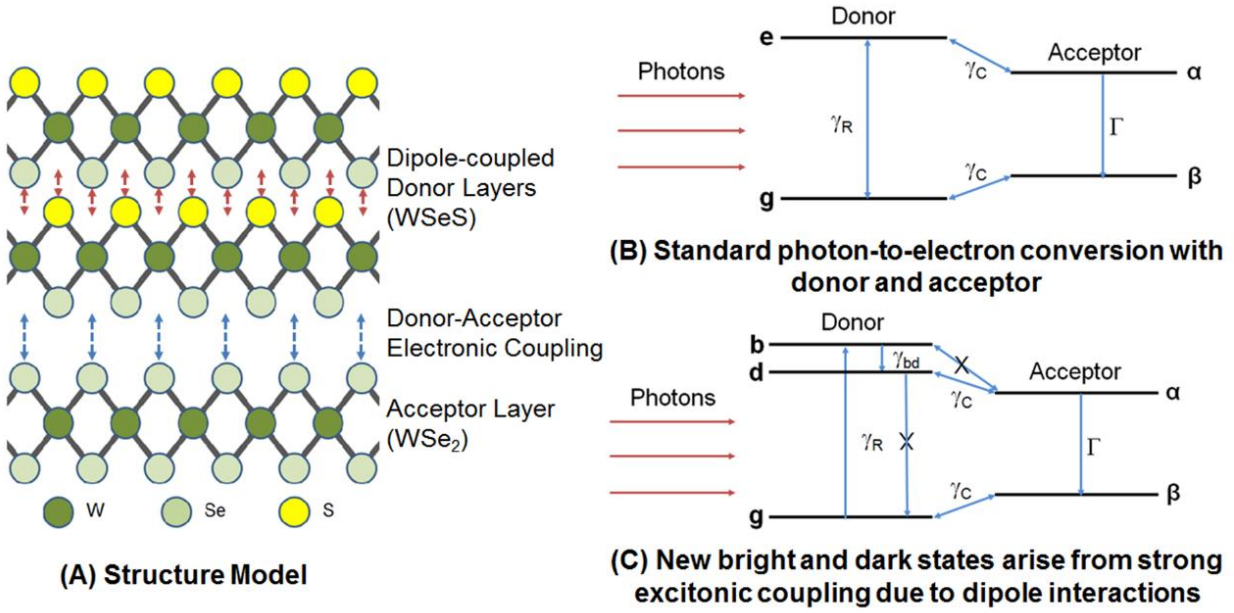

Figure 35. Donor-Acceptor Photovoltaic Model: (A) Structure Model; (B) Standard photon-to-electron conversion with donor and acceptor; (C) New bright and dark states arise from strong excitonic coupling due to dipole interactions.

Figure 35(C) shows the improved model with dark state protection. The new additional feature of our model is the formation of new optically excitable states through strong excitonic coupling between the donor layers, as shown in Figure 35(C). The formation of stable delocalized excited states arising from dipole-dipole interactions leads to a splitting of the conduction band in the donor with the formation of a bright state b and a dark state d. Virtually all photon absorption and emission take place through the bright state. In this model, the initial absorption of photons leads to excitation on the bright state with the γ_R process. The thermal relaxation process γ_{bd} brings the excitations from the bright state b into the dark state d where radiative recombination is forbidden. The decay of excitations from b to d by the γ_{bd} process is a very fast mechanism; it is much faster than any other optical or transfer process, such as γ_R and γ_C. Since radiative recombination cannot occur through d, photon re-emission is suppressed, and fewer excitons are lost through recombination before getting transferred to the acceptor. The excitation is then transferred from d to α by the γ_C process. The output photocurrent is determined by the Γ process from α to β. The cycle is completed by the decay of excitons from the β state in the

acceptor to the ground state *g* in the donor. The dark state protection from recombination leads to an increase in the number of excitons available in the acceptor, and hence, gives a higher photocurrent in the solar cell. The overall dynamics is represented by Pauli master equations whose details can be found section 6.2.3.

The bright and the dark states form when there is coupling between two identical exciton states. In terms of a 2 by 2 Hamiltonian $H = \begin{pmatrix} E & J \\ J & E \end{pmatrix}$, the diagonal elements are the energy of the exciton states, and the off-diagonal elements are the coupling strength. Diagonalizing this Hamiltonian yields two eigenstates with one symmetric state (the bright state) and one anti-symmetric state (the dark state). The bright state is optically active, while the dark state is optically inactive. In this work, we have used the same principle and theory as in previous studies [61]–[68] and implemented them in an extended system where the donors and acceptors are 2D sheets instead of isolated molecules. As shown in Figure 35, if we consider each sheet of the double-sheet structure of the donor as a collective excitation state, then the two sheet states are coupled to each other through dipole-dipole interactions between the molecules of the sheets. Then the problem reduces to the 2x2 Hamiltonian given above, where now *E* is the energy of a single donor sheet, and *J* is the collective coupling strength between two sheets. Consequently, by this design we have created the bright-state/dark-state split on the TMDC sheets under the same principle established in the previous studies. In our calculations, we have used single unit cells of the donor and acceptor molecules to model the excitonic interactions, as in recent studies. We also used periodic boundary conditions in our calculations to account for 2D sheets of the donor and acceptor materials, so that our results are consistent for the extended system presented here.

Any exciton generated with energy much higher than the bandgap energy will quickly undergo non-radiative (phononic) decay within the band, and then settle at the bottom of the conduction band. This phononic process is usually 1000 times faster than any optical process. In this regard, all excitons generated by photons with energies higher than the bandgap thermalize from the higher energy states to the band edge before any other process can take place. Thus, it is safe to assume that in our model, all excitons start within approximately the thermal energy kT from the bottom of the conduction band before any charge migration and harvesting can happen.

We have assumed that the donor-acceptor excitation transfer rate constant in our model is greater than or equal to the excitation rate constant from ground to the donor. The excitation is transferred to the acceptor fast enough to ensure the donor is never saturated; there will not be a scenario where there would be excess carrier accumulation in the donor and absorption of photon would stop due to saturation. Excess carriers are removed from the donor dark state by quickly transferring the excitation to the acceptor, and then to the ground, thereby completing the cycle.

We have used a donor-acceptor photovoltaic model composed of pure and hybrid TMDC materials (Figure 35). There are a couple of fundamental requirements which have to be taken into account for the choice of donor and acceptor materials. Firstly, the donor should have a higher bandgap than the acceptor. This is to ensure that the band alignment and energy dynamics are consistent with the donor-acceptor model and we do not have a scenario where additional energy is required to transfer the excitons from the donor to the acceptor. Secondly, the donor material should have a significant dipole. This is to ensure that there are strong dipole-dipole interactions between the donor molecules which lead to the formation of distinct, stable bright and dark states. In addition, it is preferable to have materials from the same family with similar molecular structures and comparable work functions. This has the potential benefit of easier fabrication and experimental demonstration.

The material structure model is shown in Figure 35(A): WSeS with a bandgap of 1.87 eV was chosen as the donor in our system; WSe_2 with a bandgap of 1.67 eV was chosen as the acceptor, since its lower bandgap favors the band alignment and energy dynamics of our model. Pure TMDCs have no dipole moment. But, as described in Chapter 5, hybrid alloys of TMDCs exhibit significant dipole moments. It was found that, among the materials in the family of tungsten-based hybrid TMDC alloys, WSeS has the maximum dipole moment. So, this compound was chosen as the donor material in our device.

The donor consists of two layers of WSeS arranged one on top of the other. There is strong dipole-dipole coupling between the two donor layers because of the large permanent dipole moment in each layer, and consequently the conduction band splits into a bright band and a dark band. The induced polarization in the acceptor layer was calculated with the electric field from the donor layers. The donor-acceptor coupling energy (γ_C) was calculated from the dipole-induced

dipole interaction energy between the WSeS layers and the WSe_2 layer, as described in section 6.2.2. Radiative lifetimes of excitons in TMDCs are around 5-17 ps [173], [174], corresponding to a recombination rate (γ_R) of 40-130 μeV. We have performed simulations of our model for three different values of γ_R (80 μeV, 100 μeV, 120 μeV) to account for the different radiative recombination rates. The exciton generation rate in our model is simulated by a hot photon bath at 5800K to model the solar radiation.

6.2.2 Donor-Acceptor Coupling Energy

In our donor-acceptor photovoltaic model, the donor consists of two layers of WSeS with significant dipole moments arranged one on top of the other, while the acceptor is a single layer of WSe_2 with zero dipole moment. The electric field due to the dipole moment in the donor layers was calculated by numerical methods for extended sheets of the donor layers. The induced polarization in the acceptor layer was calculated from the electric field from the donor layers, using Quantum ESPRESSO [84]. The donor-acceptor coupling energy (γ_C) and the corresponding exciton transfer rate was calculated from the dipole-induced dipole interaction energy between the WSeS layers and the WSe_2 layer. The donor layers exhibit strong dipole-dipole interaction between the individual layers.

$$U_{int} = -\frac{2\mu_1\mu_2}{4\pi\varepsilon_0 d^3}$$

where,
μ_1 and μ_2 – dipole moments of donor layers, and
d – spacing between the donor layers.

The donor-acceptor interaction is a dipole-induced dipole interaction.

$$U_{int} = -\frac{\mu^2\alpha}{(4\pi\varepsilon_0)^2 d^6}$$

where,
μ - dipole moment of donor,
α - polarizability of the acceptor,
d - donor acceptor separation.

Using the above formulas for isolated systems, we used numerical methods to obtain the interaction energy for extended sheets of the donor and acceptor materials.

6.2.3 Current Enhancement due to Dark State Protection

The exciton transfer dynamics, including exciton generation from photons and corresponding output current, is represented by Pauli master equations [61], [62].

The exciton transfer dynamics illustrated in Figure 35(B) can be represented by the following Pauli master equations:

$$\begin{aligned}
\dot{\rho}_{ee} &= -\gamma_R\left[\left(1+n_h\left(E_e-E_g\right)\right)\rho_{ee}-n_h\left(E_e-E_g\right)\rho_{gg}\right] \\
&\quad -\gamma_C\left[\left(1+n_c\left(E_e-E_\alpha\right)\right)\rho_{ee}-n_c\left(E_e-E_\alpha\right)\rho_{\alpha\alpha}\right] \\
\dot{\rho}_{gg} &= \gamma_R\left[\left(1+n_h\left(E_e-E_g\right)\right)\rho_{ee}-n_h\left(E_e-E_g\right)\rho_{gg}\right] \\
&\quad +\gamma_C\left[\left(1+n_c\left(E_\beta-E_g\right)\right)\rho_{\beta\beta}-n_c\left(E_\beta-E_g\right)\rho_{gg}\right] \\
\dot{\rho}_{\alpha\alpha} &= \gamma_C\left[\left(1+n_c\left(E_e-E_\alpha\right)\right)\rho_{ee}-n_c\left(E_e-E_\alpha\right)\rho_{\alpha\alpha}\right]-\Gamma\rho_{\alpha\alpha} \\
\dot{\rho}_{\beta\beta} &= -\gamma_C\left[\left(1+n_c\left(E_\beta-E_g\right)\right)\rho_{\beta\beta}-n_c\left(E_\beta-E_g\right)\rho_{gg}\right]+\Gamma\rho_{\alpha\alpha}
\end{aligned} \tag{1}$$

and the dynamics illustrated in Figure 35(C) can be represented by:

$$\begin{aligned}
\dot{\rho}_{bb} &= -\gamma_R\left[\left(1+n_h\left(E_b-E_g\right)\right)\rho_{bb}-n_h\left(E_b-E_g\right)\rho_{gg}\right] \\
&\quad -\gamma_{bd}\left[\left(1+n_c\left(E_b-E_d\right)\right)\rho_{bb}-n_c\left(E_b-E_d\right)\rho_{dd}\right] \\
\dot{\rho}_{dd} &= \gamma_{bd}\left[\left(1+n_c\left(E_b-E_d\right)\right)\rho_{bb}-n_c\left(E_b-E_d\right)\rho_{dd}\right] \\
&\quad -\gamma_C\left[\left(1+n_c\left(E_d-E_\alpha\right)\right)\rho_{dd}-n_c\left(E_d-E_\alpha\right)\rho_{\alpha\alpha}\right] \\
\dot{\rho}_{gg} &= \gamma_R\left[\left(1+n_h\left(E_b-E_g\right)\right)\rho_{bb}-n_h\left(E_b-E_g\right)\rho_{gg}\right] \\
&\quad +\gamma_C\left[\left(1+n_c\left(E_\beta-E_g\right)\right)\rho_{\beta\beta}-n_c\left(E_\beta-E_g\right)\rho_{gg}\right] \\
\dot{\rho}_{\alpha\alpha} &= \gamma_C\left[\left(1+n_c\left(E_d-E_\alpha\right)\right)\rho_{dd}-n_c\left(E_d-E_\alpha\right)\rho_{\alpha\alpha}\right]-\Gamma\rho_{\alpha\alpha} \\
\dot{\rho}_{\beta\beta} &= -\gamma_C\left[\left(1+n_c\left(E_\beta-E_g\right)\right)\rho_{\beta\beta}-n_c\left(E_\beta-E_g\right)\rho_{gg}\right]+\Gamma\rho_{\alpha\alpha}
\end{aligned} \tag{2}$$

where each ρ_{xx} is the population in the x state, the $n_h\left(E\right)$ is the optical distribution number defined by $n_h\left(E\right)=\left(e^{E/k_BT_h}-1\right)^{-1}$ with $T_h=5800K$ (temperature of the sun), and the $n_c\left(E\right)$ is the thermal distribution number defined by $n_c\left(E\right)=\left(e^{E/k_BT_c}-1\right)^{-1}$ with $T_c=300K$ (room temperature). The rates γ_R and γ_C are the radiative recombination rate and the donor-acceptor transfer rate,

respectively. The thermal relaxation rate γ_{bd} is usually very large compared to all the other decay rates involved; and here we define it to be $\gamma_{bd} = 1000\gamma_R$ in accordance with previous studies [61]–[65]. γ_{bd} is the same for both the relaxation from b to d and the reverse process, while the difference in rates is accounted for by the thermal distribution $\left(1+n_c\left(E_b - E_d\right)\right)$ for the relaxation and $n_c\left(E_b - E_d\right)$ for the reverse process. The rate Γ defines the output current as $I = \Phi e \Gamma \rho_{\alpha\alpha}$ where e here is the elementary charge and Φ is the photon flux in our system. The photon flux is the incident solar irradiance reaching the surface of the Earth absorbed by our two-layer TMDC-based donor material.

6.2.4 Maximum Efficiency with Dark State Protection

The efficiency limit of our donor-acceptor solar cell model was calculated using the carrier and energy dynamics, and the incident photons in our system were taken from the data of the AM1.5G solar spectrum [117]. For a particular bandgap of the donor, it is assumed that all the incident photons with energies higher than the bandgap are absorbed by the donor. The excited carriers in the donor are taken as relaxed to the band edge (dark state) for current extraction and the corresponding thermalization loss is taken into account. There is additional thermalization loss during the excitation transfer from donor to acceptor since the acceptor has a lower bandgap. The output energy obtained from each carrier is the bandgap of the acceptor, where the excitons decay from the excited state to the ground state, and in conjunction with the Carnot loss [43]. The range of donor material bandgaps was taken as 0.5-3 eV, with the acceptor bandgap taken to be 0.2 eV lower than that of the donor.

$$\eta = \frac{P_{OUT}}{P_{IN}} \times 100\%$$

where,
η – Efficiency (%)
P_{IN} – Total input power from AM 1.5G spectrum,
P_{OUT} – Output power obtained from across the acceptor material bandgap.

Any exciton generated with energy higher than the bandgap will quickly undergo non-radiative (phononic) decay within the band and then settle at the bottom of the conduction band.

This phononic process is usually 1000 times faster than any optical process such that it is safe to assume all excitons start in the bottom of the conduction band before any charge migration and harvesting can happen. Consequently, the voltage is always limited by the band gap.

In the quantum heat engine model widely used by Chin, Scully and others [61]–[67], voltage is calculated to be $eV = (E_\alpha - E_\beta) - kT \ln W$, where $W = \rho_{\beta\beta}/\rho_{\alpha\alpha}$, with $\rho_{\alpha\alpha}$ being the steady state population of the acceptor's excited state, $\rho_{\beta\beta}$ the steady state population of the acceptor's ground state. eV is therefore equal to the original acceptor bandgap $(E_\alpha - E_\beta)$ plus a thermodynamic correction. This makes the voltage always consistent with thermodynamics. For our system in steady state, there is no excess carrier accumulation in any of the excited states due to continuous donor-acceptor transfer of excitons; as a result, the entropy-associated reduction in voltage is very small compared to the bandgap of the acceptor.

In a standard solar cell, there are additional voltage reductions due to the Carnot loss and the angular entropy factor from photon emission [172]. The maximum power-point voltage (V_{mp}) of a solar cell with a bandgap E_G is given by the relationship involving the Carnot factor η_C and the entropic voltage loss due to the number of arrangements W:

$$V_{mp} = E_G \eta_C - \frac{k_B T_c}{e} \ln(W),$$

where the number of arrangements $W = \frac{1}{c}\frac{\Omega_c}{\Omega_h}\frac{\rho_{\beta\beta}}{\rho_{\alpha\alpha}}$, $T_c = 300\ K$ (room temperature), $T_h = 5800\ K$ (temperature of the sun) and the Carnot factor $\eta_C = 1 - T_c/T_h \approx 0.95$. The angular entropy factor is $\Delta = \frac{k_B T_c}{e} \ln\left(\frac{1}{c}\frac{\Omega_c}{\Omega_h}\right)$; it depends on the size of the solar disk (Ω_h) as viewed from the Earth, the angular radiation from the solar cell (Ω_c), and the concentration factor c (which is 1 in our case, since we are not looking at concentrated sunlight). In our model, radiative recombination and corresponding photon emission is suppressed by the dark state, preventing some entropic losses. The only significant voltage reduction remaining in our system is due to the Carnot loss, which is around 5% of the bandgap energy for optimal photovoltaic materials.

6.3 Results and Discussion

6.3.1 Enhancement of Output Photocurrent

There is strong dipole-dipole coupling between the two donor layers because of the large permanent dipole moment in each layer. This leads to a split in the conduction band into a bright band and a dark band, which was obtained by DFT calculations to be an 18 meV energy gap. The donor-acceptor coupling energy and the corresponding transfer rate γ_C was obtained using numerical methods in MATLAB; γ_C was calculated for donor-acceptor separation spacing ranging from 3 Å to 12 Å. It can be sees that the exciton transfer reduces exponentially as the donor-acceptor separation increases, as shown in Figure 36. For higher separations, there is reduction in the strength of donor-acceptor interaction which leads to a weaker coupling energy and a correspondingly lower exciton transfer rate. For the equilibrium donor-acceptor spacing of 3 Å [78], the coupling energy is 515 μeV, which decreases with increasing donor-acceptor separation to a value of around 50 μeV for 10 Å separation. For our initial simulation, we have used a radiative recombination rate (γ_R) of 100 μeV to demonstrate the fundamental benefit of current enhancement through dark state protection.

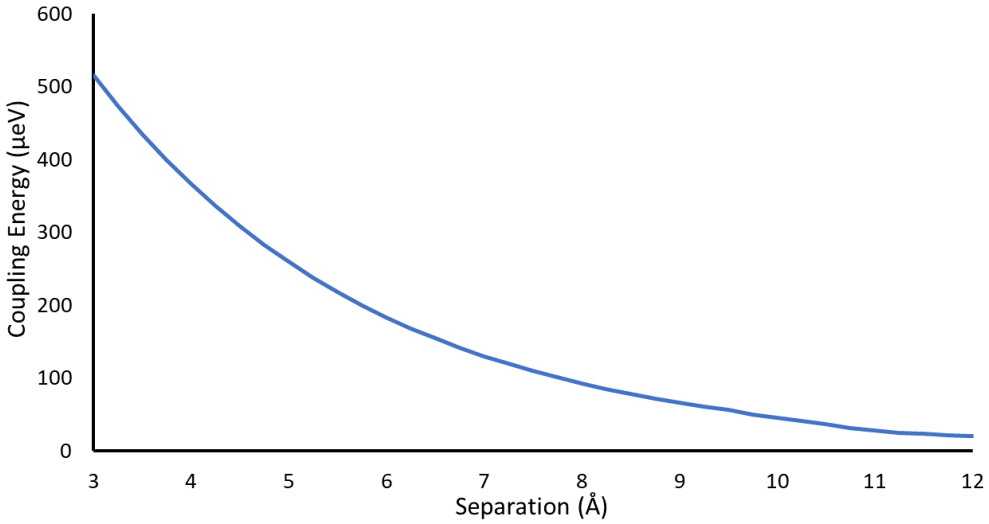

Figure 36. Donor-Acceptor Coupling Energy γ_C.

For the equilibrium separation of 3 Å and corresponding coupling energy of 515 μeV, an enhancement of 13.4% in the output photocurrent was obtained. The current of the system without dark state protection is 4.9 mA/cm^2, while introducing dark state protection increases the current to 5.56 mA/cm^2. If we look at the donor-acceptor separation scenario where the values of radiative recombination rate (γ_R) and donor-acceptor coupling energy (γ_C) are comparable to each other, we obtain a larger current enhancement of around 35% with the output photocurrent jumping from 0.99 mA/cm^2 to 1.34 mA/cm^2 due to dark state protection (for γ_C = 80 μeV). The increase in current is the result of the suppression of radiative recombination in the donor material where the photon absorption and exciton generation take place.

We have also performed some additional simulations for different values of the radiative recombination rate (γ_R). Our initial calculations took into account γ_R as 100 μeV. We have further studied cases with γ_R of 80 μeV and 120 μeV to account for the different radiative recombination rates found experimentally in TMDCs. Our results show that there is significant enhancement of the output photocurrent for the model in Figure 35(C) compared to the one in Figure 35(B) due to dark state protection. The current enhancement for different values of donor-acceptor coupling energies for each of the three cases of γ_R are summarized in Figure 37.

There is significant current enhancement of around 10-15% for the different values of γ_R for a coupling energy (γ_C) of around 500 μeV (which corresponds to equilibrium donor-acceptor separation of 3 Å). For cases where the coupling energy is smaller than or comparable to the radiative recombination rate, we can obtain current enhancements as high as 35-40% with dark state protection. This is due to the competition between the donor-acceptor transfer process γ_C and the recombination process γ_R. When the donor-acceptor transfer rate is small compared to the radiative recombination rate, significant loss can occur through the recombination process unless it is suppressed by dark state protection. By implementing dipole-dipole interactions and dark state protection in our donor-acceptor model (WSeS and WSe_2), a current enhancement of up to 35% can be obtained. The results presented in Figure 37 shows that for systems where the donor-acceptor coupling energies are small compared to the radiative recombination rates, we can obtain

a significantly high percentage enhancement of the output photocurrent by dark state protection by incorporating dipole-dipole interactions.

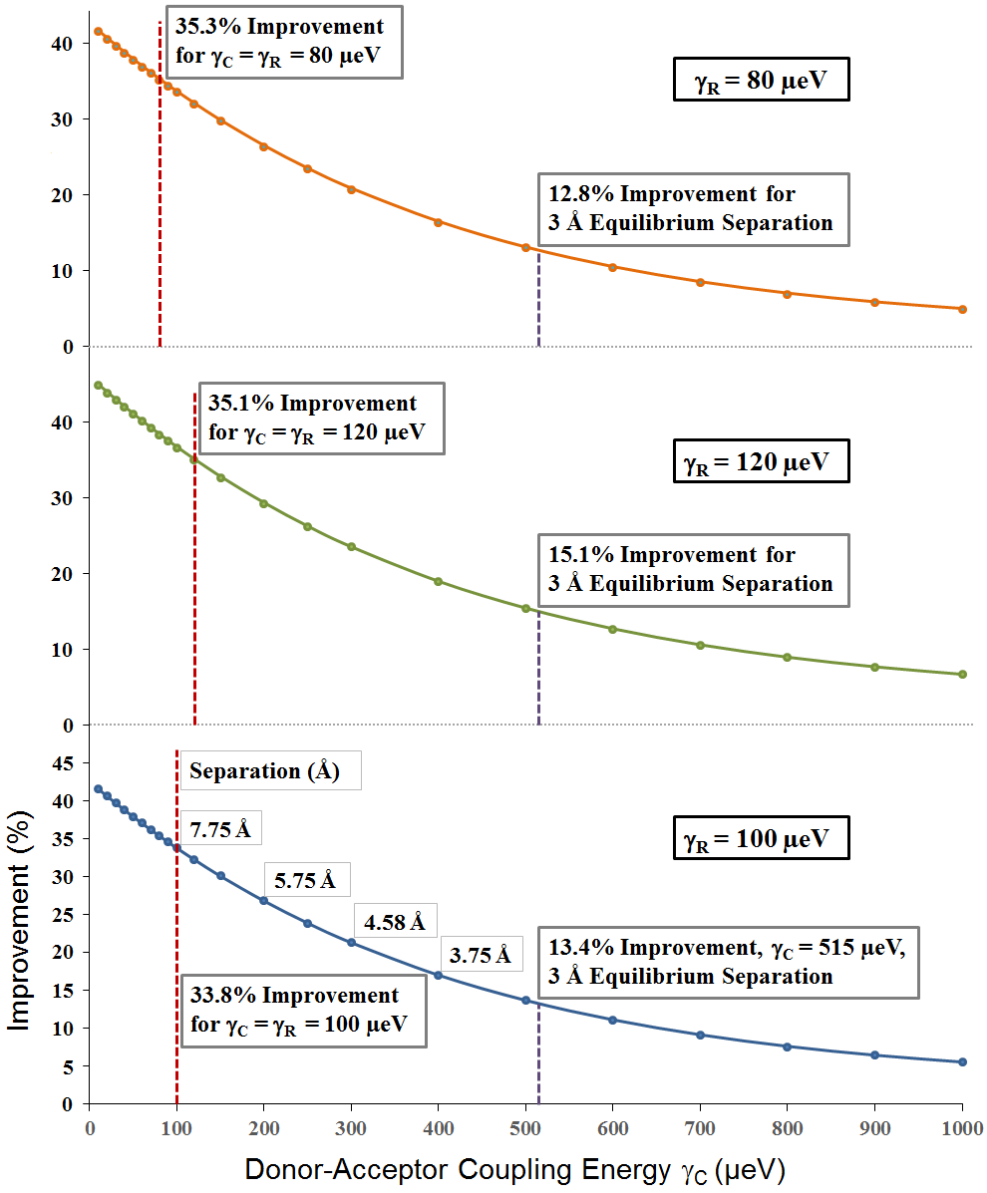

Figure 37. Improvement of output current due to dark state protection for various donor-acceptor coupling energies for $\gamma_R = 100$ μeV, and comparative performance for different values of $\gamma_R = 80$ and 120 μeV.

6.3.2 Maximum Efficiency of Photovoltaic Model with Dark State Protection

The maximum possible efficiency of a donor-acceptor solar cell model with dark state protection was calculated (Figure 38) for the AM1.5G spectrum [117] and compared with the well-known Shockley-Queisser limit for single junction solar cells [42], [43]. The calculations were carried out for donor material bandgaps from 0.5 eV to 3 eV, with the corresponding acceptor material bandgaps taken as 0.2 eV lower than the donor. It can be seen that the efficiency limit of our photovoltaic model is significantly higher than the Shockley-Queisser limit over the entire bandgap range of 0.5-3 eV.

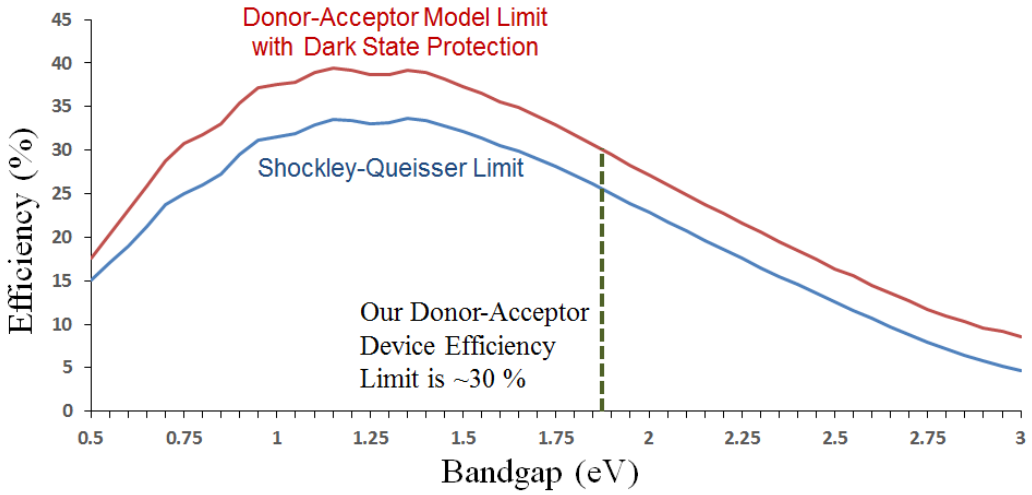

Figure 38. Efficiency limit of a donor-acceptor photovoltaic system with dark state protection.

Our efficiency limit calculation is an idealistic approach to evaluate the efficiency of a donor-acceptor model with perfect dark-state protection. It is assumed that all the incident photons with energies above the donor bandgap are absorbed and correspondingly excitons are generated, there is no radiative recombination in the donor (dark state protection is perfect), and there is no loss of excitons during the Γ process in the acceptor. We have accounted for carrier thermalization losses during the relaxation to the band edges in the donor and acceptor. For our donor material (WSeS) with a bandgap of 1.87 eV, we can get a maximum efficiency of around 30% using the donor-acceptor photovoltaic model with dark state protection under ideal conditions, compared to a maximum efficiency of around 26% as per the Shockley-Queisser limit for a semiconductor of the same bandgap 1.87 eV. In our model, we have overcome the detailed-balance

limit, but we are still within the ultimate efficiency as described by Shockley and Queisser, which is the maximum efficiency that can be achieved without radiative recombination.

The efficiency limit calculation is a purely theoretical estimation as it doesn't account for many non-idealities; dark state protection might not be perfect at room temperature or with a conduction band splitting of less than 100 meV. A major challenge in attaining our predicted efficiency is obtaining 100% photon absorption in only a few layers of the donor material. The absorption of a two-layer TMDC donor system is around 6-7% of incident photons in the incident solar spectrum (AM1.5G), which results in the low current values of around 1 to 5 mA/cm^2 in our system; this is consistent with experimental photovoltaic cells consisting of 2-3 layers of TMDC materials. These values are well below those found in commercial solar cells, which typically have short-circuit currents around 30-40 mA/cm^2. To obtain an efficiency above the Shockley-Queisser Limit, it is necessary to add enough layers so that over 95% of the above bandgap energy photons in the incident solar spectrum could be absorbed.

In addition, there could also be significant loss of carriers through recombination in the donor if the donor-acceptor coupling energy and the corresponding transfer rate is low, compared to the generation rate of excitons in the donor; this scenario would lead to an accumulation of excess carriers in the donor which are not transferred to the acceptor, and hence lost through recombination or other processes. On the other hand, if we can extract the hot carriers with energies above the band edge in the donor and efficiently transfer the high energy excitons to the acceptor, this can lead to lower thermalization losses and allow for even higher efficiencies. Although not outright conclusive, the maximum efficiency limit shown in Figure 38 gives an insight into the possible improvements that can be obtained with incorporating the dark state protection mechanism into a TMDC-based donor-acceptor photovoltaic system.

6.4 Outlook and Conclusion

We have demonstrated a TMDC-based donor-acceptor photovoltaic model, where the dark state protection mechanism is used to reduce carrier recombination and enhance photon-to-electron conversion, leading to significantly higher current output. TMDCs have already been shown to have great potential as ultra-thin photovoltaic materials in solar cells. In this work, we have explored and modeled a heterojunction-like solar cell composed of tungsten diselenide (WSe_2) as

the acceptor material and tungsten sulfo-selenide (WSeS) as the donor material. The dipole-dipole coupling between the two layers of the donor material splits the conduction band and enables the dark state protection of excitation from radiative recombination, achieving a photocurrent enhancement as high as 35% over the standard model without dark state protection. The enhancement is more significant when the donor-acceptor transfer rate is comparable to or smaller than the radiative recombination rate.

The principal model which we have presented in this work exhibits the unique feature of dark state protection in an experimentally realizable system, compared to prior work on this specific topic which focus on elementary models of hypothetical molecules. While we used experimental literature values wherever possible, we did make certain assumptions about unknowns and considered the most optimistic scenarios. However, since this phenomenon of sark state protection could still be seen as an improvement compared to a control without radiative recombination suppression, it is possible to observe this effect across a wide range of possible experimental conditions. For instance, even if non-radiative losses are present, the enhanced current due to dark state protection observed experimentally could be lower than that which we have modeled in this work, but it will still be higher than the system which does not have any dark state protection. The ideal values presented in this work provide an upper limit for the potential benefits of this approach, to help motivate further work in the field; importantly, experimental realization and measurement of dark state current enhancement does not require extraordinarily optimistic or even unusual parameter values.

As a potential device model for implementation, we propose a contact for hole collection on the WSeS side and a contact for electron collection on the WSe_2 side of appropriate work functions, similar to carrier collection mechanisms in the structure of heterojunction solar cells. Although a preliminary estimate, the efficiency limit of such a model has been calculated to potentially overcome the Shockley-Queisser limit if all photons above the bandgap energy are absorbed with perfect dark state protection, and there is no loss during carrier collection in the acceptor. This opens up possibilities for exploring new materials and device architectures for ultra-thin, ultra-efficient photovoltaic devices.

Our estimate of the maximum efficiency gives a possible future direction of this work, if dark state protection can be experimentally realized. It includes all the required physics in an ideal system, but does not include all non-idealities. The idealized assumptions highlight the fundamental limits of the system with dark state protection and present an upper-bound limit of the maximum possible efficiency of this system.

7. SUMMARY

Transition Metal Di-Chalcogenides (TMDC) are 2D layered materials which have attracted a great deal of interest in recent years due to their promising physical and chemical properties, and potential for implementation in a variety of electronic and optical applications. We have carried out a detailed investigation of the electronic and optical properties of tungsten disulfide (WS_2) and related TMDCs. WS_2 has an optically favorable band gap for photovoltaic applications; it has significant absorptivity of photons with energies above its bandgap. It also exhibits excellent carrier transport properties, as demonstrated by typically high mobility values. Its 2D layered structure makes it possible to modify and tune its electronic properties by altering the structure with dopants. Its favorable electronic and optical properties make it a strong candidate in photovoltaics. We have explored various device models and architectures to demonstrate photovoltaic applications of WS_2 and related TMDCs, and proposed new designs which have the potential to overcome many existing limitations of photovoltaic performance.

In Chapter 2, we developed a DFT-based model to calculate key materials properties for various structures of WS_2, which have been validated against experimentally fabricated and characterized materials. It is essential to study the fundamental electronic properties in order to progress to device level applications and understand the benefits and limitations of device level integration in new and existing technology. The most fundamental property is the electronic band structure, which gives us a lot of vital information such as absorptivity of incident photons and availability of excited carriers. The electronic and optical properties of monolayer, bilayer and bulk WS_2 were calculated and analyzed for implementation in photovoltaic systems. The study of these properties allows us to progress towards understanding and investigating device-level applications of WS_2.

Bulk WS_2 was found to be an indirect bandgap material having a bandgap of 1.29 eV, with direct transition starting around 2.2 eV. Bilayer WS_2 was found to be an indirect bandgap material having a bandgap of 1.64 eV, with direct transition starting around 2.13 eV. Monolayer WS_2 was found to be a direct bandgap material exhibiting a bandgap of 2.15 eV. The bandgaps of the different structures of WS_2 are summarized in Figure 39. The electronic band structure and

bandgap of monolayer, bilayer and bulk WS_2 are similar to a typical photovoltaic material, which makes them very good candidates for use in solar cells.

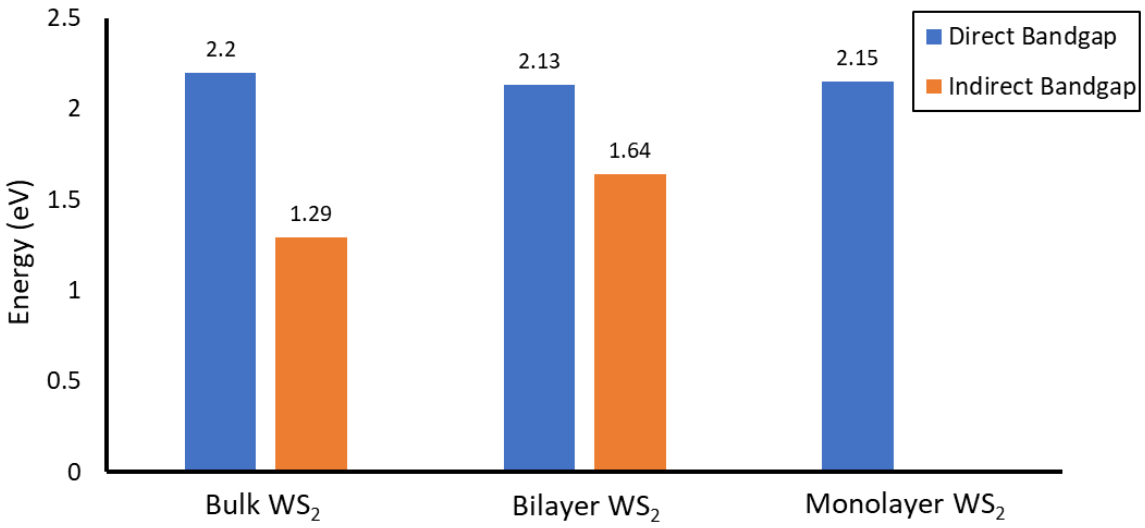

Figure 39. Summary of bandgaps of WS_2

The values of α obtained for the different structures of WS_2 show that there is significant absorption of incoming photons with energies above the bandgap energy. The absorption profiles of WS_2 show that this material has good absorption of photons within the energy range of the incident solar radiation on the surface of Earth and outer space environments. This enables implementation of WS_2 as a light absorbing material in a solar cell. These results show WS_2 has very favorable electronic and optical properties for photovoltaic applications, along with the natural advantages of light weight, flexibility, and earth abundance of most TMDCs.

In Chapter 3, we have used the calculated electronic and optical properties of WS_2 to progress towards understanding and investigating device-level applications of this unique material in a photovoltaic system. Bulk WS_2 was used as the starting material for designing a solar cell device model. Using this as the baseline, monolayer WS_2 and amorphous silicon (a-Si) were added to improve the performance. A p-n junction solar cell was modeled and simulated using monolayer WS_2, bulk WS_2 and a-Si to obtain a structure similar to HIT (Heterojunction with Intrinsic Thin Layer) solar cells.

Initially, our baseline solar cell design using only bulk WS_2 gave reasonable performance with an optimal efficiency of around 14%. After making some modifications to our model, such as introducing monolayer WS_2 and a-Si, which improve the electronic band structure and optical performance, the overall efficiency of the optimal solar cell model increased significantly to over 23%, which is comparable to the performance of many commercial single-junction solar cells. The maximum device efficiency which we obtained from best performing photovoltaic model was 23.3%, with V_{OC} of 0.84 V and J_{SC} of 33.5 mA/cm^2.

The primary device modeling and simulations which we have developed in this work are based on the terrestrial solar radiation on the surface of the Earth (AM1.5G spectrum). In addition, we have also investigated potential implementations of our proposed WS_2-based solar cell model in space photovoltaic applications, where this material has the potential to outperform existing technology. We simulated our solar cell models under the space solar radiation (AM0 spectrum) to gain better understanding and insight into the performance of our proposed device for space photovoltaic applications.

TMDCs have been demonstrated to exhibit resistance to radiation-induced damage, and are very good candidates for space photovoltaic applications. Our solar cell design shows that it is possible to obtain efficiencies above 20% with the space solar spectrum, but a major issue encountered here is the total thickness of the active layers in our device and possible radiation-induced degradation. It is essential to design an ultra-thin device with a maximum thickness of around a few hundred nanometers to minimize damage from radiation. The reduced absorption in thin WS_2 layers of our solar cell can be compensated by incorporation of additional features such as light trapping structures and anti-reflection coating layers to enhance the incident radiation absorption and obtain a higher device performance with an ultra-thin device model.

In Chapter 4, we developed a photovoltaic system based on WS_2 for proposed implementation in space photovoltaic applications. We have demonstrated that our photovoltaic model with thickness of 200 nm exhibits efficiencies around 14.3-15.8% over the temperature range of satellite orbits (313-343K). We have incorporated a light trapping structure and an anti-reflection coating layer in our solar cell model which collectively increase the absorption of the incident solar radiation, and lead to better performance of the device with higher current; we have

proposed a realistic and experimentally viable device structure which can be competitive and comparable to existing solar cells for space photovoltaics.

We have used a 1D silver grating light trapping structure in our photovoltaic model to increase the optical path length of light inside the solar cell. The efficiencies of our solar cell increased to 18.5-20.4% over the temperature range 313-343K as a result of absorption enhancement from light trapping. In addition to the light trapping structure, we have also added an appropriate dielectric material layer in our photovoltaic model to function as an anti-reflection coating, in order to reduce the surface reflection from our solar cell and enhance the absorption even further. The efficiencies of our final solar cell model increased to 21.4-23.6% over the temperature range 313-343K because of the effect of the anti-reflection coating layer, which is comparable to the performance of many commercial single-junction solar cells used in space applications. These results show that a solar cell based on WS_2 have very favorable performance features and properties for use in space photovoltaics, along with the natural advantages of light weight, flexibility, earth abundance and resilience.

The 2D layered structure of TMDCs makes it possible to modify and tune their electronic properties by doping with other atoms and manufacturing hybrid alloys. It is possible to obtain alloys of TMDCs by altering their composition to contain more than one kind of chalcogen atoms, leading to the formation of hybrid TMDCs with tunable electronic and optical properties. In Chapter 5, we have developed a DFT-based model to calculate electronic properties of hybrid TMDC alloys and oxides based on tungsten. We have explored monolayers of tungsten-based TMDC alloys containing sulfur and selenium, whose properties are intermediate of pure tungsten dilsulfide (WS_2) and pure tungsten diselenide (WSe_2) with tunable direct bandgaps dependent on the sulfur and selenium concentrations.

The electronic band structure and bandgap of hybrid tungsten-based TMDC alloys containing both sulfur and selenium atoms were calculated and analyzed for electronic and photonic applications in Chapter 5. Our results show that it is possible to engineer a hybrid tungsten-based TMDC alloy which can have any desirable direct bandgap in the range 1.67-2.15 eV for a particular target application, and also exhibit the favorable electronic and optical

properties of semiconducting TMDCs. The TMDC alloys exhibit tunability of electronic properties and other unique features which allow for a variety of novel applications.

Transition metal oxides are very versatile, sturdy, and resistant to atmospheric extremities; they are known to exhibit good absorptivity of high energy photons. The electronic band structure, bandgap and density of states were calculated to study the unique features of this material and explore possible electronic and optical applications. The electronic properties of tungsten trioxide show that this material is a promising candidate for implementation as a wide-bandgap semiconductor. It can be incorporated in multi-junction solar cells in conjunction with existing photovoltaic materials and technology. It can also be implemented in tandem with silicon and TMDC-based solar cells to obtain higher efficiencies due to effect of WO_3 as a wide bandgap photovoltaic material.

The significant dipole moments of the hybrid TMDCs open up further possibilities to explore novel applications in nanoelectronics. Recent studies have shown that dipole-dipole interactions between molecules with dipole moments leads to the formation of dark states in the conduction band which can suppress radiative recombination. This mechanism of dark state protection can lead to an increase in the efficiency of photovoltaic systems.

In Chapter 6, we have investigated dark state protection due to dipole-dipole interactions in a photovoltaic model based on hybrid TMDCs for increasing the photovoltaic efficiency with a realistic material model to facilitate experimental realization.

We have modeled a donor-acceptor solar cell composed of pure tungsten diselenide (WSe_2) as the acceptor material and a TMDC alloy, tungsten sulfo-selenide (WSeS), as the donor material, in analogy with a heterojunction solar cell. The dipole-dipole coupling between the two layers of the donor material splits the conduction band into a bright band and a dark band and enables the dark state protection of excitation from radiative recombination; this leads to a corresponding increase in the output photocurrent. Our numerical model demonstrates the first application of the dark state protection mechanism to a material based photovoltaic system with a photon current enhancement of up to 35%. We have also made a preliminary estimate of the maximum possible efficiency of our photovoltaic system after taking into account all the possible energy losses in our model assuming perfect dark state protection. Our results show that it is possible to design a system

with an ideal energy conversion efficiency exceeding the Shockley-Queisser limit, if dark state protection can be experimentally realized.

The research projects and results presented in this dissertation give a promising insight into the advancements and potential breakthroughs that can be achieved in nanoelectronics and photonics using ultra-thin TMDCs. Over the next few years, there would be great value in establishing collaboration with research groups focused on experimental work to fabricate, characterize, and test the photovoltaic devices proposed in the research described in this dissertation. Experimental observations and verifications of TMDC-based device models would lead the way for commercial development of nanoelectronic and photonic devices based on ultra-thin 2D TMDCs. In addition, similar investigations can also be carried out with other relatively unexplored materials using the same theoretical techniques and simulations as described in the research projects. This would have a strong potential for exploration of new materials for unique and novel applications in a variety of electronic and optical devices.

REFERENCES

[1] Q. H. Wang, K. Kalantar-Zadeh, A. Kis, J. N. Coleman, and M. S. Strano, "Electronics and optoelectronics of two-dimensional transition metal dichalcogenides," *Nature Nanotechnology*, vol. 7, no. 11. 2012, doi: 10.1038/nnano.2012.193.

[2] S. M. Auerbach, K. A. Carrado, and P. K. Dutta, *Handbook of Layered Materials*. 2004.

[3] J. P. Wilcoxon, P. P. Newcomer, and G. A. Samara, "Synthesis and optical properties of MoS2 and isomorphous nanoclusters in the quantum confinement regime," *Journal of Applied Physics*, vol. 81, no. 12, 1997, doi: 10.1063/1.365367.

[4] B. L. Abrams and J. P. Wilcoxon, "Nanosize semiconductors for photooxidation," *Critical Reviews in Solid State and Materials Sciences*, vol. 30, no. 3. 2005, doi: 10.1080/10408430500200981.

[5] K. F. Mak, C. Lee, J. Hone, J. Shan, and T. F. Heinz, "Atomically Thin MoS2: A New Direct-Gap Semiconductor," *Physical Review Letters*, vol. 105, no. 13, 2010.

[6] A. Ramasubramaniam, D. Naveh, and E. Towe, "Tunable band gaps in bilayer transition-metal dichalcogenides," *Physical Review B - Condensed Matter and Materials Physics*, vol. 84, no. 20, 2011, doi: 10.1103/PhysRevB.84.205325.

[7] R. Coehoorn, C. Haas, J. Dijkstra, C. J. F. Flipse, R. A. de Groot, and A. Wold, "Electronic structure of MoSe2, MoS2, and WSe2. I. Band-structure calculations and photoelectron spectroscopy," *Physical Review B*, vol. 35, no. 12, 1987, doi: 10.1103/PhysRevB.35.6195.

[8] B. Radisavljevic, A. Radenovic, J. Brivio, V. Giacometti, and A. Kis, "Single-layer MoS2 transistors," *Nature Nanotechnology*, vol. 6, no. 3, 2011, doi: 10.1038/nnano.2010.279.

[9] W. Zhang *et al.*, "Ultrahigh-Gain Photodetectors Based on Atomically Thin Graphene-MoS2 Heterostructures," *Scientific Reports*, vol. 4, 2015, doi: 10.1038/srep03826.

[10] A. Splendiani *et al.*, "Emerging photoluminescence in monolayer MoS2," *Nano Letters*, vol. 10, no. 4, 2010, doi: 10.1021/nl903868w.

[11] M. Bernardi, M. Palummo, and J. C. Grossman, "Extraordinary sunlight absorption and one nanometer thick photovoltaics using two-dimensional monolayer materials," *Nano Letters*, vol. 13, no. 8, 2013, doi: 10.1021/nl401544y.

[12] P. Afanasiev and C. Lorentz, "Oxidation of Nanodispersed MoS2 in Ambient Air: The Products and the Mechanistic Steps," *Journal of Physical Chemistry C*, vol. 123, no. 12, 2019, doi: 10.1021/acs.jpcc.9b01682.

[13] O. Lopez-Sanchez, D. Lembke, M. Kayci, A. Radenovic, and A. Kis, "Ultrasensitive photodetectors based on monolayer MoS2," *Nature Nanotechnology*, vol. 8, no. 7, 2013, doi: 10.1038/nnano.2013.100.

[14] P. A. Iles, "Future of photovoltaics for space applications," *Progress in Photovoltaics: Research and Applications*, vol. 8, no. 1, 2000, doi: 10.1002/(SICI)1099-159X(200001/02)8:1<39::AID-PIP304>3.0.CO;2-D.

[15] S. G. Bailey, R. Raffaelle, and K. Emery, "Space and terrestrial photovoltaics: Synergy and diversity," *Progress in Photovoltaics: Research and Applications*, vol. 10, no. 6, 2002, doi: 10.1002/pip.446.

[16] T. Vogl *et al.*, "Radiation tolerance of two-dimensional material-based devices for space applications," *Nature Communications*, vol. 10, no. 1, 2019, doi: 10.1038/s41467-019-09219-5.

[17] "Light Trapping | PVEducation." https://www.pveducation.org/pvcdrom/design-of-silicon-cells/light-trapping (accessed Sep. 29, 2019).

[18] L. Li, "Formulation and comparison of two recursive matrix algorithms for modeling layered diffraction gratings," *Journal of the Optical Society of America A*, vol. 13, no. 5, 1996, doi: 10.1364/josaa.13.001024.

[19] T. Markvart and L. Castañer, "Principles of solar cell operation," in *McEvoy's Handbook of Photovoltaics: Fundamentals and Applications*, 2018.

[20] M. A. Green and M. J. Keevers, "Optical properties of intrinsic silicon at 300K," *Progress in Photovoltaics: Research and Applications*, vol. 3, no. 3, 1995, doi: 10.1002/pip.4670030303.

[21] "Anti-Reflection Coatings | PVEducation." https://www.pveducation.org/pvcdrom/design-of-silicon-cells/anti-reflection-coatings (accessed Sep. 29, 2019).

[22] H. S. Lee *et al.*, "MoS2 Nanosheet Phototransistors with Thickness-Modulated Optical Energy Gap," *Nano Letters*, vol. 12, no. 7, Jul. 2012, doi: 10.1021/nl301485q.

[23] Y. J. Wu *et al.*, "Piezoreflectance study of near band edge excitonic-transitions of mixed-layered crystal Mo(SxSe1-x)2 solid solutions," *Journal of Applied Physics*, vol. 115, no. 22, 2014, doi: 10.1063/1.4882301.

[24] J. Z. Ou, A. F. Chrimes, Y. Wang, S. Y. Tang, M. S. Strano, and K. Kalantar-Zadeh, "Ion-driven photoluminescence modulation of quasi-two-dimensional MoS2 nanoflakes for applications in biological systems," *Nano Letters*, vol. 14, no. 2, 2014, doi: 10.1021/nl4042356.

[25] Y. Wang *et al.*, "Plasmon resonances of highly doped two-dimensional MoS2," *Nano Letters*, vol. 15, no. 2, 2015, doi: 10.1021/nl503563g.

[26] S. Mouri, Y. Miyauchi, and K. Matsuda, "Tunable photoluminescence of monolayer MoS2 via chemical doping," *Nano Letters*, vol. 13, no. 12, 2013, doi: 10.1021/nl403036h.

[27] D. O. Dumcenco, H. Kobayashi, Z. Liu, Y. S. Huang, and K. Suenaga, "Visualization and quantification of transition metal atomic mixing in Mo1-x Wx S2 single layers," *Nature Communications*, vol. 4, 2013, doi: 10.1038/ncomms2351.

[28] L. Ci *et al.*, "Atomic layers of hybridized boron nitride and graphene domains," *Nature Materials*, vol. 9, no. 5, 2010, doi: 10.1038/nmat2711.

[29] H. Liu, K. K. A. Antwi, S. Chua, and D. Chi, "Vapor-phase growth and characterization of Mo1−x Wx S2 ($0 \leq x \leq 1$) atomic layers on 2-inch sapphire substrates," *Nanoscale*, vol. 6, no. 1, 2014, doi: 10.1039/C3NR04515C.

[30] Y. Chen *et al.*, "Composition-dependent Raman modes of Mo1−x Wx S2 monolayer alloys," *Nanoscale*, vol. 6, no. 5, 2014, doi: 10.1039/C3NR05630A.

[31] Q. Feng *et al.*, "Growth of large-area 2D MoS2(1-x)Se2x semiconductor alloys," *Advanced Materials*, vol. 26, no. 17, 2014, doi: 10.1002/adma.201306095.

[32] Z. Lin *et al.*, "Facile synthesis of MoS2 and Mox W1-x S2 triangular monolayers," *APL Materials*, vol. 2, no. 9, 2014.

[33] X. Huang, Z. Zeng, and H. Zhang, "Metal dichalcogenide nanosheets: Preparation, properties and applications," *Chemical Society Reviews*, vol. 42, no. 5, 2013, doi: 10.1039/c2cs35387c.

[34] Z. Yin *et al.*, "Single-Layer MoS2 Phototransistors," *ACS Nano*, vol. 6, no. 1, Jan. 2012, doi: 10.1021/nn2024557.

[35] H. P. Komsa and A. v. Krasheninnikov, "Two-dimensional transition metal dichalcogenide alloys: Stability and electronic properties," *Journal of Physical Chemistry Letters*, vol. 3, no. 23, 2012, doi: 10.1021/jz301673x.

[36] L. Yang *et al.*, "Large-area synthesis of monolayered MoS2(1−x)Se2x with a tunable band gap and its enhanced electrochemical catalytic activity," *Nanoscale*, vol. 7, no. 23, 2015, doi: 10.1039/C5NR02652K.

[37] Y. Gong *et al.*, "Band gap engineering and layer-by-layer mapping of selenium-doped molybdenum disulfide," *Nano Letters*, vol. 14, no. 2, 2014, doi: 10.1021/nl4032296.

[38] S. Umrao, J. Jeon, S. M. Jeon, Y. J. Choi, and S. Lee, "A homogeneous atomic layer MoS2(1−x)Se2x alloy prepared by low-pressure chemical vapor deposition, and its properties," *Nanoscale*, vol. 9, no. 2, 2017, doi: 10.1039/C6NR07240B.

[39] Y. Yue, Y. Feng, J. Chen, D. Zhang, and W. Feng, "Two-dimensional large-scale bandgap-tunable monolayer MoS2(1−x)Se2x/graphene heterostructures for phototransistors," *Journal of Materials Chemistry C*, vol. 5, no. 24, 2017, doi: 10.1039/C7TC00951H.

[40] J. Bullock, A. Cuevas, T. Allen, and C. Battaglia, "Molybdenum oxide MoOx: A versatile hole contact for silicon solar cells," *Applied Physics Letters*, vol. 105, no. 23, 2014, doi: 10.1063/1.4903467.

[41] M. Bivour, J. Temmler, H. Steinkemper, and M. Hermle, "Molybdenum and tungsten oxide: High work function wide band gap contact materials for hole selective contacts of silicon solar cells," *Solar Energy Materials and Solar Cells*, vol. 142, 2015, doi: 10.1016/j.solmat.2015.05.031.

[42] W. Shockley and H. J. Queisser, "Detailed balance limit of efficiency of p-n junction solar cells," *Journal of Applied Physics*, vol. 32, no. 3, 1961, doi: 10.1063/1.1736034.

[43] L. C. Hirst and N. J. Ekins-Daukes, "Fundamental losses in solar cells," *Progress in Photovoltaics: Research and Applications*, vol. 19, no. 3, 2011, doi: 10.1002/pip.1024.

[44] M. A. Green, E. D. Dunlop, J. Hohl-Ebinger, M. Yoshita, N. Kopidakis, and A. W. Y. Ho-Baillie, "Solar cell efficiency tables (Version 55)," *Progress in Photovoltaics: Research and Applications*, vol. 28, no. 1, 2020, doi: 10.1002/pip.3228.

[45] O. D. Miller, E. Yablonovitch, and S. R. Kurtz, "Strong internal and external luminescence as solar cells approach the Shockley-Queisser limit," *IEEE Journal of Photovoltaics*, vol. 2, no. 3, 2012, doi: 10.1109/JPHOTOV.2012.2198434.

[46] M. A. Green and S. P. Bremner, "Energy conversion approaches and materials for high-efficiency photovoltaics," *Nature Materials*, vol. 16, no. 1. 2016, doi: 10.1038/nmat4676.

[47] M. C. Beard, J. M. Luther, and A. J. Nozik, "The promise and challenge of nanostructured solar cells," *Nature Nanotechnology*, vol. 9, no. 12. 2014, doi: 10.1038/nnano.2014.292.

[48] S. A. Mann, R. R. Grote, R. M. Osgood, A. Alù, and E. C. Garnett, "Opportunities and Limitations for Nanophotonic Structures to Exceed the Shockley-Queisser Limit," *ACS Nano*, vol. 10, no. 9, 2016, doi: 10.1021/acsnano.6b03950.

[49] Y. Xu, T. Gong, and J. N. Munday, "The generalized Shockley-Queisser limit for nanostructured solar cells," *Scientific Reports*, vol. 5, 2015, doi: 10.1038/srep13536.

[50] C. B. Honsberg and A. M. Barnett, "Paths to Ultra-High Efficiency (>50% Efficient) Photovoltaic Devices," *20th European Photovoltaic Solar Energy Conference*, no. June, 2005.

[51] A. Polman, M. Knight, E. C. Garnett, B. Ehrler, and W. C. Sinke, "Photovoltaic materials: Present efficiencies and future challenges," *Science*, vol. 352, no. 6283. 2016, doi: 10.1126/science.aad4424.

[52] C. H. Henry, "Limiting efficiencies of ideal single and multiple energy gap terrestrial solar cells," *Journal of Applied Physics*, vol. 51, no. 8, 1980, doi: 10.1063/1.328272.

[53] J. S. Ward *et al.*, "Techno-economic analysis of three different substrate removal and reuse strategies for III-V solar cells," *Progress in Photovoltaics: Research and Applications*, vol. 24, no. 9, 2016, doi: 10.1002/pip.2776.

[54] Z. Zhou, E. Sakr, Y. Sun, and P. Bermel, "Solar thermophotovoltaics: Reshaping the solar spectrum," *Nanophotonics*, vol. 5, no. 1. 2016, doi: 10.1515/nanoph-2016-0011.

[55] T. Trupke, M. A. Green, and P. Würfel, "Improving solar cell efficiencies by down-conversion of high-energy photons," *Journal of Applied Physics*, vol. 92, no. 3, 2002, doi: 10.1063/1.1492021.

[56] D. Knig *et al.*, "Hot carrier solar cells: Principles, materials and design," in *Physica E: Low-Dimensional Systems and Nanostructures*, 2010, vol. 42, no. 10, doi: 10.1016/j.physe.2009.12.032.

[57] A. Sharma, V. Singh, T. L. Bougher, and B. A. Cola, "A carbon nanotube optical rectenna," *Nature Nanotechnology*, vol. 10, no. 12, 2015, doi: 10.1038/nnano.2015.220.

[58] S. Wen, J. Zhou, P. J. Schuck, Y. D. Suh, T. W. Schmidt, and D. Jin, "Future and challenges for hybrid upconversion nanosystems," *Nature Photonics*, vol. 13, no. 12. 2019, doi: 10.1038/s41566-019-0528-x.

[59] A. Luque and A. Martí, "The intermediate band solar cell: Progress toward the realization of an attractive concept," *Advanced Materials*, vol. 22, no. 2, 2010, doi: 10.1002/adma.200902388.

[60] N. J. Ekins-Daukes *et al.*, "Strain-balanced GaAsP/InGaAs quantum well solar cells," *Applied Physics Letters*, vol. 75, no. 26, 1999, doi: 10.1063/1.125580.

[61] C. Creatore, M. A. Parker, S. Emmott, and A. W. Chin, "Efficient Biologically Inspired Photocell Enhanced by Delocalized Quantum States," *Physical Review Letters*, vol. 111, no. 25, Dec. 2013, doi: 10.1103/PhysRevLett.111.253601.

[62] Y. Zhang, S. Oh, F. H. Alharbi, G. S. Engelc, and S. Kais, "Delocalized quantum states enhance photocell efficiency," *Physical Chemistry Chemical Physics*, vol. 17, no. 8, 2015, doi: 10.1039/c4cp05310a.

[63] K. D. B. Higgins, B. W. Lovett, and E. M. Gauger, "Quantum-Enhanced Capture of Photons Using Optical Ratchet States," *Journal of Physical Chemistry C*, vol. 121, no. 38, 2017, doi: 10.1021/acs.jpcc.7b07138.

[64] Z. Hu, G. S. Engel, F. H. Alharbi, and S. Kais, "Dark states and delocalization: Competing effects of quantum coherence on the efficiency of light harvesting systems," *Journal of Chemical Physics*, vol. 148, no. 6, 2018, doi: 10.1063/1.5009903.

[65] Z. Hu, G. S. Engel, and S. Kais, "Double-excitation manifold's effect on exciton transfer dynamics and the efficiency of coherent light harvesting," *Physical Chemistry Chemical Physics*, vol. 20, no. 47, 2018, doi: 10.1039/c8cp05535a.

[66] M. O. Scully, "Quantum photocell: Using quantum coherence to reduce radiative recombination and increase efficiency," *Physical Review Letters*, vol. 104, no. 20, 2010, doi: 10.1103/PhysRevLett.104.207701.

[67] K. E. Dorfman, D. v. Voronine, S. Mukamel, and M. O. Scully, "Photosynthetic reaction center as a quantum heat engine," *Proceedings of the National Academy of Sciences of the United States of America*, vol. 110, no. 8, 2013, doi: 10.1073/pnas.1212666110.

[68] F. H. Alharbi and S. Kais, "Theoretical limits of photovoltaics efficiency and possible improvements by intuitive approaches learned from photosynthesis and quantum coherence," *Renewable and Sustainable Energy Reviews*, vol. 43. 2015, doi: 10.1016/j.rser.2014.11.101.

[69] J. P. Marangos, "Electromagnetically induced transparency," *Journal of Modern Optics*, vol. 45, no. 3, Mar. 1998, doi: 10.1080/09500349808231909.

[70] M. D. Lukin and A. Imamoğlu, "Controlling photons using electromagnetically induced transparency," *Nature*, vol. 413, no. 6853. 2001, doi: 10.1038/35095000.

[71] P. A. Yin *et al.*, "Theoretical and Experimental Investigations on the Aggregation-Enhanced Emission from Dark State: Vibronic Coupling Effect," *Advanced Electronic Materials*, vol. 6, no. 7, 2020, doi: 10.1002/aelm.202000255.

[72] C. Kittel, *Introduction to Solid State Physics*, 6th Edition. John Wiley, 1986.

[73] B. van Zeghbroeck, "Energy bands," 2007. https://ecee.colorado.edu/~bart/book/book/chapter2/ch2_3.htm (accessed Mar. 29, 2021).

[74] H. Jiang, "Electronic Band Structures of Molybdenum and Tungsten Dichalcogenides by the *GW* Approach," *The Journal of Physical Chemistry C*, vol. 116, no. 14, Apr. 2012, doi: 10.1021/jp300079d.

[75] R. Tenne, L. Margulis, M. Genut, and G. Hodes, "Polyhedral and cylindrical structures of tungsten disulphide," *Nature*, vol. 360, no. 6403, 1992, doi: 10.1038/360444a0.

[76] Z. He and W. Que, "Molybdenum disulfide nanomaterials: Structures, properties, synthesis and recent progress on hydrogen evolution reaction," *Applied Materials Today*, vol. 3. 2016, doi: 10.1016/j.apmt.2016.02.001.

[77] W. J. Schutte, J. L. de Boer, and F. Jellinek, "Crystal structures of tungsten disulfide and diselenide," *Journal of Solid State Chemistry*, vol. 70, no. 2, 1987, doi: 10.1016/0022-4596(87)90057-0.

[78] J. A. Wilson and A. D. Yoffe, "The transition metal dichalcogenides discussion and interpretation of the observed optical, electrical and structural properties," *Advances in Physics*, vol. 18, no. 73, May 1969, doi: 10.1080/00018736900101307.

[79] R. Majumdar, *Quantum Mechanics in Physics and Chemistry with Applications to Biology*, Second Edition. Prentice Hall India, 2014.

[80] N. M. Harrison, "An Introduction to Density Functional Theory." Accessed: Oct. 30, 2016. [Online]. Available: https://www.ch.ic.ac.uk/harrison/Teaching/DFT_NATO.pdf.

[81] J. C. Cuevas, "Introduction to Density Functional Theory." https://www.uam.es/personal_pdi/ciencias/jcuevas/Talks/JC-Cuevas-DFT.pdf (accessed Oct. 30, 2016).

[82] W. Kohn, A. D. Becke, and R. G. Parr, "Density Functional Theory of Electronic Structure," *The Journal of Physical Chemistry*, vol. 100, no. 31, Jan. 1996, doi: 10.1021/jp960669l.

[83] P. Bermel, "ECE 695 Numerical Simulations Lecture 17: Electronic Band Structures," 2017. Accessed: Mar. 30, 2021. [Online]. Available: https://web.ics.purdue.edu/~pbermel/ece695/Lectures/ECE695-Lecture17-S17.pdf.

[84] P. Giannozzi *et al.*, "QUANTUM ESPRESSO: A modular and open-source software project for quantum simulations of materials," *Journal of Physics Condensed Matter*, vol. 21, no. 39, 2009, doi: 10.1088/0953-8984/21/39/395502.

[85] W. Zhao *et al.*, "Origin of indirect optical transitions in few-layer MoS2, WS2, and WSe2," *Nano Letters*, vol. 13, no. 11, 2013, doi: 10.1021/nl403270k.

[86] J. P. Perdew, E. R. McMullen, and A. Zunger, "Density-functional theory of the correlation energy in atoms and ions: A simple analytic model and a challenge," *Physical Review A*, vol. 23, no. 6, 1981, doi: 10.1103/PhysRevA.23.2785.

[87] J. P. Perdew, K. Burke, and M. Ernzerhof, "Generalized Gradient Approximation Made Simple," *Physical Review Letters*, vol. 77, no. 18, Oct. 1996, doi: 10.1103/PhysRevLett.77.3865.

[88] H. J. Monkhorst and J. D. Pack, "Special points for Brillouin-zone integrations," *Physical Review B*, vol. 13, no. 12, Jun. 1976, doi: 10.1103/PhysRevB.13.5188.

[89] F. Aryasetiawan and O. Gunnarsson, "The GW method," *Reports on Progress in Physics*, vol. 61, no. 3, 1998, doi: 10.1088/0034-4885/61/3/002.

[90] F. Bruneval, "The GW Approximation," 2012. Accessed: Oct. 30, 2016. [Online]. Available: http://www.tddft.org/bmg/files/seminarios/127407.pdf.

[91] P. Umari, “Introduction to the GW method.” http://www.quantum-espresso.org/wp-content/uploads/2013/06/talk_school_shanghai13.pdf (accessed Oct. 30, 2016).

[92] “GWL Manual.” http://www.gwl-code.org/manual_gwl.pdf (accessed Oct. 30, 2016).

[93] C. Espejo, T. Rangel, A. H. Romero, X. Gonze, and G. M. Rignanese, “Band structure tunability in MoS2 under interlayer compression: A DFT and GW study,” *Physical Review B - Condensed Matter and Materials Physics*, vol. 87, no. 24, 2013, doi: 10.1103/PhysRevB.87.245114.

[94] T. Cheiwchanchamnangij and W. R. L. Lambrecht, “Quasiparticle band structure calculation of monolayer, bilayer, and bulk MoS2,” *Physical Review B - Condensed Matter and Materials Physics*, vol. 85, no. 20, 2012, doi: 10.1103/PhysRevB.85.205302.

[95] A. R. Beal and H. P. Hughes, “Kramers-Kronig analysis of the reflectivity spectra of 2H-MoS2, 2H-MoSe2 and 2H-MoTe2,” *Journal of Physics C: Solid State Physics*, vol. 12, no. 5, 1979, doi: 10.1088/0022-3719/12/5/017.

[96] J. A. Baglio, “Characterization of n-Type Semiconducting Tungsten Disulfide Photoanodes in Aqueous and Nonaqueous Electrolyte Solutions,” *Journal of The Electrochemical Society*, vol. 129, no. 7, 1982, doi: 10.1149/1.2124184.

[97] M. S. Dresselhaus, “Optical Properties of Solids.” Accessed: Oct. 30, 2016. [Online]. Available: http://web.mit.edu/6.732/www/opt.pdf.

[98] E. Y. Tsymbal, “Optical properties of solids.” Accessed: Oct. 30, 2021. [Online]. Available: http://unlcms.unl.edu/cas/physics/tsymbal/teaching/SSP-927/Section%2013_Optical_Properties_of_Solids.pdf.

[99] R. Ribeiro, “Notes on Quantum ESPRESSO.” http://hawk.fisica.uminho.pt/ricardo-ribeiro/QEnotes.html (accessed Oct. 30, 2021).

[100] A. Benassi, A. Ferretti, and C. Cavazzoni, “P W SCF ’s epsilon.x user’s manual.” Accessed: Oct. 30, 2016. [Online]. Available: http://www.quantum-espresso.org/wp-content/uploads/Doc/pp_user_guide.pdf.

[101] X. Ni, Z. Liu, and A. v. Kildishev, “PhotonicsDB: Optical Constants.” https://nanohub.org/resources/photonicsdb (accessed Oct. 30, 2016).

[102] “nanoHUB.org - Simulation, Education, and Community for Nanotechnology.” https://nanohub.org/ (accessed Oct. 30, 2021).

[103] E. D. Palik, *Handbook of optical constants of solids*, vol. 1. 2012.

[104] R. F. Pierret and G. W. Neudeck, *Advanced Semiconductor Fundamentals*, Second Edition., vol. 6. Reading, MA: Addison-Wesley, 1987.

[105] B. L. Evans and P. A. Young, "Optical absorption and dispersion in molybdenum disulphide," *Proceedings of the Royal Society of London. Series A. Mathematical and Physical Sciences*, vol. 284, no. 1398, 1965, doi: 10.1098/rspa.1965.0071.

[106] H. R. Gutiérrez *et al.*, "Extraordinary room-temperature photoluminescence in triangular WS2 monolayers," *Nano Letters*, vol. 13, no. 8, 2013, doi: 10.1021/nl3026357.

[107] S. Alfihed, M. Hossain, A. Alharbi, A. Alyamani, and F. H. Alharbi, "PLD Grown Polycrystalline Tungsten Disulphide (WS2) Films," *Journal of Materials*, vol. 2013, 2013, doi: 10.1155/2013/603648.

[108] K. Masuko *et al.*, "Achievement of more than 25% conversion efficiency with crystalline silicon heterojunction solar cell," *IEEE Journal of Photovoltaics*, vol. 4, no. 6, 2014, doi: 10.1109/JPHOTOV.2014.2352151.

[109] R. V. K. Chavali *et al.*, "Multiprobe Characterization of Inversion Charge for Self-Consistent Parameterization of HIT Cells," *IEEE Journal of Photovoltaics*, vol. 5, no. 3, 2015, doi: 10.1109/JPHOTOV.2014.2388072.

[110] S. Hwan Lee, D. Lee, W. Sik Hwang, E. Hwang, D. Jena, and W. Jong Yoo, "High-performance photocurrent generation from two-dimensional WS2 field-effect transistors," *Applied Physics Letters*, vol. 104, no. 19, 2014, doi: 10.1063/1.4878335.

[111] S. L. Howell *et al.*, "Investigation of Band-Offsets at Monolayer-Multilayer MoS2 Junctions by Scanning Photocurrent Microscopy," *Nano Letters*, vol. 15, no. 4, 2015, doi: 10.1021/nl504311p.

[112] X. Liu *et al.*, "High performance field-effect transistor based on multilayer tungsten disulfide," *ACS Nano*, vol. 8, no. 10, 2014, doi: 10.1021/nn505253p.

[113] M. W. Iqbal *et al.*, "High-mobility and air-stable single-layer WS2 field-effect transistors sandwiched between chemical vapor deposition-grown hexagonal BN films," *Scientific Reports*, vol. 5, 2015, doi: 10.1038/srep10699.

[114] E. Hecht, *Optics*, 4th Edition. Pearson Education, 2002.

[115] S. M. Sze and K. M. Kwok, *Physics of semiconductor devices*, 3rd Edition. Wiley Online Library, 2007.

[116] E. A. Schiff, "Carrier drift-mobilities and solar cell models for amorphous and nanocrystalline silicon," *MRS Proceedings*, vol. 1153, Jan. 2009, doi: 10.1557/PROC-1153-A15-01.

[117] "Reference Air Mass 1.5 Spectra." https://www.nrel.gov/grid/solar-resource/spectra-am1.5.html (accessed Sep. 29, 2019).

[118] "Standard Solar Spectra." https://www.pveducation.org/pvcdrom/appendices/standard-solar-spectra (accessed Sep. 29, 2019).

[119] M. A. Green, "Photovoltaic principles," in *Physica E: Low-Dimensional Systems and Nanostructures*, 2002, vol. 14, no. 1–2, doi: 10.1016/S1386-9477(02)00354-5.

[120] "P/N Junctions and Band Gaps." http://solarcellcentral.com/junction_page.html (accessed Oct. 30, 2016).

[121] "The photovoltaic effect | PVEducation." https://www.pveducation.org/pvcdrom/solar-cell-operation/the-photovoltaic-effect (accessed Oct. 30, 2016).

[122] R. F. Pierret, *Semiconductor Device Fundamentals*. Reading, MA: Addison Wesley Longman, 1996.

[123] J. Gray, X. Wang, R. V. K. Chavali, X. Sun, A. Kranti, and J. R. Wilcox, "ADEPT 2.1," 2015. https://nanohub.org/resources/10913/about#citethis (accessed Oct. 30, 2016).

[124] X. Wang, M. R. Khan, J. L. Gray, M. A. Alam, and M. S. Lundstrom, "Design of GaAs solar cells operating close to the shockley-queisser limit," *IEEE Journal of Photovoltaics*, vol. 3, no. 2, 2013, doi: 10.1109/JPHOTOV.2013.2241594.

[125] J. E. Moore, C. J. Hages, N. J. Carter, R. Agrawal, J. L. Gray, and M. S. Lundstrom, "Current-voltage analysis of band tail effects in CZTSSe through numerical simulation," 2015, doi: 10.1109/PVSC.2015.7355784.

[126] Y. Sun, K. H. Montgomery, X. Wang, S. Tomasulo, M. L. Lee, and P. Bermel, "Modeling wide bandgap GaInP photovoltaic cells for conversion efficiencies up to 16.5%," 2015, doi: 10.1109/PVSC.2015.7356074.

[127] "Quantum Efficiency | PVEducation." https://www.pveducation.org/pvcdrom/solar-cell-operation/quantum-efficiency (accessed Jan. 23, 2016).

[128] "Short-Circuit Current | PVEducation." https://www.pveducation.org/pvcdrom/solar-cell-operation/short-circuit-current (accessed Jan. 23, 2016).

[129] "Open-Circuit Voltage | PVEducation." https://www.pveducation.org/pvcdrom/solar-cell-operation/open-circuit-voltage (accessed Jan. 23, 2016).

[130] K. F. Mak and J. Shan, "Photonics and optoelectronics of 2D semiconductor transition metal dichalcogenides," *Nature Photonics*, vol. 10, no. 4. 2016, doi: 10.1038/nphoton.2015.282.

[131] S. Meroli, "The Minority Carrier Lifetime in Silicon Wafer." https://meroli.web.cern.ch/Lecture_lifetime.html (accessed May 25, 2017).

[132] J. G. Fossum, R. P. Mertens, D. S. Lee, and J. F. Nijs, "Carrier recombination and lifetime in highly doped silicon," *Solid State Electronics*, vol. 26, no. 6, 1983, doi: 10.1016/0038-1101(83)90173-9.

[133] G. Masetti, M. Severi, and S. Solmi, "Modeling of Carrier Mobility Against Carrier Concentration in Arsenic-, Phosphorus-, and Boron-Doped Silicon," *IEEE Transactions on Electron Devices*, vol. 30, no. 7, 1983, doi: 10.1109/T-ED.1983.21207.

[134] C. Ballif, D. M. Huljić, G. Willeke, and A. Hessler-Wyser, "Silver thick-film contacts on highly doped n-type silicon emitters: Structural and electronic properties of the interface," *Applied Physics Letters*, vol. 82, no. 12, 2003, doi: 10.1063/1.1562338.

[135] V. P. Pham and G. Y. Yeom, "Recent Advances in Doping of Molybdenum Disulfide: Industrial Applications and Future Prospects," *Advanced Materials*, vol. 28, no. 41. 2016, doi: 10.1002/adma.201506402.

[136] J. Hu, M. Ouyang, P. Yang, and C. M. Lieber, "Controlled growth and electrical properties of heterojunctions of carbon nanotubes and silicon nanowires," *Nature*, vol. 399, no. 6731, 1999, doi: 10.1038/19941.

[137] B. Tian *et al.*, "Coaxial silicon nanowires as solar cells and nanoelectronic power sources," *Nature*, vol. 449, no. 7164, 2007, doi: 10.1038/nature06181.

[138] "Solar Cell Efficiency Records | PVEducation." https://www.pveducation.org/pvcdrom/appendices/solar-cell-efficiency-results2 (accessed Oct. 30, 2016).

[139] Z. Huang *et al.*, "Tungsten sulfide enhancing solar-driven hydrogen production from silicon nanowires," *ACS Applied Materials and Interfaces*, vol. 6, no. 13, 2014, doi: 10.1021/am501940x.

[140] H. Chung, K.-Y. Jung, and P. Bermel, "Flexible flux plane simulations of parasitic absorption in nanoplasmonic thin-film silicon solar cells," *Optical Materials Express*, vol. 5, no. 9, 2015, doi: 10.1364/ome.5.002054.

[141] A. Ristow, M. M. Hilali, A. Ebong, and A. Rohatgi, "Screen-printed back surface reflector for light trapping in crystalline silicon solar cells," *Georgia Institute of Technology*, 2001.

[142] J. D. Lin *et al.*, "Electron-doping-enhanced trion formation in monolayer molybdenum disulfide functionalized with cesium carbonate," *ACS Nano*, vol. 8, no. 5, 2014, doi: 10.1021/nn501580c.

[143] R. J. Walters, S. Messenger, J. H. Warner, C. D. Cress, M. Gonzalez, and S. Maximenko, "Modeling of radiation induced defects in space solar cells," in *Physics and Simulation of Optoelectronic Devices XIX*, 2011, vol. 7933, doi: 10.1117/12.873902.

[144] H. Y. Tada and J. R. Carter Jr., *Solar Cell Radiation Handbook*. JPL Publication, 1977.

[145] M. Yamaguchi, A. Khan, S. J. Taylor, M. Imaizumi, T. Hisamatsu, and S. Matsuda, "A detailed model to improve the radiation-resistance of si space solar cells," *IEEE Transactions on Electron Devices*, vol. 46, no. 10, 1999, doi: 10.1109/16.792008.

[146] T. Sumita, M. Imaizumi, S. Matsuda, T. Ohshima, A. Ohi, and H. Itoh, "Proton radiation analysis of multi-junction space solar cells," in *Nuclear Instruments and Methods in Physics Research, Section B: Beam Interactions with Materials and Atoms*, 2003, vol. 206, doi: 10.1016/S0168-583X(03)00791-2.

[147] L. C. Hirst *et al.*, "Intrinsic radiation tolerance of ultra-thin GaAs solar cells," *Applied Physics Letters*, vol. 109, no. 3, 2016, doi: 10.1063/1.4959784.

[148] "Effect of Temperature." https://www.pveducation.org/pvcdrom/solar-cell-operation/effect-of-temperature (accessed Oct. 27, 2020).

[149] V. Liu and S. Fan, "S4: A free electromagnetic solver for layered periodic structures," *Computer Physics Communications*, vol. 183, no. 10, Oct. 2012, doi: 10.1016/j.cpc.2012.04.026.

[150] M. Ghebrebrhan, P. Bermel, Y. Avniel, J. D. Joannopoulos, and S. G. Johnson, "Global optimization of silicon photovoltaic cell front coatings," *Optics Express*, vol. 17, no. 9, 2009, doi: 10.1364/oe.17.007505.

[151] J. Kang, X. Wang, P. Bermel, and C. Liu, "S4: Stanford Stratified Structure Solver," 2012, doi: https://doi.org/10.4231/D35T3G11T.

[152] E. Yablonovitch and G. D. Cody, "Intensity Enhancement in Textured Optical Sheets for Solar Cells," *IEEE Transactions on Electron Devices*, vol. 29, no. 2, 1982, doi: 10.1109/T-ED.1982.20700.

[153] F. J. Beck, A. Stavrinadis, T. Lasanta, J.-P. Szczepanick, and G. Konstantatos, "Understanding light trapping by resonant coupling to guided modes and the importance of the mode profile," *Optics Express*, vol. 24, no. 2, 2016, doi: 10.1364/oe.24.000759.

[154] K. Li *et al.*, "Light trapping in solar cells: simple design rules to maximize absorption," *Optica*, vol. 7, no. 10, 2020, doi: 10.1364/optica.394885.

[155] S. Schauer *et al.*, "Disordered diffraction gratings tailored by shape-memory based wrinkling and their application to photovoltaics," *Optical Materials Express*, vol. 8, no. 1, 2018, doi: 10.1364/ome.8.000184.

[156] S. Mokkapati and K. R. Catchpole, "Nanophotonic light trapping in solar cells," *Journal of Applied Physics*, vol. 112, no. 10. 2012, doi: 10.1063/1.4747795.

[157] Z. Yu, A. Raman, and S. Fan, "Fundamental limit of light trapping in grating structures," *Optics Express*, vol. 18, no. S3, 2010, doi: 10.1364/oe.18.00a366.

[158] S. Fan and J. D. Joannopoulos, "Analysis of guided resonances in photonic crystal slabs," *Physical Review B - Condensed Matter and Materials Physics*, vol. 65, no. 23, 2002, doi: 10.1103/PhysRevB.65.235112.

[159] C. Hsu *et al.*, "Thickness-Dependent Refractive Index of 1L, 2L, and 3L MoS2, MoSe2, WS2, and WSe2," *Advanced Optical Materials*, vol. 7, no. 13, 2019, doi: 10.1002/adom.201900239.

[160] H. C. Kim *et al.*, "Engineering Optical and Electronic Properties of WS2 by Varying the Number of Layers," *ACS Nano*, vol. 9, no. 7, 2015, doi: 10.1021/acsnano.5b01727.

[161] F. Packeer, M. A. M. Zawawi, N. Z. I. Hashim, N. M. Noh, W. M. Jubadi, and M. Missous, "Alternative Spin-On-Glass (SoG) material characterization for Deep-Submicron (<0.35 um) soft reflow fabrication process," in *IOP Conference Series: Materials Science and Engineering*, 2018, vol. 380, no. 1, doi: 10.1088/1757-899X/380/1/012005.

[162] C. Chiang and D. B. Fraser, "Understanding of spin-on-glass (SOG) properties from their molecular structure," 1989, doi: 10.1109/vmic.1989.78000.

[163] B. J. van Zeghbroeck, “Temperature dependence of the energy bandgap.” https://ecee.colorado.edu/~bart/book/eband5.htm (accessed Mar. 07, 2021).

[164] “PSTAR.” https://physics.nist.gov/PhysRefData/Star/Text/PSTAR.html (accessed Mar. 07, 2021).

[165] M. M. Benameur, B. Radisavljevic, J. S. Héron, S. Sahoo, H. Berger, and A. Kis, “Visibility of dichalcogenide nanolayers,” *Nanotechnology*, vol. 22, no. 12, Mar. 2011, doi: 10.1088/0957-4484/22/12/125706.

[166] W. Zhao *et al.*, “Evolution of electronic structure in atomically thin sheets of WS2 and WSe2,” *ACS Nano*, vol. 7, no. 1, 2013, doi: 10.1021/nn305275h.

[167] S. Roy and P. Bermel, “Electronic and optical properties of ultra-thin 2D tungsten disulfide for photovoltaic applications,” *Solar Energy Materials and Solar Cells*, vol. 174, Jan. 2018, doi: 10.1016/j.solmat.2017.09.011.

[168] “Dipole Moments - Chemistry LibreTexts.” https://chem.libretexts.org/Bookshelves/Physical_and_Theoretical_Chemistry_Textbook_Maps/Supplemental_Modules_(Physical_and_Theoretical_Chemistry)/Physical_Properties_of_Matter/Atomic_and_Molecular_Properties/Dipole_Moments (accessed Jan. 24, 2018).

[169] K. Kalantar-Zadeh *et al.*, “Synthesis of nanometre-thick MoO3 sheets,” *Nanoscale*, vol. 2, no. 3, 2010, doi: 10.1039/b9nr00320g.

[170] A. R. Beal and W. Y. Liang, “Excitons in 2H-WSe2 and 3R-WS2,” *Journal of Physics C: Solid State Physics*, vol. 9, no. 12, 1976, doi: 10.1088/0022-3719/9/12/029.

[171] P. P. González-Borrero *et al.*, “Optical band-gap determination of nanostructured WO3 film,” *Applied Physics Letters*, vol. 96, no. 6, 2010, doi: 10.1063/1.3313945.

[172] M. A. Alam and M. Ryyan Khan, “Shockley–Queisser triangle predicts the thermodynamic efficiency limits of arbitrarily complex multijunction bifacial solar cells,” *Proceedings of the National Academy of Sciences of the United States of America*, vol. 116, no. 48, 2019, doi: 10.1073/pnas.1910745116.

[173] M. Palummo, M. Bernardi, and J. C. Grossman, “Exciton Radiative Lifetimes in Two-Dimensional Transition Metal Dichalcogenides,” *Nano Letters*, vol. 15, no. 5, May 2015, doi: 10.1021/nl503799t.

[174] G. Moody *et al.*, "Intrinsic homogeneous linewidth and broadening mechanisms of excitons in monolayer transition metal dichalcogenides," *Nature Communications*, vol. 6, 2015, doi: 10.1038/ncomms9315.

VITA

Sayan Roy graduated with a B. S. in Electrical Engineering from Purdue University, West Lafayette, IN, USA in 2013. He obtained his M. S. degree in Electrical and Computer Engineering from Purdue University, West Lafayette, IN, USA in 2017. He is currently a Ph.D. candidate in the School of Electrical and Computer Engineering at Purdue University. His research interests include transition metal di-chalcogenides (TMDCs), photovoltaics, photonics and nanoelectronics. His doctoral research topic is modeling of ultrathin 2D TMDCs for nanoelectronic and photovoltaic applications and implementing advanced techniques, with a focus on tungsten disulfide, tungsten diselenide and hybrid tungsten-based TMDCs. In addition to his research activities, he has been a teaching assistant (TA) for many courses in the ECE department at Purdue University over several semesters. He was awarded the Magoon Award for Excellence in Teaching at Purdue University in 2017.

PUBLICATIONS

[1] S. Roy and P. Bermel, “Electronic and optical properties of ultra-thin 2D tungsten disulfide for photovoltaic applications,” *Solar Energy Materials and Solar Cells*, vol. 174, Jan. 2018, doi: 10.1016/j.solmat.2017.09.011.

[2] S. Roy, Z. Hu, S. Kais, and P. Bermel, “Enhancement of Photovoltaic Current through Dark States in Donor-Acceptor Pairs of Tungsten-Based Transition Metal Di-Chalcogenides,” *Advanced Functional Materials*, March 2021, doi: 10.1002/adfm.202100387.

[3] S. Roy, Z. Hu, S. Kais, and P. Bermel, “Tailoring Donor-Acceptor Pairs of Tungsten-based Transition Metal Di-Chalcogenides (TMDCs) for Improved Photovoltaic Current Generation,” *IEEE 46th Photovoltaic Specialists Conference (PVSC)*, June 2019, doi: 10.1109/PVSC40753.2019.8981337.

[4] S. Roy and P. Bermel. "2D Tungsten Disulfide Sheets for Ultralight, Flexible Photovoltaics." *Optics for Solar Energy*, Optical Society of America, November 2018, doi: https://doi.org/10.1364/OSE.2018.OM2D.4.